Thermochronometric Investigation of Multiple Unconformities and Post-depositional Thermal History of a Fault Block in the Northern Western Desert, Egypt

by

Travis Robert Glauser

B.S., University of Kansas, 2006

Submitted to the Department of Geology and the

Faculty of the Graduate School of the University of

Kansas in partial fulfillment of the requirements for the

degree of Master of Science

Advisory Committee

_____
Dr. Daniel F. Stockli (Chairman)

_____
Dr. Anthony W. Walton

_____
Dr. Michael H. Taylor

Date Submitted: December 8, 2010

The Thesis Committee for Travis Glauser certifies that this is the approved version of the following thesis:

Thermochronometric Investigation of Multiple Unconformities and Post-depositional Thermal History of a Fault Block in the Northern Western Desert, Egypt

Committee:

_____

Chairperson: Dr. Daniel F. Stockli

Date approved: December 8, 2010

Abstract

Thermochronometric Investigation of Multiple Unconformities and Post-depositional Thermal History of a Fault Block in the Northern Western Desert, Egypt

By

Travis Glauser

Department of Geology, November 2010

University of Kansas

Detrital apatite and zircon (U-TH)/He analysis across a recently discovered unconformity in the Western Desert of Egypt provides new insight into the tectonic evolution of northeastern Africa. The unconformity juxtaposes Cretaceous and Cambrian-Ordovician strata, and poses a potential problem for the mapping of a Jurassic hydrocarbon source rock in and near the Faghur Basin. This study utilizes detrital apatite and zircon (U-Th)/He analysis of samples collected from two boreholes in the Western Desert to elucidate the timing and magnitude of this unconformity. Data from detrital minerals further provides insight into the tectonic and thermal evolution of source terrane (ie. timing of exhumation). Detrital zircon (U-Th)/He (DZHe) ages from Cretaceous to Tertiary formations above the unconformity represent the cooling ages of source terranes with respect to the ZHe closure temperature. These ages can indicate timing of geological processes such as tectonic uplift or erosional unroofing. Statistical analysis of the DZHe ages within formations support a series of models for the influx of sediment during distinct periods of tectonic activity. The ZHe data supports two main conclusions. First, DZHe ages from below the unconformity postdate Paleozoic strata, and support Hercynian-related

uplift of a fault block during the Carboniferous in the northern Western Desert of Egypt. This paleo-structural-high shed sediments into onlapping Jurassic and Early Cretaceous units and remained subaerially exposed until the Late Cretaceous. Second, ZHe ages above the unconformity predate Mesozoic-Cenozoic strata, and the Safa Sandstone and Alam El Buib (AEB) Formation contain Triassic to Jurassic detrital components, which reveal the presence of a rapidly exhumed fault block associated with Triassic-Jurassic rifting. Detrital apatite (U-Th)/He (DAHe) data is limited by the current geothermal gradient to the near surface Moghra formation, but provides a record of sediment influx from Late Cretaceous to Late Eocene compressional events of the Neotethyan margin.

Acknowledgements

Apache Egypt provided cuttings samples from the Sokar-1X and Heqet-2 boreholes as well as the majority of funding for this project. This project would not have been possible without support and insight from Bill Bosworth, Alan Clare and Tom Maher at Apache Egypt. Additional funding was provided by National Science Foundation grants to Stockli (EAR-0414817 and EAR-0305731), and KU Departmental grants and American Association of Petroleum Geologists Gustavus Archie Memorial Grant awarded to Glauser. The University of Kansas Isotope Geochemisty Laboratory staff and fellow graduate students Roman Kislitsyn, Chris Hager, Melissa Wolfe, Eugene Symanski, Markella Hoffman, Jeff Schroeder, T.J. Dewane, John Lee, Evan Bargnesi, Kyle Gorynski, Edgardor Pujols and Sarah Evans provided vital support and training on (U-Th)/He analytical methods including laser heating, mineral dissolution and inductively coupled plasma mass spectrometry. The faculty and staff at the University of Kansas Department of Geology were a tremendous resource, particularly committee members Anthony W. Walton Ph.D. and Michael Taylor Ph.D. Finally, the foundation of this project was set by Daniel Stockli, Ph.D. and the completion of the project would not have been possible without his knowledge, advisement, and support.

TABLE OF CONTENTS

Introduction

This project was initiated by Daniel Stockli (University of Kansas Geology) and Bill Bosworth (Apache Egypt Corp) to investigate the timing and magnitude of an erosional unconformity in the Western Desert of Egypt, as well as to provide insight on the value of using detrital minerals to determine the tectonic and thermal history of detrital source terranes. The following two chapters outline the results and implications of (U-Th)/He analysis of detrital zircon (chapter 1) and apatite (chapter 2) extracted from cuttings from the Sokar-1X and Heqet-2 boreholes located in and near the Fahgur Basin. All mineral separation and (U-Th)/He analysis was carried out at the University of Kansas Isotope Geochemistry Laboratory.

Chapter one focuses on the detrital zircon (U-Th)/He results and implications. The zircon data answers the primary goal of this study, which is to determine the timing and magnitude of a previously-undocumented unconformity that juxtaposes Cretaceous units over Cambro-Ordovician units, omitting Late Paleozoic and part of the Early Cretaceous units. The ZHe ages below the unconformity are younger than the depositional age of zircon indicating that they were buried to depth were the thermal gradient exceeded the zircon-helium closure temperature. The DZHe ages indicate the presence of a paleo-structural high uplifted in the Carboniferous in the vicinity of the Sokar-1X well that remained subaerially exposed to the Late Cretaceous. This is an important realization that will aid in the continued mapping and exploration of the Safa source rock in and near the Fahgur basin.

Additionally, this chapter discusses detrital zircon (U-Th)/He as a viable technique to provide absolute age constraints on the thermal evolution of the source terrane of zircon found in the stratigraphic column of the Western Desert. The data above the unconformity were not buried to sufficient depth to exceed the He closure temperature of zircon. Therefore DZHe ages

above the unconformity are representative of the cooling of their source terrane. A series of probability distribution diagrams are presented, which isolate definite populations of DZHe ages. This statistical evaluation of the DZHe data reveals a record of influx of sediment into the basin during distinct periods of tectonic activity in northern Africa. The result of the study is a series of theoretical diagrams that illustrate the evolution of the basin configuration during deposition of the stratigraphic column.

Chapter two presents and discusses apatite (U-Th)/He data. The nature of the present geothermal gradient and the low abundance of inorganic detrital apatite in the stratigraphic units sampled limited the amount of detrital apatite data acquired. The strata within a significant portion of the theoretical apatite partial retention zone (APRZ) consist of dominantly carbonate and fine-grained rocks that were not expected to yield zircon and inorganic apatite and were therefore not sampled. The detrital apatite (U-Th)/He age populations identified in samples from above the APRZ correspond well with tectonic events from widespread Santonian inversion to the onset of Early Miocene rifting. This new apatite data supports current work on basin inversion time constraints in the region.

CHAPTER 1: Thermochronometric investigation of multiple unconformities and post-depositional thermal history of a fault block in the northern Western Desert, Egypt

Abstract

The subsurface of the Western Desert of Egypt contains multiple stacked sedimentary deposits separated by major unconformities reflecting the long-lived tectonic evolution of the Neotethyan continental margin in eastern North Africa. In this study, zircon (U-Th)/He (ZHe) data from two boreholes was collected to elucidate the thermal evolution of the drilled strata and to explore the detrital provenance and thermal history of the source terrane. The ~15,000 ft deep Sokar-1X borehole penetrates Tertiary and Cretaceous strata, a major erosional unconformity at ~13,100 ft and Cambro-Ordovician section below the unconformity. The Heqet-2 borehole contains complete Late Paleozoic and Jurassic section that is omitted in the Sokar-1X borehole. A total of 58 samples of borehole cuttings from the Sokar-1X borehole and 8 samples from the Heqet-2 borehole were analyzed, resulting in 274 single-crystal ZHe ages. ZHe ages above the unconformity are significantly older than the depositional age, suggesting detrital ZHe ages that were not reset subsequent to deposition. ZHe ages from Cambro-Ordovician strata below the unconformity are substantially younger than the minimum depositional age suggesting major cooling and resetting of zircon (>200°C) during the Hercynian orogeny. Specifically, ZHe ages form Cretaceous strata above the unconformity show the following trends: (1) ZHe ages from 6,000-9,000 ft (Aptian-Early Cenomanian) are characterized by a ZHe age peak at 450 Ma and a minor Albian peak, (2) samples from 9,000-12,000 ft (Late Hauterivian-Barremian) show two major detrital ZHe age peaks at 450 and 350 Ma, and (3) samples from 12,000-13,000 ft (Early Hauterivian) exhibit three dominant ZHe age components at 450 Ma, 350 Ma, and 170-200 Ma.

Additional cuttings from the Heqet-2 borehole containing complete stratigraphy yield ZHe ages that mainly represent a strong Hercynian input as well as Late Triassic and Early Jurassic components of Tethyan-related input. These ZHe age peaks display provenance characteristics typical for cooling signatures of rocks from the eroding Arabian-Nubian Shield, a North-African Hercynian source, and eroded material from exhumed fault blocks along the Triassic-Jurassic Neotethyan rifted margin. While immediately above the unconformity Hercynian ZHe ages dominate, the occurrence of Triassic or Early Jurassic ages suggest the presence of eroding rapidly cooled and exhumed Tethyan normal fault blocks. At decreasing depth, first Jurassic-Triassic, and then Hercynian source input disappears and the arrival of detritus from the Arabian-Nubian Shield begins to dominate the North African passive continental margin in the Western Desert in the middle to late Cretaceous. This unique data set illustrates the value of ZHe thermochronometry as a thermochronometer in strata with cooling temperatures exceeding those that can be examined by other low-temperature dating techniques, and as a detrital provenance tool. It cannot constrain crystallization ages, but rather sheds light on the cooling and exhumation history of the source terrane and the tectonic/geological environment of the basin deposits.

1. Introduction

The Phanerozoic tectonic evolution of northern Africa contains multiple phases of collision, formation of a passive Tethyan continental margin, multi-phase rifting during the break-up of Pangea and more recent inversion events related to collision associated with the final closure of the Neotethys ocean (Said, 1962; Sestini, 1984; Ziegler, 1989; Keeley, 1994; Unrug, 1996; Boote et al., 1998; Guiraud and Bosworth, 1999; Stampfli et al., 2001a; Badalini et al.,

2002; Bumby and Guiraud, 2005; Guiraud et al., 2005; Bosworth et al., 2008). Throughout this tectonic evolution, many basins have been created and amassed sediment in northern Africa. Detrital minerals from these basins record the multi-phase tectonic history of contraction and extension.

A recent hydrocarbon exploration well in the Western Desert of Egypt (Fig. 1) penetrated an unexpected unconformity, where Late Cretaceous rocks unconformably overlie Cambrian to Ordovician siliciclastics. Upper Paleozoic and Mesozoic up to part of the Hauterivian strata are omitted. This study utilizes detrital zircon (U-Th)/He analysis, a low-temperate dating technique, on drill cutting samples collected from two boreholes in the Western Desert to (1) elucidate the timing and magnitude of this unconformity, (2) provide insight into the tectonic and thermal evolution of the source terrane (ie. timing of exhumation of various source terranes), and (3) determine the value of DZHe thermochronometry as a detrital provenance tool. This methodology does not constrain crystallization ages, but rather elucidates the cooling and exhumation history of the source terrane and the tectonic section of rift basin fill. Thus, this study enables reconstruction of the evolving structural setting of the Western Desert, from the time of uplift of the eroded fault block through the present, including tectonic uplift and exhumation of source terranes.

Previously, detrital geochronology and low-temperature thermochronology techniques have been used in a wide range of geologic and tectonic studies. Detrital mineral geochronology, typically by *in situ* zircon U-Pb methods, either laser ablation or ion probe, has become the standard for elucidating crystallization ages of source terranes to establish provenance of detrital minerals. However, U-Pb methods are not typically able to differentiate the timing of exhumation of various source terranes. They therefore do not fully reflect the

thermal and tectonic histories of the source terrane (Fedo et al., 2003). In order to determine the timing of exhumation of various source terranes, several viable thermochornology techniques have recently been used. For example, $^{40}Ar/^{39}Ar$ (e.g. Najman et al., 1997; Stuart, 2002; Hodges et al., 2005, Huntington and Hodges, 2006), zircon fission track (ZFT) (e.g. Bernet and Garver, 2005; Tagami and O'Sullivan, 2005) and zircon (U-Th)/(He-Pb) double dating (Reiners et al., 2005). This study uses zircon (U-Th)/He thermochronology applied to detrital zircon in order to determine the magnitude and timing of the unconformity and shed light on the cooling and exhumation history of the source terrane. ZHe dating is a well-established technique applied in many recent geologic, stratigraphic, tectonic, and geomorphologic studies to constrain the timing of erosional exhumation (Ehlers and Farley, 2003; Reiners, 2005; Stockli, 2005). See below for examples, advantages and limitations of the aforementioned viable techniques, and justification of (U-Th)/He dating as a better technique for this and similar studies in which determining the tectonic and thermal evolution of the source terrane is essential.

2. Detrital Geochronology and Thermochronology

The timing of geologic events that involve cooling of minerals, such as the cooling of volcanic rocks, exhumation or erosional unroofing, can be measured quantitatively by observing radioactive decay systems using geochronology or thermochronology techniques. Measurements of parent and daughter isotopes of a given decay system can be used to calculate ages that represent a time where certain environmental conditions, particularly temperature, existed. Either parent or daughter isotopes can be lost by thermal diffusion above a mineral and element-specific closure temperature. Below the closure temperature all isotopes are retained. There are many different techniques that can be used to determine the age of a mineral based on a

particular radioactive decay system. These provide an age representing the time at which all mobile elements are retained. Some ages can be linked to certain geological processes. For instance, this study links ZHe cooling ages to the age of either rapid cooling of volcanics or exhumation of zircon-bearing rock. Many different techniques are capable of determining an age representing the mineral passing through a thermal barrier that divides diffusive loss versus retention. Geochronometers typically have a closure representative of the crystallization of a mineral, whereas low-temperature thermochronometry provides the cooling history due to some geologic process (e.g. rapid cooling, erosional unroofing, fault exhumation, etc.).

Geochronology has been used extensively to date igneous and metamorphic crystallization, but has also been applied to detrital studies (e.g. Dodson et al., 1988; Barton et al. 1989). Zircon U-Pb dating is a commonly employed geochronometer in detrital studies due to zircon's resistance to chemical and mechanical weathering during transport and its affinity for radioactive minerals. Detrital studies usually utilize crystallization ages of the detrital source terrane to link basin deposits and provenance (e.g. Ross and Bowring, 1990; DeGraaff-Surpless et al. 2002), but the crystallization age typically does not reveal information about more subtle cooling histories. On the other hand, thermochronology has the advantage of resolving these lower-temperature cooling histories (e.g. Stockli, 2005). When applied to detrital minerals, it can relate detrital age signature of sedimentary rocks to tectonic and erosional processes associated with the source region (e.g. Armstrong, 2005).

$^{40}Ar/^{39}Ar$ thermochronology is a powerful technique that has been applied to recent studies to constrain cooling histories in tectonic and erosion processes of source terranes (McDougall and Harrison, 1999; Hodges et al., 2005; Huntington and Hodges, 2006) with the advantage of fast laser fusion analysis that yields very precise results. Muscovite $^{40}Ar/^{39}Ar$ has a

closure temperature of ~350-400°C that allows exhumation ages above 10-8 km of depth to be constrained (Harrison, 1985; Stuart et al., 2002). For sediments that do not reach the closure temperature during burial, detrital $^{40}Ar/^{39}Ar$ can be used to better constrain absolute ages of maximum burial (Najman et al., 1997). Drawbacks of the $^{40}Ar/^{39}Ar$ method lie mainly within the characteristics of argon-bearing minerals. Muscovite and potassium-bearing minerals are not present in all parent lithologies and are very susceptible to chemical and mechanical weathering during detrital transport. Zircon, on the other hand, is not as susceptible to weathering and abrasion, so it may be found in even the most mature of sandstones.

Detrital zircon fission track thermochronometry (DZFT) is another viable low-temperature technique applied to tectonic exhumation and erosional studies of orogenic belts and their corresponding sedimentary rocks (Bernet and Garver, 2005; Tagami and O'Sullivan 2005), and provided depositional age constraints (Tagami and Dumitru, 1996; Carter, 1999). DZFT analysis typically shows the most recent thermal event (cooling below the annealing temperature ~240°C ± 30°C), which is commonly directly related to uplift or exhumation (Hurford, 1986). This higher closure temperature may not be applicable to all studies where a lower closer temperature is ideal.

Recently, (U-Th)/He thermochronometry (typically apatite and zircon) has been applied to many geologic, stratigraphic, tectonic, and geomorphologic studies (Reiners, 2005; Stockli, 2005; Biswas et al., 2007). This technique can elucidate the timing of exhumation of fault blocks related to tectonic events that usually cannot be dated by U-Pb crystallization ages, and utilizes several common minerals (e.g. zircon, apatite). Helium ages provide a significantly shorter erosional lag time (i.e. the time between exhumation cooling and exposure at the surface), than other methods due to the proximity of the closure temperature to the surface in

common geothermal gradients. Apatite (U-Th)/He dating has a closure temperature ~70°C (Wolf et al., 1996; Stockli et al., 2000; Farley, 2002, Farley and Stockli, 2002; Ehlers and Farley, 2003) and hence lag time. The lower closure temperature can also be a disadvantageous as cooling ages can be erased with minimal heating, and Apatite (U-Th)/He dating may not be an effective technique in samples extracted from a deep borehole. Zircon has a helium closure temperature of 180°C (Reiners et al., 2002; Reiners et al., 2004), which creates a balance between maximum sampling depth and erosional lag time. Zircon is common in igneous and metamorphic source lithologies and is very robust during transport, making it an ideal mineral for detrital studies involving exhumation of source terranes.

Geochronometers and thermochronometers can be combined in a single study to connect provenance crystallization ages with tectonic histories of provenance defined by exhumation of source terranes (e.g. Carter and Moss 1999). (U-Th)/He zircon dating coupled with U-Pb laser ablation ICPMS can relate crystallization ages and exhumation ages (Rahl et al., 2003; Reiners et al., 2005; MacPhee et al., 2005) or furthermore combining the former with $^{40}Ar/^{39}Ar$ (Harris et al. 2008). This study does not present double or triple dating data, but rather is a high-resolution DZHe study that sheds light on the tectonic history, sediment dispersal, detrital source thermal/tectonic evolution, and the impact of tectonic events on this long-lived Tethyan margin from sediment deposited in the Western Desert of Egypt.

3. Geological Setting

3.1 Proterozoic Formation of Gondwana and Proterozoic Effects of Gondwanan Suture Zones

The Proterozoic-Phanerozoic tectonic history of northeastern Africa consists of several extensional and contractional phases associated with the formation of Gondwana, collision of

Gondwana with Laurasia and subsequent break-up of Pangea (Guiraud and Bosworth, 1999; Badalini et al., 2002; Guiraud et al., 2005). In the late Proterozoic (720-540 Ma), Gondwana was assembled as a result of Pan-African-Brasillian orogenesis (Unrug, 1996). Orogenic suture zones became zones of weakness for subsequent deformation (Wilson and Guiraud, 1998; Bumby and Guiraud, 2005). From the mid-Cambrian to the present, these zones were repeatedly reactivated by intra-cratonic strike-slip movement, initiating transpressional basin inversion and transtensional basin subsidence. Along the northern margin of Gondwana, this subsidence resulted in formation of localized basins along the northeastern margin of what is now the African plate (Badalini et al., 2002), particularly along the Trans-African Lineament (Keeley, 1994).

3.2 Paleozoic Evolution and Neotethys Formation

During the Paleozoic, northeastern African basins experienced long periods of subsidence and short periods of gentle folding with episodic basin inversion. Throughout this time, the central African plate shed sediments to the north-northwest across episodically flooded pediplains into these basins (Guiraud et al., 2005). By the Late Ordovician, northeastern Africa was near the south pole, and was glaciated from the latest Ordovician to early Silurian (Badalini et al., 2002; Ruban et al., 2007).

The Paleozoic and Mesozioc tectonic evolution of northern Africa can be described in terms of the evolution of the Tethys oceans and associated rifting. Closure of the Paleotethys is associated with the Laurasia-Gondwana collision, which may have begun as early as the Middle Devonian (Boote et al., 1998), but most collision-related deformation was manifested during multiple stages of Hercynian orogenesis during the latest Carboniferous to Early Permian

(Guiraud et al., 2005). Closure of the Paleotethys occurred from west to east, with maximum deformation at the western end of the suture zone (Ziegler, 1989; Guiraud et al., 2005). During the Late Carboniferous and Early Permian, immediately following closure of the Paleotethys, rift basins began to form along the northern margin of Africa, marking the onset of opening of the Neotethys Ocean (Stampfli et al., 2001b; Stampfli and Borel, 2002; Guiraud et al., 2005), and extensional faulting occurred from the Permian through the Jurassic (Guiraud and Bosworth, 1999).

3.3 Mesozoic Evolution and Supercontinental Breakup

Phanerozoic basin development in northeastern Africa was influenced by poly-phase rifting associated with the break-up of Pangaea through reactivation of suture zones (Guiraud et al., 2005). Rifting began in the Late Carboniferous, and associated basin development began in the Early-Middle Jurassic with the opening of the central Atlantic Ocean (Bumby and Guiraud, 2005). Rifting continued through the Jurassic, or to possibly as late as the Early Cretaceous (Ziegler, 1989; Guiraud and Bosworth, 1999; Badalini et al., 2002; El Awdan et al., 2002; Bumby and Guiraud, 2005). A divergent plate margin was developed between Gondwana and Laurasia, along which multiple phases of rifting and inversion ensued (Ziegler, 1989; Badalini et al., 2002). Extensional horst and graben faulting of Paleozoic to Triassic sediments was dominant in the Middle Jurassic (Fig. 2). Synrift and postrift deposits within rift-related basins contain potential source and reservoir rock that were exposed to Late Cretaceous transpressive faulting. This caused contractional reactivation of pre-existing normal faults (El Awdan et al., 2002).

The development of a passive margin along the northeastern coast of Africa may have begun as early as the Bathonian (Keeley,1994), or as late as the Early Cretaceous (Stampfli, 2001). North Africa and Europe converged during the Early Cretaceous, followed by Aptian rifting (Badalini, 2002). Late Cretaceous and Paleogene intraplate contraction associated with the East Mediterranean Rift created half-grabens along the margin in northern Egypt (Guiraud et al., 2001; Stampfli, 2001). This was followed by Santonian dextral transpression across northeastern Africa (Guiraud and Bosworth, 1999), inverting basins from Morroco to Oman (Bosworth, 2008).

4. Northern Western Desert Stratigraphy

The stratigraphic record of the northern Western Desert is characterized by crystalline basement overlain by Paleozoic sandstones, in turn overlain by a northward-thickening Mesozoic-Tertiary sedimentary wedge (Said, 1962; Sestini, 1984; Fig. 2). The stratigraphy encountered in the Heqet-2 well is consistent with the regional stratigraphy outlined by Figure 3. It records the complete stratigraphic section from the Jurassic Safa Formation through the Miocene Marmarica Formation at the surface. The Sokar-1X well penetrates Cambrian through Miocene strata. It contains an erosional unconformity at 13,100 ft that omits Silurian through lower Cretaceous (lower Hauterivian) strata, such that the Shifa Formation is overlain by the early Cretaceous Alam El Bueib Formation (Unit 3). Mesozoic units above the unconformity are up to 10 km thick, and thin to the south from the current passive continental margin (Stampfli et al., 2002). Since the Silurian-Triassic section is not preserved in the Sokar-1X well and the Hequet-2 well does not penetrate to the Triassic, the Silurian-Triassic section will not be discussed.

In the study area, including the Faghur Basin in the northern Western Desert, undifferentiated sandstones of the Cambrian-Ordovician Shifa Formation unconformably overlie Precambrian basement. The post-Paleozoic succession comprises four major cycles, beginning with fluvio-deltaic siliciclastics and ending with marine shales and limestones. The Lower-Middle Jurassic Khatatba Formation is comprised of a series of fluvial deltaic siliciclastic deposits that grade up section into marine shales and limestones (Keeley and Wallis, 1991). In some areas in the northern Western Desert, the Khatatba Formation is a prolific oil and gas reservoir (Rossi et al., 2001). The Safa Member is a source rock that is a zone of interest in the Hequet-2 well.

The Cretaceous through Middle Eocene record is dominated by fluvial through shallow marine deposits. Prior extensional faulting related to rifting created accommodation space, allowing for deposition of a thick succession of fluvial to shallow marine sandstones. These are recorded in the Lower Cretaceous Alam El Buib through Kharita formations (Sestini, 1984). The earliest Late Cretaceous Bahariya Formation (Early Cenomanian) contains multiple paralic sequences of facies ranging from fluvial-deltaic to shallow marine deposits (Sestini, 1984; Khalifa and Catuneanu, 2008). Overlying this is the Abu Roash Formation (Upper Cenomanian to Coniacian), which is dominated by shallow marine carbonates and mudstones (Barr, 1968; Sestini, 1984), and the Khoman Formation (Santonian to Campanian) and Appollonian Formation (Paleocene to Middle Eocene) middle to outer neritic carbonates (Sestini, 1984). Regional subsidence since the Middle Eocene has resulted in deposition of deeper-water facies (Rossi et al., 2001). The Dabaa Formation (Late Eocene to Oligocene) consists of open marine shales, and is overlain by the Mohgra Formation (Miocene) dominated by fluvio-deltaic facies (Sestini, 1984).

5. Methodology

5.1 Sampling

Apache Egypt collected drill cuttings every 10 ft while drilling all sandy formations that were expected to contain detrital zircon. From approximately 2,000 to 6,000 feet measured depth, shale, limestone and dolomite are the dominant lithology, so no samples of cuttings were collected in this interval. The Shifa Sandstone, Alam El Buib Formation, Kharita Formation, Bahariya Formation and Mohgra Formation from the Sokar-1X and the Safa Member of the Khatatba Formation in the Heqet-2 were sampled. Most samples were received in water-based drilling mud, but several of the deeper samples contained up to 10% diesel fuel that was added to stabilize the wellbore while drilling. Many hours were spent decanting samples to remove fine-grained drilling mud and diesel fuel. Groups of three adjacent samples were combined and amalgamated to maximize the amount of zircon from a given sample, resulting in a total of 66 samples, each representative of 30 ft of stratigraphic section. Only samples within the same formation were combined to mitigate cross-sampling of different formations.

Several sampling complexities associated with borehole cuttings need to be mentioned. Cuttings travel from the drill bit to the surface through circulating drill mud. Individual samples contain chips of rock and sand broken loose by the bit and mixed with cuttings from adjacent rocks, so some homogenization of grains occurs over a certain interval, and the risk of contamination of grains is elevated by dislodging of grains from overlying strata during circulation. Drilling presents several concerns including cave-ins, sustained laminar flow of drill mud, contact of the drill string with the exposed uncased borehole, etc. that may dislodge sediment and contaminate a sample of drill mud.

5.2 (U-Th)/He Thermochronology

(U-Th)/He dating is based on the decay of ^{235}U, ^{238}U, ^{232}Th, and to a lesser extent ^{147}Sm, to produce radiogenic ^{4}He nuclei through alpha-decay series to their respective daughter nuclides ^{207}Pb, ^{206}Pb, ^{208}Pb and ^{143}Nd. During an alpha decay event, a ^{4}He nucleus is ejected with energy up to ~8 MeV (Farley et al., 1996). This energetic ejection translates into average stopping-distance in zircon of ~16.7 microns, ~19.6 microns, and ~19.3 microns for respective parent nuclides of ^{235}U, ^{238}U and ^{232}Th (Farley et al., 1996) and ~6 microns for ^{147}Sm (Hourigan et al., 2005). It is necessary and standard procedure to apply a statistical correction that accounts for grain geometry and mineral density to determine the fraction of alpha particles ejected from the grain by parent nuclides near the grain boundary (Farley et al., 1996; Farley, 2002). The alpha-ejection correction, or F_T correction, accounts for the fraction of potentially ejected alpha particles within approximately 20 μm of the rim of the grain. This reduces the raw age to a meaningful (U-Th)/He age. Helium retention in a thermochronometer is dependent on the mineral-specific diffusion coefficient and temperature (Farley, 2002; Reiners et al., 2002; Meesters and Dunai, 2002). Helium is differentially retained across a range of temperatures. This temperature range is specific for different thermochronometers, and is referred to as a partial-retention zone (PRZ). At temperatures above the partial retention zone, all ^{4}He is lost, resetting the zircon helium (ZHe) age to zero, and below the PRZ no ^{4}He is lost through thermal diffusion. The partial retention zone for zircon (ZHe PRZ) is ~120 to ~180°C (Tagami et al., 2003; Reiners, 2005; Stockli 2005). The maximum temperature at the bottom of the Sokar-1X borehole is ~130°C, which indicates zircon is an ideal low-temperature thermochronometer

compared to others, which have lower temperature range PRZs (apatite (U-Th)/He, zircon fission track, apatite fission track, etc.).

In this study, single zircon crystal aliquots were heated using a Nd-YAG laser to 1285°C to extract helium. ^{4}He was spiked with a known amount of ^{3}He and a ratio was determined using a quadrapole mass spectrometer. Zircon grains were dissolved through a standard pressure vessel dissolution procedure in multiple steps using hydrofluoric and then hydrochloric acids. Dissolved zircons were spiked with known quantities of ^{235}U, ^{230}Th and ^{149}Sm and analyzed for ^{238}U, ^{232}Th and ^{147}Sm using inductively coupled mass spectrometry. The helium age equation was solved iteratively using in-house software and corrected for alpha-ejection based on 3D zircon measurements, and results are shown in Tables 1 and 2.

5.3 Detrital Zircon (U-Th)/He Thermochronology

Zircon (U-Th)/He was the thermochronometer chosen in this study due to the advantages it offers over several other low-temperature thermochronometers (described above) when applied to detrital studies. This technique can be used to elucidate the timing of geologic processes such as tectonic uplift or erosional exhumation that typically cannot be dated by U-Pb crystallization ages while providing higher precision than other low-temperature techniques such as ^{40}Ar/^{39}Ar and DZFT techniques. Because zircon is a robust mineral that is resistant to weathering and mechanical abrasion and is well preserved in many sedimentary rocks, it is an ideal geochronometer and thermochronometer in detrital studies.

As with all low-temperature thermochronometers, the temperature history of the zircon during sedimentary transport and burial is critical to the interpretation of the DZHe age. The data obtained in this study (described below) required two different methods of interpretation.

DZHe ages below the unconformity are younger than the depositional ages, so they have been reset by burial below the depth where the thermal gradient exceeds the ZHe closure temperature. These ages constrain the exhumation age prior to erosion of the paleo-structural-high in the Sokar-1X vicinity. Above the unconformity, most DZHe ages exceed their respective depositional ages while only a few are nearly equal to their depositional age. This indicates that zircons above the unconformity were not thermally reset by burial and the unconformity is a barrier that separates two distinct groups of zircons that must be interpreted differently.

Within the two regions of data, there are few outlier ages that do not conform to the defining characteristics of their group. These were isolated and removed from interpretation using two filters based on alpha-radiation dosages, described in detail below. The first filter eliminates metamict grains, mainly from zircon below the unconformity, that have significant helium-loss due to severe radiation damage. The second filter eliminates ages not representative of a closed system by comparison with present day helium-concentration and expected alpha dosage; these include grains exhibiting either excess helium or helium loss.

5.4 Detrital Zircon Complexities

5.4.1 Abrasion

Most samples in this study contain a heterogeneous supply of zircon grains with different crystal habits and variable size and roundedness. Detrital zircons are mechanically abraded during transport from their source terrane to their depositional environment. Detrital zircons within individual samples from the Sokar-1X and Heqet-2 boreholes have variable degrees of roundness, ranging from euhedral to well-rounded (Fig. 4). Since negligible abrasion occurs during standard mineral separation, any mechanical abrasion is considered to be due to sedimentary transport. An attempt was made to relate the degree of roundedness to separate age

populations. However, no such correlation is evident. Grains with different degrees of roundness contribute ages within all major populations. Furthermore, it is possible that euhedral grains freed during mineral separation may have 'hitchhiked' as inclusions within coarser quartz grains or compound grains, reducing or preventing any transport abrasion. Grains with different degrees of abrasion could then have originated from the same terrane. Based on this interpretation, it is not possible to reliably relate degree of roundedness to proximity of source terrane. Rounded grains may also require a modified F_T correction depending on the severity of grain rounding or timing of abrasion during transport. Euhedral to sub-euhedral grains were preferentially selected during picking to reduce error associated with F_T correction.

5.4.2 Sample Bias

To ensure a reliable analysis, (U-Th)/He analysis requires that grains be hand-picked, ensuring the selection of the best quality grains, free of inclusions, fractures, and of adequate size (70-100 μm diameter). Non-random grain selection in this technique has potential to eliminate possible age populations. The edges of the grain are removed during transport, resulting in an overcorrection when the standard 20 μm F_T correction is applied. Perhaps future studies involving modeling and advanced measuring of grain roundedness will eliminate this F_T correction error in detrital samples, however the difference in sample ages in this case would be near to or less than standard error.

5.5 Radiation Damage

Radiation damage caused by the decay of parent nuclides can potentially cause significant error in (U-Th)/He analysis if undetected. Uranium and thorium lose alpha particles

during several steps of decay to their respective lead isotopes. During alpha decay, most of the 4.0-6.0 MeV alpha-particle ejection energy is dissipated by alpha-particle ionization over 10-30 μm dislocating ~100 atoms. The lower 70 keV alpha-recoil energy of the larger ^{234}Th and ^{238}U is dissipated over only 30-40 nm but dislocates ~1000 atoms (Weber, 1993). It is the recoil of larger nuclides that creates significant radiation damage. Overlapping regions of dislocated atoms can develop into networks of distorted crystal lattices and eventually, with enough decay, become metamict or completely amorphous. These networks provide fast diffusion passages, allowing ^{4}He to escape more rapidly and at lower temperatures than in lower-radiation grains.

The amount of radiation damage on zircon limits the retentiveness of zircon with respect to helium. Final damage to the crystal is both time and temperature dependent due to recrystallization and thermal annealing of distorted diffusion domains (Weber et al., 1997). More damage occurs in grains with relatively high uranium concentration or in relatively old grains. In metamict grains large nuclides such as lead can diffuse out of zircon, but fortunately uranium is retained (Horie et al., 2006) and can be used to calculate alpha dosages. The amount of radiation damage can be quantified by calculating alpha-dose using the helium age equation (equation 1) which includes concentration information for uranium and thorium to calculate concentration of alpha-events per mass of zircon. Palenik and others (2003) present a range of damage from crystalline to completely amorphous in a single zircon grains over a narrow dose range of 2.1 to 10.1 x 10^{15} alpha-decay events/mg. However, Nasdala and others (2004) report helium retention in slightly to moderately metamict grains and significant helium loss only in strongly metamict zircon with alpha-dosage greater than ~3.5 x 10^{18} events.

Moderate to highly metamict grains are subject to helium loss and therefore yield younger ages, so the necessity of picking metamict grains for (U-Th)/He analysis is avoided.

Pitting and abrasion on the surface of detrital grains can conceal moderate amounts of radiation damage while picking with a light microscope, and minor amounts of radiation damage are usually undetectable. It is therefore necessary to determine a relative amount of radiation damage in individual detrital zircon grains. For this study, a filter described in detail below was successfully designed to eliminate ZHe ages for grains that were considered moderately to highly metamict. Typical natural zircon uranium concentrations are less than 5,000 ppm (Ewing et al., 2005). Sokar-1X detrital zircons had uranium concentrations ranging from ~50-500 ppm with few outliers and an average of ~170 ppm. All grains with uranium concentrations greater than 400 ppm had alpha-dosages greater than 3.0×10^{16} events/mg.

5.6 Alpha-Dosage Filter

As discussed above, radiation damage from alpha decay can cause significant helium loss in zircon, and abrasion from detrital transport can make this difficult to discern. Therefore, it is extremely beneficial to calculate alpha-dosage for suspected metamict grains. From the Sokar-1X data, several ZHe ages from the Paleozoic strata below the unconformity (Fig. 5) contain ages younger than the Mesozoic strata above the unconformity. These ages are obviously erroneous outliers and others were suspected, so alpha-dosages were calculated for all ZHe ages. Alpha dosages based on 200 Ma of radioactive decay reveal that most zircons have fewer than 3.0×10^{16} events/mg (Fig. 6), but 13 of the 274 ZHe analyses experienced doses over this limit. These grains are interpreted to be moderately to highly metamict and thus yield ages that are too young. These grains are omitted from probability density plots to avoid representing an erroneous zircon population. This only eliminates ages that are too young and mostly eliminates ages from samples below the Paleozoic-Mesozoic unconformity. This primary filter is designed

to eliminate all grains that are significantly metamict due to extensive radiation damage from old or high-uranium grains. Applying filters to the non-reset zircon is similar to eliminating discordant U-Pb ages; the filter removes grains that do not represent a closed system.

5.7 Alpha-Dosage versus Helium Concentration Filter

Several possible mechanisms associated with detrital-zircon transport can potentially modify the helium-concentration profile and translate the location of a population of ZHe ages in probability density plots. A secondary filter was created in an attempt to determine which populations are problematic and may have been translated from their true location. This filter is designed to determine if individual grains skew from the theoretical linear relationship between alpha-dosage and retained helium concentration (Fig. 7). In an ideal closed system, there should be a linear relationship (line of best fit) between the alpha-dosage and helium concentration. Two possible deviations from the linear relationship are defined were problematic ages have either relative excess helium or helium deficiencies caused by loss of either parent or daughter component from the system. Helium deficiency is characteristic of metamict grains, but other factors may also be responsible (ie. fractures, inclusion sinks, recycled grains, etc.). Therefore, helium-deficient grains are likely, but not necessarily, due to metamictization. Grains containing excess helium are not fully understood in detrital systems, but could be due to removal of uranium-rich rims during transport or implantation from "bad neighbors" at source.

Filter 2 is very aggressive and may in fact over-filter meaningful data. It is difficult to define what constitutes an outlier on this plot. Therefore, the filtered data is presented here for potential future work, but does not significantly impact the core interpretations of this study. This filter is only applicable to grains that have not breached the closure temperature during

burial (not reset), so filter 2 has only been applied to those aliquots with ages older than depositional ages. Since filter 2 is far more aggressive than filter 1, and significantly reduces the number of analyses in some sections, probability density plots display results following application of both filters. Interpretations of the probability-density plots below mainly consider the results of the alpha-dosage filter.

6. Results

6.1 Detrital Zircon (U-Th)/He Data

Detrital Zircon (U-Th)/He ages were collected from the entire span of the Sokar-1X borehole (Fig. 3), excluding the interval from ~2,000-6,000 ft of dominantly carbonate and mudstone, which was not expected to yield zircon. The data are divided into two zones. The zone above the major unconformity at 13,100 ft contains ZHe ages older than depositional ages of the Mesozoic and Cenozoic strata. The zone below the unconformity contains depositional ages of Paleozoic strata predating ZHe ages. The data above the unconformity have been further separated into sections based on stratigraphic formations to identify populations of exhumed source rock comprising basin fill. These subdivisions provide convenient intervals of sufficient quantity of data to be analyzed in cumulative probability density distributions that show major source components for their corresponding sedimentary formations. To supplement part of the omitted section from the Sokar-1X unconformity, 27 additional aliquots from the Upper Safa Member of the Khatatba Formation in the Heqet-2 borehole were also analyzed. Figure 5 reveals significant spread in ages for most stratigraphic intervals. Some stratigraphic intervals only meters thick contain ZHe ages ranging from ~100 Ma to over 600 Ma. Cumulative probability

density diagrams were created to investigate multiple ZHe age populations within particular stratigraphic intervals.

6.2 Probability Density Diagrams

The use of cumulative probability density distributions is standard practice for isolating data populations in a variety of thermochronologic investigations involving detrital mineral phases (Fedo et al., 2003). Detrital zircons in a single sample of sandstone can originate from different source terranes, sometimes up to thousands of kilometers away, and can display a significant amount of spread in their respective ZHe ages if they are not reset during burial. To isolate specific populations within the spread, cumulative probability density distributions for ZHe ages were prepared using Isoplot software (Ludwig, 2003).

6.3 ZHe Data Presentation

Zircon helium ages (ZHe) vs. depth show two main groups of data that are treated differently in terms of data presentation and interpretation. (1) Above the Paleozoic-Mesozoic unconformity ZHe ages are older than stratal ages. These are treated as "un-reset" zircons in contrast to (2) ZHe ages below the unconformity, which are younger than the depositional age of their host rocks. The alpha-dosage filter (filter 1) described above was applied to all samples, but only affected Sokar-1X Paleozoic and Lower Alam El Buib (AEB) members and Heqet-2 Jurassic samples. Filter 2 was designed for and applied only to samples with ZHe ages older than the depositional age of their source rock (Sokar-1X above the Paleozoic-Mesozoic unconformity and Heqet-2 Jurassic samples).

6.3.1 Sokar 1-X Paleozoic Strata

All ZHe ages from Paleozoic sediments have ZHe ages younger than the depositional ages of their host rocks. Paleozoic strata below the major unconformity at 13,100 ft MD to the total depth of 15,400 ft are of Cambrian to Ordovician Shifa Formation with ZHe ages ranging from 36 to 450 Ma. Application of the alpha-dosage filter removes several anomalously young ZHe ages less than 150 Ma. A frequency distribution plot of 44 ages from this interval reveals major populations of Devonian, Carboniferous and Permian zircons and minor populations of Triassic and Jurassic zircons (Fig. 8).

6.3.2 Sokar 1-X Mesozoic and Cenozoic Strata

Above the Paleozoic-Mesozoic unconformity at 13,100 ft is ~10,000 ft of Cretaceous rocks capped by ~3,000 ft of Cenozoic rocks that have ZHe ages older than their depositional ages. Forty-one analyses from the Hauterivian to Barremian Alam El Buib Formation (Units 3-1), from 9,080 to 13,100 ft, display a range of unfiltered ZHe ages from 662 to 67.9 Ma. Major peaks are found in Cambrian (~525 Ma), Silurian (~430 Ma), Late Devonian to Carboniferous transition (~350 Ma) populations and minor peaks are found in Precambrian (~575 Ma), Permian (~280 Ma), Triassic (~250 Ma), Jurassic (~195), and Cretaceous (~70 Ma) populations. Alam El Buib (AEB) samples are divided into two sections for population distribution analysis in order to identify any population changes between the lower and upper members. Lower members 3C-3G, from 13,100 to 12,000 ft, (Fig. 9a) show strong Silurian (~430 Ma) and Late Devonian (~358 Ma) populations and several minor populations in the Cambrian (~530 Ma), Carboniferous (~302 Ma), Triassic (250 Ma), and Jurassic (~195 Ma). Filters 1 and 2 completely remove the minor Cretaceous population and slightly reduce both the Triassic and Jurassic populations.

Upper AEB members 1-3C contain 41 analyses with several populations ranging from Precambrian to Jurassic (Fig. 9b). A major population centered in the Devonian (~400 Ma) contains several major subpeaks in the Cambrian (~530 Ma), Ordovician (~475 Ma), and Carboniferous (~350 Ma). Minor populations include those in the Precambrian (~650 Ma), Permian (~275 Ma), and Jurassic (~175 Ma). Application of the alpha-dosage filter has no effect on this interval, while filter 2 removes the minor populations at ~650 and ~175 Ma.

Above the AEB formation, are the Aptian-age Alamein Dolomite overlain by the Aptian-age Dahab Shale (8,180-9,080 ft), which are dominated by carbonates and mudstones respectively. Only one sample from this interval yields 3 Cambrian to Ordovician ZHe ages (521.5 +/- 41.7; 481.4 +/- 38.5; and 466.4 +/- 37.3 Ma). Three ZHe ages are not enough to construct a meaningful probability density distribution and likely do not represent all age populations, so this formation is not interpreted below.

The Albian-age Kharita Formation contains a major population centered in the Late Ordovician (~450 Ma), with major subpeaks in the Cambrian (~530 Ma) to the Early Devonian (~410 Ma; Fig. 9c). A major component is also prominent in the Carboniferous (~340 Ma). Minor components are present in the Precambrian (~700 Ma), Carboniferous to Permian transition (~290 Ma), Jurassic (~160 Ma) and Cretaceous (~120 Ma). Filter 2 removes only the Precambrian and Jurassic populations, reduces the Cretaceous population and does not affect the other major populations.

The Cenomanian-age Bahariya Formation (5,660-6,340 ft) contains two major peaks in the Ordovician (~480 Ma) and Silurian (~430 Ma) (Fig. 9d). There is a possible subpeak in the Cambrian (~530 Ma). Several minor populations are present from the Carboniferous to the Jurassic, but several are removed by filter 2 to leave only Carboniferous (~350 and ~300 Ma)

and Jurassic (~170 Ma) populations. Above the Bahariya Formation lie Cretaceous Abu Roash Formation and Cenozoic Khoman Apollonia and Dabaa formations from 5,660-1,700 ft. They are composed mainly of mudstones and carbonates and consequently were not sampled.

The Early Miocene Moghra Formation (Fig. 9e) from 750-1,700 ft contains a high frequency of minor populations from the Precambrian to the Miocene and no obviously dominant populations such as are present the units below. Filter 2 eliminates all populations younger than a population at the Permian-Triassic transition (~250 Ma), reducing the number of ZHe ages dramatically from n=36 to n=23. Significant populations removed by filter 2 include Jurassic (~200 Ma) and Cretaceous (~140 and ~90 Ma). The filtered Moghra data contains major Cambrian (~510 Ma), Devonian (~410 Ma), Carboniferous (~340 Ma), and Permian (~290 Ma) populations. Above the Moghra Formation, a 750ft cap of Marmarica Limestone to the surface was not sampled.

6.3.3 Heqet-2 Jurassic Strata

All Heqet-2 samples are from the Upper Safa Member of the Khatatba Formation. ZHe ages from this unit are all older than depositional age with the exception of one metamict Late Cretaceous age which is eliminated by the alpha-dosage filter. Major age populations include Devoinian (~380 Ma), Carboniferous (~350 and ~310 Ma), Permian (~250 Ma), Triassic-Jurassic transition (~200 Ma) and Jurassic (~180 Ma) (Fig. 9f). Application of filter 2 reduces the magnitude of nearly all populations, but does not completely remove any population. Filter 2 also severely reduces the number of analyses for this section from n=26 to n=18. All populations that are not completely removed by filter 2 are meaningful, so filter 1 is sufficient for this interval.

7. Discussion

7.1 Basal Cretaceous Unconformity

ZHe ages below the basal Cretaceous unconformity at 13,100 ft are younger than depositional age, indicating that these units were, at some time, buried to a depth where the temperature exceeded 180°C. The erosional nature of the unconformity suggests that erosional unroofing brought these zircons to a shallower depth, where the geothermal gradient was less than the ZHe closure temperature. These Cambrian-Ordovician sandstones contain a dominant population of ZHe ages that peaks in the Late Carboniferous (320 ±26 Ma) (Fig. 9). Therefore, Paleozoic strata below the basal Cretaceous unconformity underwent major exhumation in the Carboniferous (~350-290 Ma), cooling from >180°C to <140°C. Zircons were then buried by subsequent Mesozoic-Cenozoic deposition, but never deep enough to have exceeded the closure temperature.

Hercynian deformation of northern Africa associated with closure of the Proto-Tethys ocean consists of faulting and folding in northwest Africa, with decreasing magnitude toward the east, which led to widespread Late Carboniferous unconformities (Badalini et al., 2002). Carboniferous contractional deformation implied by this study supports evidence from Guiraud and others (2005) of the first stage Hercynian deformation occurring around the Devonian-Carboniferous transition. Furthermore, the presence of two Hercynian-related components (~350 and 300 Ma) in Mesozoic strata above the unconformity supports two main stages of Hercynian orogenesis within the peak range of Hercynian orogenesis in northern Africa during the latest Carboniferous to earliest Permian as discussed by Guiraud and others (2005).

Complete Jurassic stratigraphy is present in the nearby Heqet-2 well. These Jurassic sandstones include a major population of ZHe ages (~350 Ma) indicating that sediments were being shed off a fault block exhumed in the Carboniferous and transported into the Jurassic basin. This implies an onlap relationship of Jurassic rocks in the Heqet-2 area onto the Sokar-1X paleo-structural-high. The basal Cretaceous unconformity in the Sokar-1X well is not regionally observed (Fig. 3), so the unconformity must be a local feature isolated to at least one and possibly other fault blocks bounding Jurassic basins in the northern Western Desert. Therefore, the basal Cretaceous unconformity represents a period of localized non-deposition, uplift and erosion from the Carboniferous through the Jurassic. Within Jurassic samples of the Heqet-2 well, Jurassic and Triassic DZHe populations indicate an alternate provenance of Triassic to Jurassic rift-related features. It is unknown if rifting reactivated the Sokar-1X paleo-structural-high during this period; reactivation may not provide enough structural throw to exhume, and reset zircon and Hercynian age components would still dominate.

7.2 Dominant Provenance Components

Deconvolution of all ZHe populations derived from 2x-filtered ZHe ages from units above the Paleozoic-Mesozoic unconformity in the Sokar-1X well and the Heqet-2 Jurassic strata reveal ten major populations (Fig. 10). The peaks may be correlated to tectonically driven exhumation of major regional source terranes. Peaks were extracted from population density plots described above and were grouped into population intervals based on overlap of the 8% standard error window. Population peaks were averaged for overlapping intervals for all sections of samples with ZHe ages older than depositional ages to identify general component age to represent the timing of source-rock cooling (Fig. 11). The components' general timing and range

of standard error are as follows: (1) Precambrian component at 584 ±47 Ma, (2) Early Paleozoic component at 529 ±42 Ma, (3) Early Paleozoic component 493 ±39 Ma, (4) Early Paleozoic component at 446 ±36 Ma, (5) Devonian component at 404 ±32 Ma, (6) Early Carboniferous component at 349 ±28 Ma, (7) Carboniferous component at 295 ±24 Ma, (8) Permian-Triassic component at 250 ±20 Ma, (9) Triassic-Jurassic component at 201 ±16 Ma, and (10) Jurassic component at 171 ±14 Ma. Additional components corresponding to geologic events other than provenance exhumation will also be discussed.

7.2.1 Precambrian Components

Precambrian components are sparse within Mesozoic and Cenozoic strata, but are minor components (584 ±47 Ma) in AEB and Moghra formations. Filter 2 removes other Precambrian populations from upper AEB members *(ZHe ~650 Ma)* and the Kharita Formation *(ZHe ~700 Ma)* that may be correlative to synorogenic magmatism or tectonic exhumation during the final stages of Late Paleozoic assembly of Gondwana. Late Pan-African-Brasilian orogenesis (720-580 Ma) related to assembly of Gondwanaland (Unrug, 1996; Caby, 2003; Guiraud et al., 2005) produced contractional suture belts. Exhumed terranes from these orogenic belts could have shed sediment into this region directly. However, if stored in other sedimentary basins at low temperatures and then shed into the local basin having not been partially reset or not reset, these Precambrian components could represent second-cycle ZHe ages.

7.2.2 Early Paleozoic Components

Component 2 at 529 ±42 Ma may correspond to post-collisional magmatism or exhumation associated with rejuvenated N-S strike-slip zones following the Pan-African event

(Guiraud et al., 2005). Pan-African structural fabrics later facilitated subsequent strain beginning in the Mid-Cambrian (Keeley, 1994). Magmatism was also active during this time; Paquette and others (1998) determined the Tioueine pluton from the Tuareg Shield in Hoggar (U-Pb age 523 ±1 Ma) formed as a result of N-S shearing that affected most of northern Africa at the time.

7.2.3 Hunic Rifting Components

A major ZHe population exists in AEB, Kharita, and Bahariya sections at 446 +/- 36 Ma, but it is unclear where the 450 Ma ZHe age population originates. A possible explanation is exhumation related to rifting of the Hunic Superterrane in the Late Ordovician. Stampfli and others (2002) claim the Hunic superterrane rifted from northern Africa and collided with other terranes rifted from Eurasia to form the first Variscan orogenic events in the Middle Devonian. These amalgamated terranes continued north to collide with Eurasia in a second orogenic event in Visean time (Stampfli et al., 2002), and final collisions of Gondwana with Eurasia occurred after the Early Carboniferous in the Alleghanian orogeny. Another possible sediment transport mechanism is glaciation during the Late Ordovician. At this time Northern Africa was at the South Pole, and glaciers extended up to northern Africa (Badalini et al., 2002; Ruban et al., 2007).

7.2.4 Hercynian Components

Components 6 and 7 can be correlated to multiple stages of contractional deformation during Hercynian orogenesis. Component 6 (349 ±28 Ma) corresponds to contractional deformation along the northern and western African Platform and Arabian plate during the Devonian-Carboniferous transition (Guiraud and Bosworth, 1999) and represents the first stage

of the Hercynian Orogeny (Guiraud et al., 2005). Component 7 (295 +/- 24 Ma) is present as a minor component in all stratigraphic units and corresponds to a second phase of Hercynian contraction.

Carboniferous collision between Gondwana and northern continents uplifted large portions of the northeastern African Plate creating east-west-striking faults and magmatic intrusions, reversal of the main drainage direction to the south and erosion of Paleozoic sediments in middle and southern Egypt (Klitzsch, 1986; Badalini et al., 2002). Hercynian deformation of northern Africa associated with closure of the Proto-Tethys ocean consists of faulting and folding in northwest Africa, decreasing to the east, and widespread Late Carboniferous unconformities (Badalini et al., 2002). Initial collision of Gondwana with Laurasia is evident from first stage Late Carboniferous Hercynian Orogenesis (Badalini et al., 2002). Although, according to Klitzsch (1986) uplift and erosion of Paleozoic sediments was limited to southern Egypt, the Sokar-1X borehole is evidence of one and possibly other fault blocks of Paleozoic sediments being faulted and forming paleo-structural-highs exhumed during the Carboniferous. A minor Permian-Triassic transitional component population of ZHe ages occurs in Safa, Lower AEB, and Mohgra sections at 250 ±20 Ma. This may correspond to a late Permian tectonic event.

7.2.5 Triassic-Jurassic Components

The lower members of the AEB Formation contain Jurassic and Triassic components that are reduced slightly by filter 1 and significantly by filter 2. Filter 1 removes moderately metamict grains from this population. Grains removed by filter 2 demonstrate He-loss as well, indicating that the filter may be too aggressive, as it removes slightly metamict grains that would still offer

meaningful ages. Oddly, the removal of metamict grains (younger ages than expected) shifts the population peaks in the younger direction, but the peak is not shifted beyond standard error of a single analysis.

Components 9 and 10 have Triassic and Jurassic population averages of 201 ±16 Ma and 171 ±14 represent the ages of an exhumed fault block just prior or during the deposition of the Safa Sandstone. This component persists in lower AEB, but is not present in the upper AEB units indicating that the source has been removed from prolonged erosion during deposition of the AEB formation. The Jurassic component reappears as a minor population in the Bahariya Formation, but may have been recycled from another source.

The presence of Triassic and syndepositional Jurassic ZHe ages within the Jurassic strata of the Heqet-2 well indicates multiple stages of exhumation of another major source terrrane. This is consistent with multi-phase breakup of Pangea beginning as early as the Permian and continuing into Middle Jurassic (Ziegler, 1989; Badalini et al., 2002). Triassic-Jurassic DZHe components are consistent with source terrane exhumation or eruption during rift tectonism.

7.2.6 Late-Cretaceous Component

Surprisingly, ZHe ages around 83 Ma are recorded in the Moghra Formation which records timing of the Santonian contractional overprinting of basins on the northern margin of Africa. These ages are eliminated by filter 2, suggesting that they have been reset, although the source of heat to accomplish this is currently unknown. There was not enough burial to thermally reset any zircons above the 13,000 ft unconformity, so the Santonian age zircons do not represent exhumation during basin inversion, but rather a brief increase in heat during basin inversion. Santonian ZHe ages are likely not derived from volcanic rocks because first cycle

zircons would not be eliminated by Filter 2. A possible heat source is the presence of hot fluids during the Santonian, associated with basin-inversion structures. These Santonian ages further illustrate the danger of using filter 2 to disregard potential ZHe age populations but also show the usefulness of the filter to differentiate non-reset exhumation populations from those reset by other mechanisms. Furthermore, other populations excluded by filter 2 may represent similar contractional events as well.

7.2.7 Volcanic Components

The Kharita Formation contains a minor population of syndepositional ZHe ages at 117 ±9 Ma, indicating volcanic input into the basin. These ages may reflect active volcanism associated with tectonic rifting during continued development of this and other extensional basins. These may be useful to help further constrain depositional ages, but more data is required to conclusively prove this.

7.3 Reconstruction from Provenance Components

The provenance components defined above, combined with interpretation of the timing of the Sokar-1X unconformity, allow a conceptual reconstruction of the local history (Fig. 11). During the Jurassic, erosion of rift-related fault blocks and the Sokar-1X paleo-structural-high contributed sediments to the basin (Fig. 11a). Triassic to Jurassic ZHe populations indicate that exhumed normal fault blocks related to rifting did not occur during a single phase and are likely associated with Triassic pre-rift extension and later Jurassic rifting events. Erosion of the Triassic and Jurassic exhumed fault blocks persisted through deposition of the lower members (3C-3G) of the AEB Formation. Erosional reduction of the Triassic to Jurassic normal fault blocks and

subsequent burial was achieved during the Early Cretaceous within the AEB formation (Fig. 11b-c).

Zircon from the Sokar-1X paleo-structural-high are observed as significant components in all Early Cretaceous units but are only a minor component in the Late Cretaceous Bahariya Formation (Fig. 11d-e). A younger to older shift of the dominant ZHe age populations is observed in successively younger Cretaceous units (Fig. 10). This pattern of successively younger ZHe ages in the stratigraphic column suggests prolonged removal of the paleo-high during Cretaceous time. Furthermore, lack of the Hercynian age component from Late Createous units indicates a shift to Early Paleozoic components derived from older source rock from the Nubian Shield.

The presence of Late Cretaceous DZHe components in the Moghra Formation records the Santonian inversion (Fig. 11f). At this point Hercynian as well as Early Paleozoic components are present. These are likely derived from zircons originating from a terrane that was uplifted and eroded during Santonian contraction, but not reset during exhumation because they were stored at low temperatures (shallow burial).

8. Detrital Zircon Methodology Considerations

8.1 F_T Correction

If detrital ZHe ages are older than depositional ages, then zoning effects may not be realized by applying F_T corrections to partially abraded grains. For example a zircon crystallized during the early Paleozoic will produce helium from all zoned domains in a grain. During transport, mechanical abrasion removes material from the outside of the grain, possibly a domain with differential U-Th concentration. After deposition of the zircon in a Late Cretaceous

sandstone, the zircon will continue to produce helium from a modified U-Th concentration profile. Depending on the degree of abrasion and original U-Th concentration heterogeneity, an individual zircon analysis may not represent a closed system, resulting in helium-excess or helium-deficiency.

It is difficult to quantify the degree of abrasion and estimate the amount of material lost from a detrital zircon. In this study, zircon-picking was biased toward euhedral to slightly abraded grains, but ideal grains are not always available in detrital samples. A standard F_T correction was calculated using the method from 3D measurements of zircon crystals under light microscope with digital imaging and measuring software. As a result, grains picked in the study ranged from euhedral to moderately rounded. An attempt to link the degree of abrasion to individual components did not yield conclusive results. Rounded grains and euhedral grains contributed to most of the ZHe age components.

8.2 Sampling Formations, Members or Beds

There is much still to do in order to perfect the art of statistical sampling of formations, members, or beds. For this study, zircon aliquots were grouped on the order of formations that are, in some cases, on the order of hundreds-of-meters thick. Sediment-dispersal patterns may change on that scale, especially if tectonically influenced sequences exist within a formation. Variation in the dominant components on the scale of members, on the scale of hundreds-of-meters was observed in the ZHe ages from the Alam El Buib Formation. A shift from younger to older mean ages for components in lower to upper members of the Alam El Buib Formation indicates a substantial change in the source of sediment. This may be related to depositional sequences on or within the member scale. For this study, slight age changes with respect to

depth within formations were interesting but not dwelled upon because only dominant components were necessary to link provenance exhumation to tectonic events of northern Africa. A slight change from older to younger ages within a formation could represent prolonged erosional unroofing of source terranes. For future studies, it may be desirable to take high-frequency samples from narrower intervals rather than grouping small sample sizes over a broad range. Sampling individual beds may not be possible due to mixing of cuttings during drill mud circulation; conventional or sidewall cores may provide the quantity of zircon necessary for analysis while representing a fixed sample depth.

9. Conclusions

Advancement of low-temperature thermochronology over the past two decades has paved the way for several techniques applicable to detrital studies where investigation of cooling history of the source terrane is pertinent. Detrital $^{40}Ar/^{39}Ar$ (Hodges et al., 2005; Huntington and Hodges, 2006) and detrital zircon fission track (Bernet and Garver, 2005; Tagami and O'Sullivan, 2005) studies are useful for investigating cooling histories of source terranes, but are not ideal in all situations. Zircon (U-Th)/He thermochronology has been used extensively in geologic and tectonic studies, but has not been widely applied to detrital studies to identify the tectonic history of a source terrane. This case study demonstrates the value of detrital Zircon (U-Th)/He thermochronology as applied to vertical multi-sample arrays designed to isolate populations of zircons exhumed during major regional tectonic events.

The low helium closure temperature of this method allows zircon to record and retain exhumation ages of the source terranes for sedimentary units in a basin. The age signature of detrital zircons from formations can be used to reconstruct the evolution of the source area. This

information may be further applied to sediment dispersal patterns to elucidate sediment inflow from source regimes. In the vicinity of the Sokar-1X borehole, the evolution of detrital populations in the basin can be correlated to major tectonic events occurring thousands of kilometers away. Furthermore, the nature of the ZHe ages within the borehole represent two entirely different regions of data that contribute to structural reconstructions but are interpreted in different ways.

The Sokar-1X borehole penetrates an erosional unconformity that juxtaposes Early Cretaceous over Cambrian-Ordovician strata. Below this basal Cretaceous unconformity, detrital zircon (U-Th)/He ages postdate Paleozoic strata, and support Hercynian related uplift of a fault block during the Carboniferous in the northern Western Desert of Egypt. This paleo-structural-high remained subaerially exposed until Late Cretaceous while contributing sediments into onlapping Jurassic and Early Cretaceous rocks nearby. Above the basal Cretaceous unconformity, probability density distribution analysis of ZHe ages predating Mesozoic-Cenozoic strata elucidates dominant sedimentary provenance components within the formations. Triassic to Jurassic components in the Safa Sandstone and Alam El Buib Formation reveal the presence of a rapidly exhumed fault block associated with Triassic-Jurassic rifting and an onlap relationship of Jurassic rocks onto the Sokar paleo-high. These two types of interpretation show the usefulness of DZHe in a variety of depositional conditions.

REFERENCES CITED

Armstrong, P.A., 2005, Low-temperature thermochronology: techniques, interpretations, and applications: Reviews in Mineralogy and Geochemistry, v. 58, p. 499-525.

Badalini, G., Redfern, J., and Carr, I.D., 2002, A synthesis of current understanding of the structural evolution of north Africa: Journal of Petroleum Geology, v. 25, p. 249-258.

Barr, F.T., 1968. Upper Cretaceous stratigraphy of Jebel El Akhdar, Northern Cyrenaica, *in* BARR, F.T., ed., Geology and Archaeology of Northern Cyrenaica, Libya: Petroleum Exploration Society of Libya, 10th Annual Field Conference, p. 131-142.

Barton, E.S., Compston, W.W., I.S., Bristow, J.W., Hallbauer, D.K., and Smith, C.B., 1989, Provenance ages for the Witwatersrand Supergroup and the Ventersdorp contact reef: constraints from ion microprobe U-Pb ages of detrital zircons: Economic Geology, v. 84, p. 2012-2019.

Bernet, M., and Garber, J.I., 2005, Fission-track analysis of detrital zircon; Low-temperature thermochronology; techniques, interpretations, and applications: Reviews in Mineralogy and Geochemistry, v. 58, p. 205-238.

Biswas, S., Coutand, I., Grujic, D., Hager, C., Stockli, D., Grasemann, B., 2007, Exhumation and uplift of the Shillong plateau and its influence on the eastern Himalayas: new constraints from apatite and zircon (U-Th-[Sm])/He and apatite fission track analyses: Tectonics, v. 26, TC6013.

Boote, D.R.D., Clark-Lowes, D.D., Traut, M.W., 1998. Palaeozoic petroleum systems of North Africa; Petroleum Geology of North Africa: Geological Society of London, Special Publication 132, p. 7–68.

Bosworth, W., El-Hawat, A.S., Helgeson, D.E., and Burke, K., 2008, Cyrenaica "shock absorber" and associated inversion strain shadow in the collision zone of northeast Africa: Geology, v. 36, p. 695-698.

Bumby, A.J., and Guiraud, R., 2005, The geodynamic setting of the Phanerozoic basins of Africa: Journal of African Earth Sciences, v. 43, p. 1-12.

Caby, R., 2003, Terrane assembly and geodynamic evolution of central-western Hoggar: a synthesis: Journal of African Earth Sciences, v. 37, p. 133-159.

Carter, A., 1999, Present status and future avenues of source region discrimination and characterization using fission track analysis: Sedimentary Geology, v. 124, p. 31-45.

Carter, A., and Moss, S.J., 1999, Combined detrital-zircon fission-track and U-Pb dating: a new approach to understanding hinterland evolution: Geology, v. 27, p. 235-238.

DeGraaff-Surpless, K., Graham, S.A., Wooden, J.L., and McWilliams, M.O., 2002, Detrital zircon provenance analysis of the Great Valley Group, California: evolution of an arc-forearc system: Geological Society of America Bulletin, v. 114, p. 1564-1580.

Dodson, M.H., Compston, W., Williams, I.S., and Wilson, J.F., 1988, A search for ancient zircons in Zimbabwean sediments: Journal of the Geological Society, v. 145, p. 977-983.

Ehlers, T.A., and Farley, K.A., 2003, Apatite (U-Th)/He thermochronometry: methods and applications to problems in tectonic and surface processes: Earth and Planetary Science Letters, v. 206, p. 1-14.

El-Menshawy, Z., 2004, Stratigraphic column of the Western Desert: Khalda and Apache Egypt, unpublished data.

El Awdan, A., Youssef, F., and Moustafa, A.R., 2002, Effect of Mesozoic and Tertiary deformations on hydrocarbon exploration in the northern Western Desert, Egypt: American Association of Petroleum Geologists International Meeting Abstract (Cairo).

Ewing, R.C., Meldrum, A., Wang, L., Weber, W.J., and Corrales, L.R., 2005, Radiation effects in zircon: Reviews in Mineralogy and Geochemistry, v. 53, p. 387-425.

Farley, K.A., 2002, (U-Th)/He dating: techniques, calibrations, and applications: Reviews in mineralogy and geochemistry, v. 47, p.819-844.

Farley, K.A., and Stockli, D.F., 2002, (U-Th)/He dating of phosphates: apatite, monazite, and xenotime: Reviews in Mineralogy and Geochemistry, v. 48, p. 559-577.

Farley, K.A., Wolf, R.A., Silver, L.T., 1996, The effects of long alpha-stopping distances on (U-Th)/He ages: Geochimica et Cosmochimica Acta, v. 60, p. 4223-4229.

Fedo, C.M., Sircombe, K.N., and Rainbird, R.H., 2003, Detrital zircon analysis of the sedimentary record: Reviews in Mineralogy and Geochemistry, v. 53, p.277-303.

Guiraud, R. and Bosworth, W., 1999, Phanerozoic geodynamic evolution of northeastern Africa and the northwestern Arabian platform: Techtonophysics, v. 315, p. 73-108.

Guiraud, R., Bosworth, W., Thierry, J., and Delplanque, A., 2005, Phanerozoic geological evolution of Northern and Central Africa: An overview: Journal of African Earth Sciences, v. 43, p. 83-143.

Harris, A.C., Dunlap, W.J., Reiners, P.W., Allen, C.M., Cooke, D.R., White, N.C., Campbell, I.H., and Golding, S.D., 2008, Multimillion year thermal history of a porphyry copper deposit: application of U-Pb, Ar-40/Ar-39 and (U-Th)/He chronometers, Bajo de la Alumbrera copper-gold deposit, Argentina: Mineralium Deposita, v. 43, p. 295-314.

Harrison, T.M., 1985, Sedimentary basin thermal histories through Ar-40-Ar-39 analysis of detrital microcline: American Association of Petroleum Geologists Bulletin, v. 69, p. 263-263.

Hodges, K.V., Ruhl, K.W., Wobus, C.W., and Pringle M.S., 2005, $^{40}Ar/^{39}Ar$ Thermochronology of detrital minerals: Reviews in Mineralogy and Geochemistry, v. 58, p. 239-257.

Horie, K., Hidaka, H., and Gauthier-Lafaye, F., 2006, Elemental distribution in zircon: Alteration and radiation-damage effects: Physics and Chemistry of the Earth, v. 31, p. 587-592.

Hourigan, J.K., Reiners, P.W., and Brandon, M.T., 2005, U-Th zonation-dependent alpha-ejection in (U-Th)/He chronometry: Geochimica et Cosmochimica Acta, v. 69, p. 3349-3365.

Huntington, K.W., and Hodges, K.V., 2006, A comparative study of detrital mineral and bedrock age-elevation methods for estimating erosion rates: Journal of Geophysical Research, v. 111, p. 1-11.

Huntington, K.W., Ehlers, T.A., Hodges, K.V., and Whipp Jr., D.M., 2007, Topography, exhumation pathway, age uncertainties, and the interpretation of thermochronometer data: Tectonics v. 26, p. 1-23.

Hurford, A.J., 1986, Cooling and uplift patterns in the Lepontine Alps south central Switzerland and an age of vertical movement on the Insubric Fault Line: Contributions to Mineralogy and Petrology, v. 92, p. 413-427.

Keeley, M.L., 1994, Phanerozoic evolution of the basins of Northern Egypt and adjacent areas: Geologische Rundschau, v. 83, p. 728-742.

Keeley, M.L., and Wallis, R.J., 1991, The Jurassic system in northern Egypt: II. Depositional and tectonic regimes: Journal of Petroleum Geology, v. 14, p. 49-64.

Khalifa, M.A., and Catuneanu, O., 2008, Sedimentology of the fluvial and fluvio-marine facies of the Bhariya Fornation (Early Cenomanian), Bahariya Oasis, Western Desert, Egypt: Journal of African Earth Sciences, v. 51, p. 89-103.

Klitzsch, E.H., 1986, Plate tectonics and cratonal geology in Northeast Africa (Egypt, Sudan): Geologische Rundschau, v. 75, p. 755-768.

Ludwig, K., 2003, User's manual for Isoplot 3.00, A geochronological toolkit for Microsoft Excel: Berkeley Geochronology Center Special Publication, v. 4.

MacPhee, D., Bowring, S.A., and Reiners, P.W., 2005, Combined (U-Th)/He and U-Pb thermochronometry of rift-flank exhumation in east-central Africa: Geochimica et Cosmochimicha Acta, v. 69, p. A304-A304.

McDougall, I and Harrison, T.M., 1999, Geochronology and Thermochronology by the $^{40}Ar/^{39}Ar$ Method 2nd edition: Oxford University Press, Oxford.

Meesters, A.G.C.A., and Dunai, T.J., 2002, Solving the production-diffusion equation for finite diffusion domains of various shapes, Part II, Application to cases with ejection and nonhomogeneous distribution of the source: Chemical Geology, v. 186, p. 347-363.

Najman, Y.M.R., Pringle, M.S., Johnson M.R.W., Robertson, A.H.F., and Wijbrans, J.R., 1997, Laser $^{40}Ar/^{39}Ar$ dating of single detrital muscovite grains from early foreland-basin sedimentary deposits in India: Implications for early Himalayan evolution: Geology, v. 25, p. 535-538.

Nasdala, L., Reiners, P.W., Garver, J.I., Kennedy, A.K., Stern, R.A., Balan, E., and Wirth, R., 2004, Incomplete retention of radiation damage in zircon from Sri Lanka: American Mineralogist, v. 89. p. 219-231.

Palenik, C.S., Nasdala, L., and Ewing, R.C., 2003, Radiation damage in zircon: American Mineralogist, v. 89, p. 770-781.

Paquette, J.L., Caby, R., Djouadi, M.T., and Bouchez, J.L., 1998, U-Pb dating of the end of the Pan-African orogeny in the Tuareg shield: the post-collisional syn-shear Tioueine pluton (Western Hoggar, Algeria), Lithos, v. 45, p. 245-253.

Rahl, R.M., Reiners, P.W., Campbell, I.H., Nicolescu, S., Allen, C.M., 2003, Combined single-grain (U-Th)/Pb dating of detrital zircons from the Navajo Sandstone, Utah: Geology, v. 31, p. 761-764.

Reiners, P.W., 2005, Zircon (U-Th)/He thermochronometry; Low-temperature thermochronology; techniques, interpretations, and applications: Reviews in Mineralogy and Geochemistry, v. 58, p. 151-179.

Reiners, P., Farley, K., Hickes, H., 2002, He diffusion and (U–Th)/He thermochronometry of zircon: Initial results from Fish Canyon Tuff and Gold Butte, Nevada: Tectonophysics v. 349, p. 297–308.

Reiners, P., Spell, T., Nicolescu, S., Zanetti, K., 2004, Zircon (U–Th)/He thermochronometry: He diffusion and comparisons with Ar-40/Ar-39 dating: Geochimica et Cosmochimica Acta, v. 68, p. 1857–1887.

Reiners, P.W., Campbell, I.H., Nicolescu, S., Allen, C.M., Hourigan, J.K., Garver, J.I., Mattinson, J.M., and Cowan, D.S., 2005, (U-Th)/(He-Pb) double dating of detrital zircons: American Journal of Science, v. 305, p. 259-311.

Ross, G.M., and Bowring, S.A., 1990, Detrital zircon geochronology of the Windermere Supergroup and the tectonic assembly of the southern Canadian Cordillera: Journal of Geology, v. 98, p. 879-893.

Rossi, C., Marfil, R., Ramseyer, K and Permanyer, A., 2001, Facies-Related Diagenesis and Multiphase Siderite Cementation and Dissolution in the Reservoir Sandstones of the Khatatba Formation, Egypt's Western Desert: Journal of Sedimentary Research, v. 71, p. 459-472.

Ruban, D.A., Al-Husseini, M.I., and Iwasaki, Y., 2007, Review of Middle East Paleozoic plate tectonics: GeoArabia, v. 12, p. 35-56.

Said, R., 1962, The geology of Egypt: Elsevier Publisher Company, Amsterdam-New York, 734 p.

Sestini, G., 1984, tectonic and sedimentary history of NE African margin (Egypt-Lybia): Geological Society of London, Special Publication 14, p. 161-175.

Stampfli, G.M., and Borel, G.D., 2002, A plate tectonic model for the Paleozoic and Mesozoic constrained by dynamic plate boundaries and restored synthetic oceanic isochrones: Earth and Planetary Science Letters, v. 196, p. 17-33.

Stampfli, G.M., Borzel, G.D., Cavazza, W., Mosar, J., and Ziegler, P.A., 2001a, Palaeotectonic and palaeogeographic evolution of the western Tethys and Peri-Tethyan domain (IGCP Project 369): Episodes, v. 24, p. 222-228.

Stampfli, G.M., Mosar, J., Favre, P., Pillevuit, A., and Vannay, J., 2001b, Permo-Mesozoic evolution of the western Tethys realm: Neo-Tethys East Mediterranean Basin connection, *in* Peri-Tethys Memoir 6: Peri-Tethyan rift wrench/ basins and passive margins, v. 186, p. 51-108.

Stampfli, G.M., von Raumer, J.F., and Borel, G.D., 2002, Paleozoic evolution of pre-variscan terranes: From Gondwana to the Variscan Collision, *in* Geologic Society of America Special Paper: Variscan-Appalachian Dynamics: The building of Late Paleozoic Basement, v. 305, p. 263-280.

Stockli, D.F., Farley, K.A., and Dumitru, T.A., 2000, Calibration ot the apatite (U-Th)/He thermochronometer on an exhumed fault block, White Mountains, California: Geology, v. 28, p. 983-986.

Stockli, D.F., 2005, Application of low-temperature thermochronometry to extensional tectonic settings.; Low-temperature thermochronology; techniques, interpretations, and applications: Reviews in Mineralogy and Geochemistry, v. 58, p. 411-448.

Stuart, F.M., 2002, The exhumation history of orogenic belts from $^{40}Ar/^{39}Ar$ ages of detrital micas: Mineralogical Magazine, v. 66, p. 121-135.

Tagami, T., and Dumitru, T.A., 1996, Provenance and thermal history of the Franciscan accretionary complex: constraints from zircon fission track thermochronology: Journal of Geophysical Research, v. 101, p. 11,353-11,364.

Tagami, T., and O'Sullivan, P.B., 2005, Fundamentals of fission-track thermochronology; Low-temperature thermochronology; techniques, interpretations, and applications: Reviews in Mineralogy and Geochemistry, v. 58, p. 19-47.

Tagami, T., Farley, K.A., and Stockli, D.F., 2003, Thermal sensitivities of zircon (U-Th)/He and fission-track systems: Geochemica et Cosmochimica Acta, v. 67, p. A466.

Unrug, R., 1996, The assembly of Gondwanaland: Scientific results of IGCP Project 288: Gondwanaland sutures and mobile belts: Episodes, v. 19, p. 11-20.

Weber, W.J., 1993, Alpha-decay-induced amorphization in complex silicate structures: Journal of the American Ceramic Society, v. 76, 1729-1738.

Weber, W.J., Ewing, R.C., Meldrum, A., 1997, The kinetics of alpha-decay-induced amorphization in zircon and apatite containing weapons grade plutonium or other actinides: Journal of Nuclear Materials, v. 250, p. 147-155.

Wilson, M., and Guiraud, R., 1998, Late Permian to Recent magmatic activity on the African-Arabian margin of Tethys, Petroleum Geology of North Africa: *in* Geological Society of London, Special Publication 132, p. 231-263.

Wolf, R.A., Farley, K.A., and Silver, L.T., 1996, Helium diffusion and low-temperature thermochronometry of apatite, Geochimica et Cosmochimica Acta, v. 60, p. 4231-4240.

Ziegler, P.A., 1989, Evolution of Laurussia: A study in Late Paleozoic plate tectonics: Kluwer Academic Publication, Dordrecht, 102 p.

LIST OF FIGURES AND TABLES

Table 1 – SOKAR-1X (U-Th)/He Data

Sample	Aliquots	MD [m]	Unit	Age [Ma]	± [Ma] 8%	U (ppm)	Th (ppm)	Th/U	eU	He (nmol/g)	mass (µg)	Ft	α-dose (200 Ma)
SKR00750	ZS0075-1 [2]	229	Moghra	24.6	2.0	105.5	50.3	0.48	117.4	11.06	3.0	0.71	7.77E+15
	ZS0075-2	229	Moghra	534.2	42.7	69.3	53.8	0.78	81.9	177.89	4.7	0.73	5.42E+15
	ZS0075-3	229	Moghra	430.8	34.5	99.8	34.7	0.35	108.0	193.55	4.9	0.75	7.14E+15
	ZS0075-4	229	Moghra	510.5	40.8	65.4	15.5	0.24	69.1	159.92	10.7	0.81	4.57E+15
	ZS0075-5 [2]	229	Moghra	194.2	15.5	143.0	58.1	0.41	156.6	123.73	3.5	0.74	1.04E+16
SKR00780	ZS0078-1	238	Moghra	506.9	40.6	154.7	48.0	0.31	166.0	372.85	7.1	0.79	1.10E+16
	ZS0078-2	238	Moghra	286.0	22.9	67.8	23.9	0.35	73.4	94.19	10.5	0.81	4.86E+15
	ZS0078-3	238	Moghra	504.8	40.4	92.4	42.0	0.45	102.3	222.81	6.2	0.77	6.77E+15
SKR01470	ZS0147-1 [2]	448	Moghra	276.8	22.1	237.4	48.5	0.20	248.8	277.22	3.3	0.73	1.65E+16
	ZS0147-2 [2]	448	Moghra	83.1	6.6	92.1	30.4	0.33	99.3	34.03	5.3	0.76	6.57E+15
	ZS0147-3 [2]	448	Moghra	251.0	20.1	246.2	58.8	0.24	260.0	254.82	2.5	0.71	1.72E+16
	ZS0147-4	448	Moghra	248.8	19.9	102.5	24.0	0.23	108.1	110.75	4.2	0.75	7.15E+15
	ZS0147-5	448	Moghra	342.3	27.4	149.8	54.6	0.36	162.6	234.28	4.8	0.76	1.08E+16
	ZS0147-6	448	Moghra	337.2	27.0	61.9	38.9	0.63	71.1	99.72	4.9	0.75	4.70E+15
	ZS0147-7 [2]	448	Moghra	36.6	2.9	38.3	47.9	1.25	49.6	6.96	3.1	0.71	3.28E+15
SKR01500	ZS0150-1	457	Moghra	293.7	23.5	45.4	17.5	0.38	49.5	58.44	3.6	0.73	3.28E+15
	ZS0150-2 [2]	457	Moghra	206.8	16.5	183.8	89.8	0.49	204.9	173.92	4.7	0.75	1.36E+16
	ZS0150-3 [2]	457	Moghra	89.7	7.2	142.0	30.3	0.21	149.1	54.36	4.4	0.75	9.87E+15
	ZS0150-4	457	Moghra	340.1	27.2	89.1	45.7	0.51	99.9	129.86	2.5	0.69	6.61E+15
	ZS0150-5 [2]	457	Moghra	145.3	11.6	226.2	174.9	0.77	267.3	148.49	2.7	0.70	1.77E+16
	ZS0150-6	457	Moghra	287.6	23.0	88.2	54.9	0.62	101.1	117.28	3.9	0.73	6.69E+15
	ZS0150-7	457	Moghra	587.9	47.0	31.5	15.3	0.49	35.1	79.61	3.3	0.69	2.32E+15
SKR01590	ZS0159-1	485	Moghra	490.6	39.3	95.1	28.1	0.30	101.7	186.74	2.6	0.67	6.73E+15
	ZS0159-2	485	Moghra	406.7	32.5	89.3	20.8	0.23	94.2	139.85	1.6	0.66	6.23E+15
	ZS0159-3	485	Moghra	407.7	32.6	151.8	46.1	0.30	162.6	239.03	1.5	0.65	1.08E+16
	ZS0159-4 [2]	485	Moghra	133.2	10.7	173.0	56.5	0.33	186.3	93.12	2.2	0.69	1.23E+16
SKR01629	ZS0162-1	494	Moghra	420.5	33.6	344.8	229.8	0.67	398.8	633.64	1.7	0.68	2.64E+16
	ZS0162-2	494	Moghra	409.7	32.8	105.6	33.7	0.32	113.5	167.91	1.5	0.65	7.51E+15
	ZS0162-3	494	Moghra	365.5	29.2	204.7	67.6	0.33	220.6	287.72	1.4	0.65	1.46E+16
SKR01650	ZS0165-1 [2]	503	Moghra	96.8	7.7	66.5	29.8	0.45	73.5	27.43	3.0	0.71	4.86E+15
	ZS0165-2	503	Moghra	282.9	22.6	57.2	30.2	0.53	64.3	71.29	3.0	0.71	4.26E+15
	ZS0165-3	503	Moghra	118.8	9.5	0.0	0.8	-28.30	0.2	0.07	3.3	0.70	9.99E+12
	ZS0165-4 [2]	503	Moghra	142.7	11.4	68.1	32.3	0.47	75.7	42.66	6.8	0.73	5.01E+15

[1]alpha-dose greater than 3.0E+16 events /mg. [2]He deficient determined by filter 2. [3]Excess He determined by filter 2. (excluded from cumulative probability density distributions)

Table 1 – SOKAR-1X (U-Th)/He Data (continued)

Sample	Aliquots	MD [m]	Unit	Age [Ma]	± [Ma] 8%	U (ppm)	Th (ppm)	Th/U	eU	He (nmol/g)	mass (µg)	Ft	α-dose (200 Ma)
SKR01650	ZS0165-5 [3]	503	Moghra	643.2	51.5	277.9	66.2	0.24	293.5	839.31	5.8	0.78	1.94E+16
	ZS0165-6	503	Moghra	286.3	22.9	40.3	15.7	0.39	44.0	46.46	1.8	0.67	2.91E+15
	ZS0165-7	503	Moghra	540.5	43.2	175.8	57.5	0.33	189.3	379.16	1.7	0.66	1.25E+16
SKR05660	ZS0566-1	1725	U. Bahariya	455.1	36.4	66.5	28.0	0.42	73.0	128.51	2.7	0.70	4.83E+15
	ZS0566-2	1725	U. Bahariya	532.8	42.6	105.4	50.0	0.47	117.2	242.36	2.9	0.70	7.75E+15
	ZS0566-3	1725	U. Bahariya	528.1	42.2	137.2	112.5	0.82	163.7	335.88	2.8	0.70	1.08E+16
	ZS0566-4	1725	U. Bahariya	435.3	34.8	320.3	177.4	0.55	362.0	594.40	1.9	0.68	2.40E+16
	ZS0566-5	1725	U. Bahariya	502.7	40.2	75.7	97.2	1.28	98.5	180.50	1.7	0.66	6.52E+15
	ZS0566-6	1725	U. Bahariya	393.9	31.5	158.9	56.8	0.36	172.3	263.28	2.5	0.70	1.14E+16
SKR05690	ZS0569-1	1734	U. Bahariya	489.9	39.2	160.2	96.3	0.60	182.8	359.59	2.8	0.72	1.21E+16
	ZS0569-2	1734	U. Bahariya	399.1	31.9	152.4	199.0	1.31	199.2	325.34	4.6	0.74	1.32E+16
	ZS0569-3	1734	U. Bahariya	404.5	32.4	141.1	83.1	0.59	160.6	269.31	4.7	0.75	1.06E+16
	ZS0569-4	1734	U. Bahariya	432.4	34.6	164.2	89.8	0.55	185.3	331.75	4.0	0.75	1.23E+16
	ZS0569-5 [2]	1734	U. Bahariya	266.9	21.4	178.6	90.9	0.51	200.0	215.41	3.8	0.74	1.32E+16
	ZS0569-6	1734	U. Bahariya	308.0	24.6	80.6	39.2	0.49	89.8	115.77	4.9	0.76	5.94E+15
SKR06070	ZS0607-4	1850	L. Bahariya	486.1	38.9	149.0	52.8	0.35	161.4	313.16	3.5	0.72	1.07E+16
	ZS0607-5 [2]	1850	L. Bahariya	235.3	18.8	179.5	58.8	0.33	193.3	172.12	2.5	0.69	1.28E+16
	ZS0607-6	1850	L. Bahariya	478.2	38.3	95.6	58.3	0.61	109.3	202.53	2.8	0.70	7.24E+15
	ZS0607-7 [2]	1850	L. Bahariya	168.4	13.5	129.6	15.8	0.12	133.3	87.51	2.8	0.72	8.82E+15
	ZS0607-8	1850	L. Bahariya	438.8	35.1	119.6	42.0	0.35	129.4	216.20	2.1	0.69	8.56E+15
	ZS0607-9	1850	L. Bahariya	486.8	38.9	61.4	106.5	1.73	86.4	158.41	2.3	0.68	5.72E+15
SKR06100	ZS0610-1	1859	L. Bahariya	424.8	34.0	87.6	29.0	0.33	94.4	160.30	2.9	0.72	6.25E+15
	ZS0610-2	1859	L. Bahariya	526.8	42.1	171.0	50.4	0.29	182.9	407.50	4.8	0.75	1.21E+16
	ZS0610-3	1859	L. Bahariya	414.0	33.1	50.7	24.7	0.49	56.5	95.16	3.8	0.73	3.74E+15
	ZS0610-4	1859	L. Bahariya	453.2	36.3	205.8	69.2	0.34	222.0	392.95	2.5	0.70	1.47E+16
	ZS0610-5	1859	L. Bahariya	530.8	42.5	67.7	29.7	0.44	74.7	159.75	2.9	0.72	4.94E+15
	ZS0610-6	1859	L. Bahariya	348.3	27.9	126.7	46.5	0.37	137.7	176.25	1.6	0.67	9.11E+15
SKR06310	ZS0631-4	1923	L. Bahariya	481.8	38.5	103.5	56.1	0.54	116.7	233.94	4.4	0.75	7.72E+15
	ZS0631-5	1923	L. Bahariya	453.0	36.2	75.6	36.1	0.48	84.0	149.84	3.1	0.71	5.56E+15
	ZS0631-6	1923	L. Bahariya	525.4	42.0	120.8	55.4	0.46	133.8	301.66	7.0	0.77	8.85E+15
	ZS0631-7	1923	L. Bahariya	537.9	43.0	50.1	103.8	2.07	74.5	166.42	4.9	0.75	4.93E+15
	ZS0631-8	1923	L. Bahariya	436.5	34.9	171.8	102.8	0.60	196.0	333.40	2.3	0.70	1.30E+16
	ZS0631-9 [2]	1923	L. Bahariya	237.3	19.0	175.5	80.3	0.46	194.4	183.29	3.4	0.73	1.29E+16

[1]alpha-dose greater than 3.0E+16 events /mg. [2]He deficient determined by filter 2. [3]Excess He determined by filter 2. (excluded from cumulative probability density distributions)

Table 1 – SOKAR-1X (U-Th)/He Data (continued)

Sample	Aliquots	MD [m]	Unit	Age [Ma]	± [Ma] 8%	U (ppm)	Th (ppm)	Th/U	eU	He (nmol/g)	mass (µg)	Ft	α-dose (200 Ma)
SKR06340	ZS0634-1	1932	L. Bahariya	378.2	30.3	259.6	69.0	0.27	275.8	418.63	3.3	0.73	1.82E+16
	ZS0634-2	1932	L. Bahariya	490.5	39.2	219.7	139.1	0.63	252.4	497.35	3.3	0.72	1.67E+16
	ZS0634-3	1932	L. Bahariya	483.4	38.7	62.7	16.5	0.26	66.6	129.35	3.1	0.72	4.41E+15
	ZS0634-4	1932	L. Bahariya	416.3	33.3	90.0	33.7	0.37	97.9	171.03	3.9	0.76	6.48E+15
	ZS0634-5	1932	L. Bahariya	431.6	34.5	154.1	85.1	0.55	174.1	303.34	3.6	0.73	1.15E+16
	ZS0634-6	1932	L. Bahariya	491.8	39.3	88.6	42.8	0.48	98.7	199.49	3.9	0.74	6.53E+15
SKR06430	ZS0643-4	1960	Kharita	484.8	38.8	151.1	75.6	0.50	168.9	338.56	5.0	0.74	1.12E+16
	ZS0643-5	1960	Kharita	441.3	35.3	144.1	75.6	0.52	161.9	298.12	5.1	0.75	1.07E+16
	ZS0643-6	1960	Kharita	453.9	36.3	339.7	170.1	0.50	379.7	727.40	4.9	0.76	2.51E+16
SKR06460	ZS0646-2	1969	Kharita	386.6	30.9	84.2	38.3	0.46	93.2	148.87	4.4	0.75	6.16E+15
	ZS0646-3	1969	Kharita	521.9	41.7	223.4	98.1	0.44	246.5	542.70	5.4	0.75	1.63E+16
	ZS0646-4	1969	Kharita	550.3	44.0	110.5	49.4	0.45	122.1	282.20	5.0	0.75	8.08E+15
	ZS0646-5	1969	Kharita	486.0	38.9	45.0	16.8	0.37	48.9	102.79	8.3	0.77	3.24E+15
SKR06800	ZS0680-1	2073	Kharita	536.2	42.9	214.4	100.3	0.47	238.0	576.06	9.2	0.80	1.57E+16
	ZS0680-2 [3]	2073	Kharita	576.6	46.1	208.8	61.3	0.29	223.2	594.57	10.8	0.82	1.48E+16
	ZS0680-3	2073	Kharita	541.7	43.3	51.6	30.4	0.59	58.8	142.83	8.7	0.80	3.89E+15
	ZS0680-4	2073	Kharita	409.5	32.8	132.4	135.8	1.03	164.3	294.12	7.8	0.79	1.09E+16
	ZS0680-5	2073	Kharita	441.5	35.3	30.3	38.6	1.27	39.4	74.44	6.9	0.77	2.61E+15
	ZS0680-6	2073	Kharita	411.3	32.9	117.0	26.7	0.23	123.3	230.64	11.4	0.82	8.15E+15
SKR06830	ZS0683-1	2082	Kharita	413.5	33.1	201.3	121.9	0.61	230.0	412.67	7.6	0.78	1.52E+16
	ZS0683-2	2082	Kharita	441.7	35.3	110.5	63.5	0.57	125.4	247.89	12.1	0.80	8.30E+15
	ZS0683-3	2082	Kharita	462.0	37.0	209.8	72.5	0.35	226.9	454.87	6.6	0.78	1.50E+16
	ZS0683-4 [3]	2082	Kharita	712.4	57.0	109.9	41.9	0.38	119.7	373.37	5.8	0.77	7.92E+15
SKR07400	ZS0740-4	2256	Kharita	476.5	38.1	36.6	24.1	0.66	42.3	85.80	5.9	0.76	2.80E+15
	ZS0740-5	2256	Kharita	330.4	26.4	131.1	27.8	0.21	137.7	196.88	8.3	0.78	9.11E+15
	ZS0740-6 [3]	2256	Kharita	1165.0	93.2	99.8	69.3	0.69	116.1	609.97	5.7	0.76	7.68E+15
SKR07430	ZS0743-1	2265	Kharita	488.4	39.1	83.5	41.0	0.49	93.1	180.28	2.8	0.71	6.16E+15
	ZS0743-2 [2]	2265	Kharita	159.4	12.7	230.9	110.4	0.48	256.8	165.67	3.5	0.74	1.70E+16
	ZS0743-3	2265	Kharita	117.5	9.4	42.0	43.7	1.04	52.3	24.19	3.2	0.72	3.46E+15
SKR07950	ZS0795-1	2423	Kharita	292.8	23.4	133.2	42.2	0.32	143.1	174.60	4.4	0.76	9.47E+15
	ZS0795-2	2423	Kharita	471.1	37.7	151.6	101.6	0.67	175.5	338.60	3.9	0.74	1.16E+16
	ZS0795-3	2423	Kharita	493.2	39.5	61.4	52.3	0.85	73.7	149.22	3.8	0.74	4.88E+15
	ZS0795-4	2423	Kharita	445.1	35.6	282.9	124.1	0.44	312.1	607.46	6.5	0.78	2.07E+16

[1]alpha-dose greater than 3.0E+16 events /mg. [2]He deficient determined by filter 2. [3]Excess He determined by filter 2. (excluded from cumulative probability density distributions)

Table 1 – SOKAR-1X (U-Th)/He Data (continued)

Sample	Aliquots	MD [m]	Unit	Age [Ma]	± [Ma] 8%	U (ppm)	Th (ppm)	Th/U	eU	He (nmol/g)	mass (µg)	Ft	α-dose (200 Ma)
SKR07950	ZS0795-5	2423	Kharita	352.6	28.2	134.7	48.5	0.36	146.1	219.42	5.5	0.77	9.67E+15
SKR07980	ZS0798-1	2432	Kharita	448.5	35.9	53.5	29.6	0.55	60.4	118.44	6.6	0.78	4.00E+15
	ZS0798-2	2432	Kharita	482.7	38.6	137.1	98.2	0.72	160.2	338.16	6.8	0.78	1.06E+16
	ZS0798-3	2432	Kharita	400.2	32.0	134.2	66.6	0.50	149.8	249.94	5.0	0.75	9.92E+15
SKR08150	ZS0815-4 [3]	2484	Kharita	698.3	55.9	124.4	50.6	0.41	136.2	411.97	7.1	0.76	9.01E+15
	ZS0815-5 [3]	2484	Kharita	656.7	52.5	113.5	41.6	0.37	123.3	350.23	6.3	0.76	8.16E+15
	ZS0815-6	2484	Kharita	433.9	34.7	62.8	31.5	0.50	70.2	127.21	6.0	0.75	4.65E+15
SKR08180	ZS0818-1	2493	Kharita	342.9	27.4	141.3	45.6	0.32	152.0	217.65	4.1	0.76	1.01E+16
	ZS0818-2 [2]	2493	Kharita	117.8	9.4	87.4	80.4	0.92	106.3	49.91	3.6	0.73	7.04E+15
	ZS0818-3 [2]	2493	Kharita	332.6	26.6	323.7	59.4	0.18	337.6	472.26	5.3	0.76	2.23E+16
SKR09080	ZS0908-1	2768	Alamein A	481.4	38.5	169.7	61.8	0.36	184.3	349.54	2.4	0.71	1.22E+16
	ZS0908-2	2768	Alamein A	521.5	41.7	138.2	54.2	0.39	150.9	317.34	3.3	0.72	9.98E+15
	ZS0908-3	2768	Alamein A	466.4	37.3	112.7	45.8	0.41	123.5	219.50	2.2	0.69	8.17E+15
SKR09500	ZS0950-2	2896	Alam El Buib 2	485.9	38.9	79.4	26.1	0.33	85.6	183.54	7.0	0.79	5.66E+15
	ZS0950-4	2896	Alam El Buib 2	364.5	29.2	154.2	62.4	0.40	168.9	240.18	2.5	0.71	1.12E+16
	ZS0950-6	2896	Alam El Buib 2	415.6	33.3	307.7	71.8	0.23	324.6	557.97	3.5	0.74	2.15E+16
	ZS0950-7	2896	Alam El Buib 2	435.7	34.9	293.1	175.1	0.60	334.3	570.94	2.4	0.71	2.21E+16
	ZS0950-8	2896	Alam El Buib 2	451.3	36.1	120.3	72.6	0.60	137.3	269.24	6.3	0.78	9.09E+15
SKR09530	ZS0953-4	2905	Alam El Buib 2	432.0	34.6	165.2	93.9	0.57	187.3	345.86	6.5	0.77	1.24E+16
	ZS0953-5 [3]	2905	Alam El Buib 2	680.8	54.5	265.3	164.6	0.62	304.0	857.31	3.9	0.73	2.01E+16
	ZS0953-6	2905	Alam El Buib 2	464.9	37.2	208.7	53.3	0.26	221.3	427.27	4.4	0.75	1.46E+16
SKR10130	ZS1013-4	3088	Alam El Buib 2	527.4	42.2	59.7	69.4	1.16	76.0	155.99	3.2	0.70	5.03E+15
	ZS1013-5	3088	Alam El Buib 2	403.6	32.3	83.0	73.3	0.88	100.2	161.17	3.8	0.72	6.63E+15
	ZS1013-6	3088	Alam El Buib 2	412.6	33.0	190.8	115.7	0.61	218.0	354.95	2.9	0.71	1.44E+16
SKR10160	ZS1016-4	3097	Alam El Buib 2	515.4	41.2	22.9	35.5	1.55	31.2	67.67	4.6	0.75	2.07E+15
	ZS1016-5 [3]	3097	Alam El Buib 2	665.9	53.3	294.6	142.4	0.48	328.0	924.06	3.7	0.75	2.17E+16
	ZS1016-6 [3]	3097	Alam El Buib 2	644.9	51.6	148.3	141.5	0.95	181.5	495.24	4.9	0.75	1.20E+16
SKR10620	ZS1062-4	3237	Alam El Buib 2	496.9	39.8	178.4	105.3	0.59	203.2	406.78	3.5	0.72	1.34E+16
	ZS1062-5	3237	Alam El Buib 2	402.4	32.2	209.6	180.4	0.86	251.9	402.14	3.3	0.72	1.67E+16
	ZS1062-6	3237	Alam El Buib 2	388.5	31.1	312.0	177.0	0.57	353.6	549.66	4.1	0.72	2.34E+16
SKR10650	ZS1065-4	3246	Alam El Buib 2	552.6	44.2	103.3	39.5	0.38	112.6	260.61	4.2	0.75	7.45E+15
	ZS1065-5 [3]	3246	Alam El Buib 2	655.4	52.4	121.7	52.0	0.43	133.9	376.50	4.3	0.76	8.86E+15
	ZS1065-6	3246	Alam El Buib 2	443.4	35.5	378.7	173.4	0.46	419.4	781.88	4.1	0.76	2.78E+16

[1]alpha-dose greater than 3.0E+16 events /mg. [2]He deficient determined by filter 2. [3]Excess He determined by filter 2. (excluded from cumulative probability density distributions)

Table 1 – SOKAR-1X (U-Th)/He Data (continued)

Sample	Aliquots	MD [m]	Unit	Age [Ma]	± [Ma] 8%	U (ppm)	Th (ppm)	Th/U	eU	He (nmol/g)	mass (µg)	Ft	α-dose (200 Ma)
SKR10950	ZS1095-4	3338	Alam El Buib 3C	364.0	29.1	115.1	141.0	1.23	148.2	208.79	3.0	0.70	9.81E+15
	ZS1095-5 [3]	3338	Alam El Buib 3C	748.7	59.9	90.3	119.8	1.33	118.5	347.53	2.5	0.69	7.84E+15
	ZS1095-6 [3]	3338	Alam El Buib 3C	717.5	57.4	148.5	52.1	0.35	160.8	458.22	2.5	0.70	1.06E+16
SKR10980	ZS1098-1	3347	Alam El Buib 3C	342.9	27.4	57.4	75.1	1.31	75.1	105.79	4.3	0.75	4.97E+15
	ZS1098-2 [2]	3347	Alam El Buib 3C	298.0	23.8	155.2	74.5	0.48	172.7	210.09	4.0	0.74	1.14E+16
	ZS1098-3	3347	Alam El Buib 3C	415.2	33.2	93.1	52.2	0.56	105.4	185.57	5.7	0.76	6.97E+15
	ZS1098-4	3347	Alam El Buib 3C	443.5	35.5	163.6	62.7	0.38	178.3	332.47	4.6	0.76	1.18E+16
	ZS1098-5	3347	Alam El Buib 3C	373.2	29.9	52.2	60.5	1.16	66.4	104.25	4.9	0.76	4.40E+15
	ZS1098-6	3347	Alam El Buib 3C	277.1	22.2	131.1	37.4	0.29	139.9	152.83	2.8	0.72	9.26E+15
SKR11480	ZS1148-4	3499	Alam El Buib 3C	484.2	38.7	100.7	81.1	0.81	119.7	246.62	6.0	0.76	7.93E+15
	ZS1148-5	3499	Alam El Buib 3C	484.7	38.8	293.7	24.4	0.08	299.5	634.53	7.0	0.78	1.98E+16
	ZS1148-6	3499	Alam El Buib 3C	547.2	43.8	104.3	50.9	0.49	116.2	269.58	5.5	0.76	7.69E+15
SKR11870	ZS1187-1	3618	Alam El Buib 3C	404.3	32.3	117.8	56.2	0.48	131.0	207.80	3.4	0.71	8.67E+15
	ZS1187-2	3618	Alam El Buib 3C	405.2	32.4	135.2	43.8	0.32	145.5	236.74	3.4	0.72	9.63E+15
	ZS1187-3	3618	Alam El Buib 3C	395.6	31.6	186.0	42.9	0.23	196.0	304.28	2.8	0.71	1.30E+16
SKR11900	ZS1190-1	3627	Alam El Buib 3C	424.5	34.0	165.9	51.4	0.31	178.0	288.55	2.2	0.69	1.18E+16
	ZS1190-2 [2]	3627	Alam El Buib 3C	179.6	14.4	75.1	72.8	0.97	92.2	64.79	3.4	0.72	6.11E+15
	ZS1190-3	3627	Alam El Buib 3C	485.6	38.9	62.3	83.0	1.33	81.8	159.10	3.1	0.72	5.42E+15
	ZS1190-4	3627	Alam El Buib 3C	344.0	27.5	65.5	23.1	0.35	71.0	100.28	3.9	0.74	4.70E+15
	ZS1190-5	3627	Alam El Buib 3C	462.4	37.0	156.8	113.0	0.72	183.4	346.70	3.9	0.74	1.21E+16
	ZS1190-6	3627	Alam El Buib 3C	441.4	35.3	110.1	52.9	0.48	122.5	216.58	3.3	0.72	8.11E+15
SKR12330	ZS1233-4	3758	Alam El Buib 3C	535.3	42.8	177.5	94.6	0.53	199.7	458.27	5.8	0.76	1.32E+16
	ZS1233-5 [2]	3758	Alam El Buib 3C	208.3	16.7	354.9	162.3	0.46	393.0	343.75	5.9	0.77	2.60E+16
	ZS1233-6	3758	Alam El Buib 3C	568.6	45.5	208.4	120.0	0.58	236.6	547.87	3.1	0.73	1.57E+16
	ZS1233-7 [3]	3758	Alam El Buib 3C	928.3	74.3	177.3	179.3	1.01	219.5	873.30	4.0	0.74	1.45E+16
	ZS1233-8	3758	Alam El Buib 3C	355.1	28.4	145.1	90.9	0.63	166.5	246.52	4.3	0.75	1.10E+16
SKR12360	ZS1236-1	3767	Alam El Buib 3C	456.7	36.5	197.3	141.5	0.72	230.6	443.07	6.7	0.76	1.53E+16
	ZS1236-2	3767	Alam El Buib 3C	599.6	48.0	29.0	24.6	0.85	34.8	89.84	6.4	0.76	2.31E+15
	ZS1236-3	3767	Alam El Buib 3C	527.9	42.2	201.6	88.3	0.44	222.3	497.02	5.7	0.76	1.47E+16
SKR12600	ZS1260-4 [2]	3840	Alam El Buib 3D	352.7	28.2	324.3	174.7	0.54	365.3	535.08	5.6	0.75	2.42E+16
	ZS1260-5 [2]	3840	Alam El Buib 3D	207.5	16.6	441.3	40.1	0.09	450.7	389.90	6.5	0.76	2.98E+16
	ZS1260-6	3840	Alam El Buib 3D	361.7	28.9	187.3	240.9	1.29	244.0	359.93	5.5	0.74	1.62E+16
SKR12630	ZS1263-1	3850	Alam El Buib 3D	196.0	15.7	52.5	40.5	0.77	62.0	50.48	6.1	0.76	4.10E+15

[1]alpha-dose greater than 3.0E+16 events /mg. [2]He deficient determined by filter 2. [3]Excess He determined by filter 2. (excluded from cumulative probability density distributions)

Table 1 – SOKAR-1X (U-Th)/He Data (continued)

Sample	Aliquots	MD [m]	Unit	Age [Ma]	± [Ma] 8%	U (ppm)	Th (ppm)	Th/U	eU	He (nmol/g)	mass (µg)	Ft	α-dose (200 Ma)
SKR12630	ZS1263-2	3850	Alam El Buib 3D	427.6	34.2	113.4	78.2	0.69	131.8	232.21	4.6	0.74	8.72E+15
	ZS1263-3	3850	Alam El Buib 3D	302.0	24.2	63.8	21.7	0.34	68.9	87.88	5.4	0.77	4.56E+15
SKR12800	ZS1280-4	3901	Alam El Buib 3E	513.3	41.1	192.1	123.1	0.64	221.0	463.59	4.5	0.73	1.46E+16
	ZS1280-5	3901	Alam El Buib 3E	362.2	29.0	65.3	69.6	1.07	81.7	123.28	5.1	0.75	5.41E+15
	ZS1280-6 [1] [2]	3901	Alam El Buib 3E	169.8	13.6	599.1	58.6	0.10	612.8	434.48	4.4	0.77	4.05E+16
	ZS1280-7	3901	Alam El Buib 3E	349.8	28.0	186.0	85.7	0.46	206.1	293.70	3.9	0.74	1.36E+16
	ZS1280-8	3901	Alam El Buib 3E	436.9	35.0	170.7	229.8	1.35	224.7	387.09	2.7	0.71	1.49E+16
SKR12830	ZS1283-1 [2]	3911	Alam El Buib 3G	176.5	14.1	210.8	110.3	0.52	236.7	184.57	10.2	0.81	1.57E+16
	ZS1283-2	3911	Alam El Buib 3G	413.6	33.1	96.1	91.5	0.95	117.6	211.65	8.2	0.78	7.78E+15
	ZS1283-3 [2]	3911	Alam El Buib 3G	67.2	5.4	73.4	65.4	0.89	88.8	25.76	9.6	0.80	5.88E+15
	ZS1283-4	3911	Alam El Buib 3G	430.1	34.4	217.6	169.6	0.78	257.4	453.74	4.3	0.74	1.70E+16
	ZS1283-5	3911	Alam El Buib 3G	361.5	28.9	221.9	215.6	0.97	272.6	378.87	2.7	0.70	1.80E+16
	ZS1283-6	3911	Alam El Buib 3G	355.9	28.5	91.4	102.4	1.12	115.4	157.28	2.6	0.70	7.64E+15
	ZS1283-7	3911	Alam El Buib 3G	383.2	30.7	161.5	119.3	0.74	189.6	275.00	2.2	0.69	1.25E+16
	ZS1283-8	3911	Alam El Buib 3G	451.0	36.1	158.1	140.1	0.89	191.1	324.71	2.1	0.68	1.26E+16
	ZS1283-9 [2]	3911	Alam El Buib 3G	287.0	23.0	171.3	245.4	1.43	228.9	252.26	2.8	0.70	1.52E+16
SKR12940	ZS1294-1	3944	Alam El Buib 3G	342.8	27.4	110.4	28.8	0.26	117.2	182.98	13.4	0.82	7.75E+15
	ZS1294-2	3944	Alam El Buib 3G	252.4	20.2	71.8	30.8	0.43	79.0	86.82	8.3	0.79	5.23E+15
	ZS1294-3	3944	Alam El Buib 3G	420.4	33.6	66.3	50.8	0.77	78.2	150.68	13.9	0.82	5.18E+15
	ZS1294-4	3944	Alam El Buib 3G	431.6	34.5	117.5	61.0	0.52	131.8	236.41	4.7	0.75	8.72E+15
	ZS1294-5 [2]	3944	Alam El Buib 3G	161.4	12.9	182.2	183.8	1.01	225.4	143.53	2.8	0.72	1.49E+16
	ZS1294-6	3944	Alam El Buib 3G	455.1	36.4	166.8	92.3	0.55	188.5	352.65	3.5	0.74	1.25E+16
SKR12970	ZS1297-1	3953	Alam El Buib 3G	523.9	41.9	201.0	135.6	0.67	232.9	526.85	6.2	0.77	1.54E+16
	ZS1297-2	3953	Alam El Buib 3G	446.4	35.7	109.7	123.8	1.13	138.8	259.93	5.3	0.76	9.19E+15
	ZS1297-3	3953	Alam El Buib 3G	362.0	29.0	264.5	220.3	0.83	316.3	471.46	4.8	0.75	2.09E+16
	ZS1297-4	3953	Alam El Buib 3G	370.4	29.6	201.1	164.9	0.82	239.9	349.14	3.1	0.71	1.59E+16
	ZS1297-5 [2]	3953	Alam El Buib 3G	290.9	23.3	158.0	124.6	0.79	187.2	204.27	2.2	0.68	1.24E+16
	ZS1297-6	3953	Alam El Buib 3G	370.1	29.6	100.0	79.0	0.79	118.5	161.88	1.9	0.67	7.85E+15
SKR13250	ZS1325-4	4039	Paleozoic Und.	220.7	17.7	81.4	40.0	0.49	90.8	76.61	2.4	0.70	6.01E+15
	ZS1325-5	4039	Paleozoic Und.	410.8	32.9	259.7	192.4	0.74	304.9	487.85	2.5	0.70	2.02E+16
	ZS1325-6	4039	Paleozoic Und.	1331.9	106.6	76.5	93.0	1.21	98.4	574.71	3.8	0.73	6.51E+15
	ZS1325-7	4039	Paleozoic Und.	429.6	34.4	152.1	72.6	0.48	169.1	303.87	4.7	0.75	1.12E+16
	ZS1325-8 [1]	4039	Paleozoic Und.	129.0	10.3	746.2	186.0	0.25	789.9	420.33	5.0	0.76	5.23E+16

[1]alpha-dose greater than 3.0E+16 events /mg. [2]He deficient determined by filter 2. [3]Excess He determined by filter 2. (excluded from cumulative probability density distributions)

Table 1 – SOKAR-1X (U-Th)/He Data (continued)

Sample	Aliquots	MD [m]	Unit	Age [Ma]	± [Ma] 8%	U (ppm)	Th (ppm)	Th/U	eU	He (nmol/g)	mass (µg)	Ft	α-dose (200 Ma)
SKR13480	ZS1348-1	4109	Paleozoic Und.	205.1	16.4	32.6	58.5	1.80	46.3	43.80	21.2	0.84	3.07E+15
	ZS1348-2	4109	Paleozoic Und.	300.7	24.1	35.0	61.1	1.74	49.4	66.21	12.3	0.81	3.27E+15
	ZS1348-3	4109	Paleozoic Und.	410.5	32.8	68.4	83.2	1.22	87.9	159.53	8.9	0.80	5.82E+15
	ZS1348-4 [1]	4109	Paleozoic Und.	278.3	22.3	423.7	387.1	0.91	514.7	560.75	2.8	0.71	3.41E+16
	ZS1348-5	4109	Paleozoic Und.	418.3	33.5	213.9	210.4	0.98	263.3	445.43	3.2	0.73	1.74E+16
	ZS1348-6	4109	Paleozoic Und.	398.2	31.9	146.4	69.2	0.47	162.7	265.88	4.2	0.74	1.08E+16
SKR13510	ZS1351-1	4118	Paleozoic Und.	315.8	25.3	266.5	160.1	0.60	304.2	399.00	3.9	0.75	2.01E+16
	ZS1351-2	4118	Paleozoic Und.	355.8	28.5	335.1	221.0	0.66	387.0	569.63	4.4	0.75	2.56E+16
	ZS1351-3 [1]	4118	Paleozoic Und.	266.4	21.3	406.9	341.4	0.84	487.1	527.19	4.0	0.74	3.22E+16
SKR13700	ZS1370-1 [1]	4176	Paleozoic Und.	320.8	25.7	493.1	529.3	1.07	617.5	796.31	3.9	0.73	4.09E+16
	ZS1370-2	4176	Paleozoic Und.	273.9	21.9	146.4	75.4	0.51	164.1	183.81	4.4	0.74	1.09E+16
	ZS1370-3	4176	Paleozoic Und.	336.3	26.9	133.8	131.7	0.98	164.7	222.34	4.8	0.73	1.09E+16
SKR13730	ZS1373-1	4185	Paleozoic Und.	326.9	26.1	122.4	112.3	0.92	148.8	210.10	9.5	0.78	9.85E+15
	ZS1373-2	4185	Paleozoic Und.	277.5	22.2	98.4	88.8	0.90	119.3	142.98	9.9	0.79	7.90E+15
	ZS1373-3	4185	Paleozoic Und.	343.3	27.5	234.2	70.8	0.30	250.9	383.43	10.0	0.80	1.66E+16
SKR13800	ZS1380-1 [1]	4206	Paleozoic Und.	202.1	16.2	478.1	420.7	0.88	577.0	476.77	4.3	0.75	3.82E+16
	ZS1380-2	4206	Paleozoic Und.	392.8	31.4	144.9	67.8	0.47	160.8	267.46	5.2	0.76	1.06E+16
	ZS1380-3	4206	Paleozoic Und.	392.0	31.4	169.8	126.7	0.75	199.6	321.98	4.0	0.74	1.32E+16
SKR13830	ZS1383-4	4215	Paleozoic Und.	396.5	31.7	334.0	294.5	0.88	403.2	666.26	5.3	0.75	2.67E+16
	ZS1383-5	4215	Paleozoic Und.	224.4	18.0	111.0	164.5	1.48	149.7	131.50	3.5	0.72	9.91E+15
	ZS1383-6	4215	Paleozoic Und.	283.4	22.7	111.7	124.1	1.11	140.8	163.24	4.7	0.74	9.32E+15
SKR14250	ZS1425-1	4343	Paleozoic Und.	269.0	21.5	173.6	61.7	0.36	188.1	201.32	3.6	0.73	1.24E+16
	ZS1425-2	4343	Paleozoic Und.	1253.0	100.2	154.6	52.1	0.34	166.8	920.85	3.6	0.73	1.10E+16
	ZS1425-3	4343	Paleozoic Und.	289.0	23.1	88.8	111.1	1.25	114.9	131.45	3.2	0.72	7.61E+15
SKR14280	ZS1428-2	4353	Paleozoic Und.	406.8	32.5	199.9	151.6	0.76	235.6	367.82	2.5	0.69	1.56E+16
	ZS1428-3	4353	Paleozoic Und.	346.9	27.8	280.0	210.0	0.75	329.4	451.66	3.2	0.72	2.18E+16
SKR14900	ZS1490-1 [1]	4542	Paleozoic Und.	73.7	5.9	577.9	270.5	0.47	641.5	189.50	4.0	0.74	4.24E+16
	ZS1490-2	4542	Paleozoic Und.	160.5	12.8	329.6	61.9	0.19	344.2	232.10	5.4	0.77	2.28E+16
	ZS1490-3 [1]	4542	Paleozoic Und.	161.7	12.9	562.4	167.7	0.30	601.8	426.00	9.4	0.80	3.98E+16
SKR14930	ZS1493-1	4551	Paleozoic Und.	433.4	34.7	69.9	78.6	1.12	88.4	156.29	4.2	0.74	5.85E+15
	ZS1493-2	4551	Paleozoic Und.	381.8	30.5	178.1	217.9	1.22	229.3	363.21	5.5	0.75	1.52E+16
	ZS1493-3	4551	Paleozoic Und.	382.4	30.6	111.5	124.5	1.12	140.7	222.85	5.2	0.75	9.32E+15
SKR15250	ZS1525-4	4648	Paleozoic Und.	148.9	11.9	170.3	57.9	0.34	184.0	120.37	14.5	0.81	1.22E+16

[1]alpha-dose greater than 3.0E+16 events /mg. [2]He deficient determined by filter 2. [3]Excess He determined by filter 2. (excluded from cumulative probability density distributions)

Table 1 – SOKAR-1X (U-Th)/He Data (continued)

Sample	Aliquots	MD [m]	Unit	Age [Ma]	± [Ma] 8%	U (ppm)	Th (ppm)	Th/U	eU	He (nmol/g)	mass (µg)	Ft	α-dose (200 Ma)
SKR15250	ZS1525-5	4648	Paleozoic Und.	338.7	27.1	268.6	183.3	0.68	311.6	453.37	7.2	0.78	2.06E+16
	ZS1525-6	4648	Paleozoic Und.	335.5	26.8	172.7	53.7	0.31	185.3	269.01	5.9	0.78	1.23E+16
	ZS1525-7	4648	Paleozoic Und.	246.0	19.7	200.7	152.6	0.76	236.6	221.80	2.5	0.70	1.57E+16
	ZS1525-8	4648	Paleozoic Und.	284.9	22.8	178.2	260.1	1.46	239.4	262.03	2.8	0.70	1.59E+16
SKR15280	ZS1528-1	4657	Paleozoic Und.	500.7	40.1	200.8	245.2	1.22	258.4	558.99	5.8	0.77	1.71E+16
	ZS1528-2	4657	Paleozoic Und.	159.5	12.8	175.4	55.9	0.32	188.6	121.06	4.1	0.74	1.25E+16
	ZS1528-3 [1]	4657	Paleozoic Und.	36.1	2.9	2056.8	233.4	0.11	2111.6	315.32	5.4	0.77	1.40E+17
	ZS1528-4	4657	Paleozoic Und.	374.7	30.0	269.1	107.7	0.40	294.4	451.47	3.4	0.74	1.95E+16
	ZS1528-5 [1]	4657	Paleozoic Und.	206.6	16.5	524.7	233.6	0.45	579.6	493.46	4.9	0.75	3.84E+16
	ZS1528-6 [1]	4657	Paleozoic Und.	251.8	20.1	539.4	160.4	0.30	577.0	608.04	4.8	0.76	3.82E+16
SKR15350	ZS1535-1	4679	Paleozoic Und.	408.2	32.7	87.8	123.4	1.41	116.8	213.27	10.7	0.81	7.74E+15
	ZS1535-2	4679	Paleozoic Und.	283.5	22.7	196.1	133.0	0.68	227.4	282.96	8.9	0.80	1.50E+16
	ZS1535-3	4679	Paleozoic Und.	413.3	33.1	201.3	106.2	0.53	226.3	416.79	9.3	0.80	1.50E+16
SKR15380	ZS1538-1	4688	Paleozoic Und.	346.6	27.7	237.1	90.3	0.38	258.4	367.39	4.4	0.74	1.71E+16
	ZS1538-2	4688	Paleozoic Und.	354.8	28.4	340.3	271.2	0.80	404.0	606.46	6.3	0.77	2.67E+16
	ZS1538-3	4688	Paleozoic Und.	463.0	37.0	103.5	46.7	0.45	114.5	221.46	4.3	0.75	7.58E+15

[1]alpha-dose greater than 3.0E+16 events /mg. [2]He deficient determined by filter 2. [3]Excess He determined by filter 2. (excluded from cumulative probability density distributions)

Table 2 – HEQET-2 (U-Th)/He Data

Sample	Aliquots	MD [m]	Unit	Age [Ma]	± [Ma] 8%	U (ppm)	Th (ppm)	Th/U	eU	He (nmol/g)	mass (µg)	Ft	α-dose (200 Ma)
HQT14460	ZH1446-1	4407	Jurassic	315.4	25.2	109.6	66.0	0.60	125.1	168.71	7.0	0.78	8.28E+15
HQT14460	ZH1446-2	4407	Jurassic	390.8	31.3	125.8	123.8	0.98	154.9	252.33	4.4	0.75	1.03E+16
HQT14460	ZH1446-3	4407	Jurassic	354.5	28.4	202.5	52.2	0.26	214.7	313.11	3.8	0.74	1.42E+16
HQT14490	ZH1449-1	4417	Jurassic	208.0	16.6	43.2	30.2	0.70	50.3	43.41	5.8	0.76	3.33E+15
HQT14490	ZH1449-2	4417	Jurassic	487.1	39.0	111.9	119.7	1.07	140.1	281.27	4.6	0.74	9.27E+15
HQT14490	ZH1449-3	4417	Jurassic	182.4	14.6	25.2	24.0	0.95	30.8	23.31	6.7	0.76	2.04E+15
HQT14490	ZH1449-4	4417	Jurassic	393.0	31.4	54.0	50.0	0.93	65.7	103.83	5.1	0.73	4.35E+15
HQT14520	ZH1452-1	4426	Jurassic	364.6	29.2	140.3	67.8	0.48	156.2	214.22	2.1	0.68	1.03E+16
HQT14520	ZH1452-2 [1]	4426	Jurassic	62.7	5.0	489.0	182.0	0.37	531.7	120.48	1.9	0.67	3.52E+16
HQT14520	ZH1452-3	4426	Jurassic	316.1	25.3	251.8	221.5	0.88	303.8	358.31	2.1	0.68	2.01E+16
HQT14550	ZH1455-1	4435	Jurassic	226.3	18.1	213.7	43.3	0.20	223.9	206.61	4.1	0.75	1.48E+16
HQT14550	ZH1455-2	4435	Jurassic	296.2	23.7	141.0	99.9	0.71	164.5	196.40	3.9	0.73	1.09E+16
HQT14550	ZH1455-3	4435	Jurassic	265.5	21.2	232.2	95.3	0.41	254.6	266.96	2.5	0.72	1.68E+16
HQT14580	ZH1458-1	4444	Jurassic	302.0	24.2	42.3	58.7	1.39	56.0	69.50	5.0	0.75	3.71E+15
HQT14580	ZH1458-2	4444	Jurassic	313.5	25.1	308.2	214.3	0.70	358.6	482.56	7.2	0.78	2.37E+16
HQT14580	ZH1458-3	4444	Jurassic	262.4	21.0	345.1	41.4	0.12	354.8	395.45	5.9	0.77	2.35E+16
HQT14630	ZH1463-1	4459	Jurassic	176.6	14.1	124.6	22.6	0.18	129.9	92.60	3.9	0.74	8.59E+15
HQT14630	ZH1463-2	4459	Jurassic	203.4	16.3	229.3	73.2	0.32	246.5	210.71	5.8	0.77	1.63E+16
HQT14630	ZH1463-3	4459	Jurassic	328.1	26.2	37.1	23.1	0.62	42.6	57.57	4.6	0.75	2.82E+15
HQT14630	ZH1463-4	4459	Jurassic	392.7	31.4	124.2	55.7	0.45	137.3	220.80	4.1	0.74	9.09E+15
HQT14690	ZH1469-1	4478	Jurassic	352.7	28.2	265.7	67.5	0.25	281.6	392.24	2.5	0.72	1.86E+16
HQT14690	ZH1469-2	4478	Jurassic	253.3	20.3	83.8	120.0	1.43	112.0	98.43	1.5	0.63	7.42E+15
HQT14690	ZH1469-3	4478	Jurassic	279.5	22.4	252.1	111.8	0.44	278.4	297.21	2.8	0.70	1.84E+16
HQT14700	ZH1470-1	4481	Jurassic	332.2	26.6	90.7	58.1	0.64	104.3	138.09	2.9	0.72	6.90E+15
HQT14700	ZH1470-2	4481	Jurassic	372.2	29.8	104.3	49.7	0.48	116.0	174.33	3.9	0.73	7.67E+15
HQT14700	ZH1470-3	4481	Jurassic	340.5	27.2	252.0	49.5	0.20	263.7	362.17	3.0	0.73	1.74E+16
HQT14700	ZH1470-4 [1]	4481	Jurassic	192.9	15.4	427.0	323.2	0.76	503.0	397.25	4.4	0.75	3.33E+16

[1]alpha-dose greater than 3.0E+16 events /mg. [2]He deficient determined by filter 2. [3]Excess He determined by filter 2. (excluded from cumulative probability density distributions)

Figure 1. Tectonic map of northeastern Africa (after Bosworth et al., 2008).

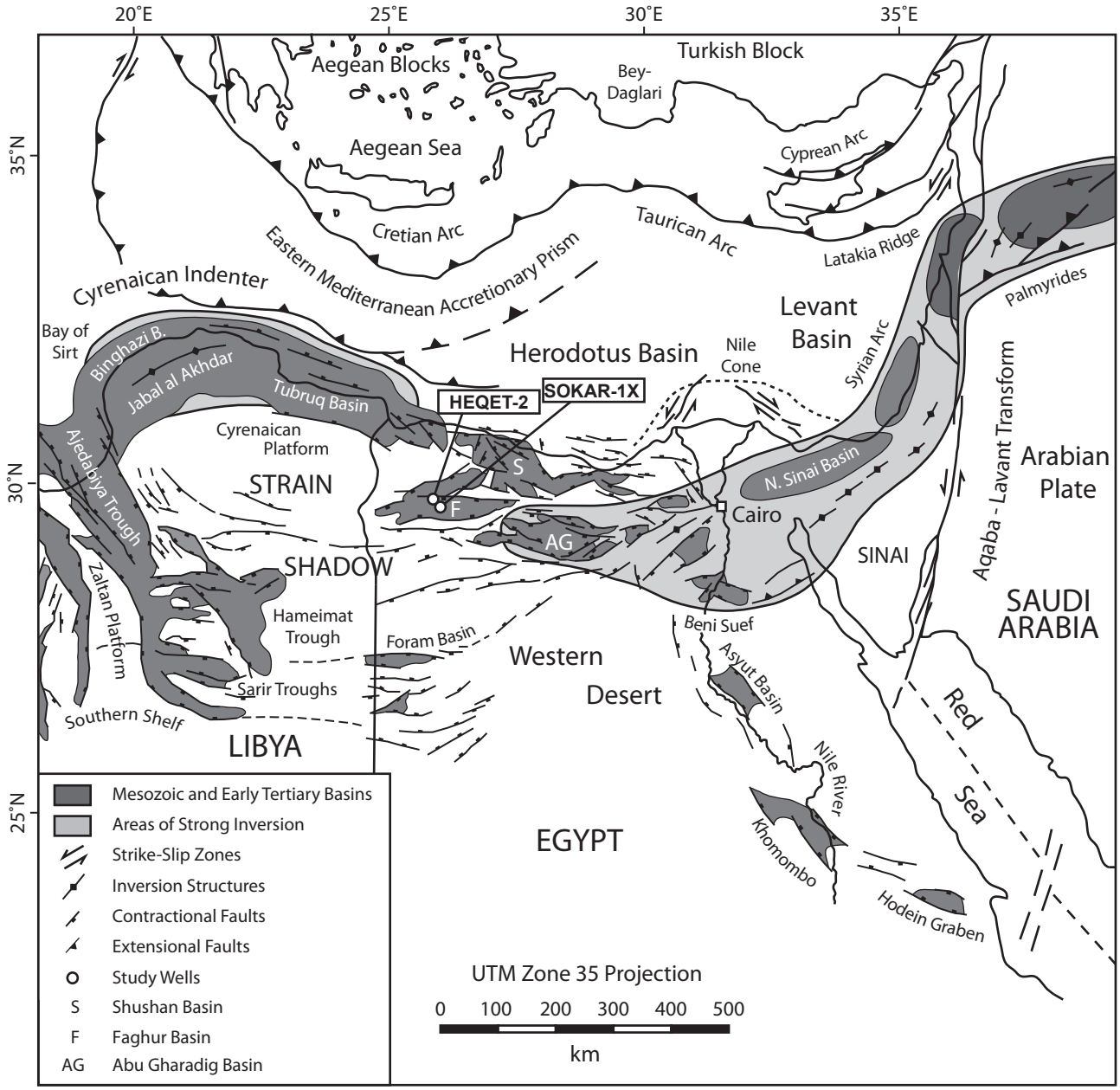
20°E
25°E
30°E
35°E
35°N
30°N
25°N
Aegean Blocks
Turkish Block
Bey-
Daglari
Aegean Sea
Cyprean Arc
Cretian Arc
Taurican Arc
Latakia Ridge
Eastern Mediterranean Accretionary Prism
Cyrenaican Indenter
Levant
Basin
Palmyrides
Bay of
Sirt
Binghazi B.
Jabal al Akhdar
Tubruq Basin
Herodotus Basin
Nile
Cone
Syrian Arc
HEQET-2
SOKAR-1X
Cyrenaican
Platform
STRAIN
S
F
AG
N. Sinai Basin
Cairo
Arabian
Plate
Aqaba - Lavant Transform
Ajedabiya Trough
SHADOW
SINAI
SAUDI
ARABIA
Zaltan Platform
Hameimat
Trough
Foram Basin
Beni Suef
Western
Desert
Asyut Basin
Sarir Troughs
Southern Shelf
LIBYA
Red
Sea
Nile River
EGYPT
Khomombo
Hodein Graben
Mesozoic and Early Tertiary Basins
Areas of Strong Inversion
Strike-Slip Zones
Inversion Structures
Contractional Faults
Extensional Faults
Study Wells
S Shushan Basin
F Faghur Basin
AG Abu Gharadig Basin
UTM Zone 35 Projection
0 100 200 300 400 500
km

Figure 2. Late Cretaceous cross-section of passive continental margin of northern Egypt (after Stampfli, 2001b). Location map after Bosworth and others (2008). Location of cross-section is approximate.

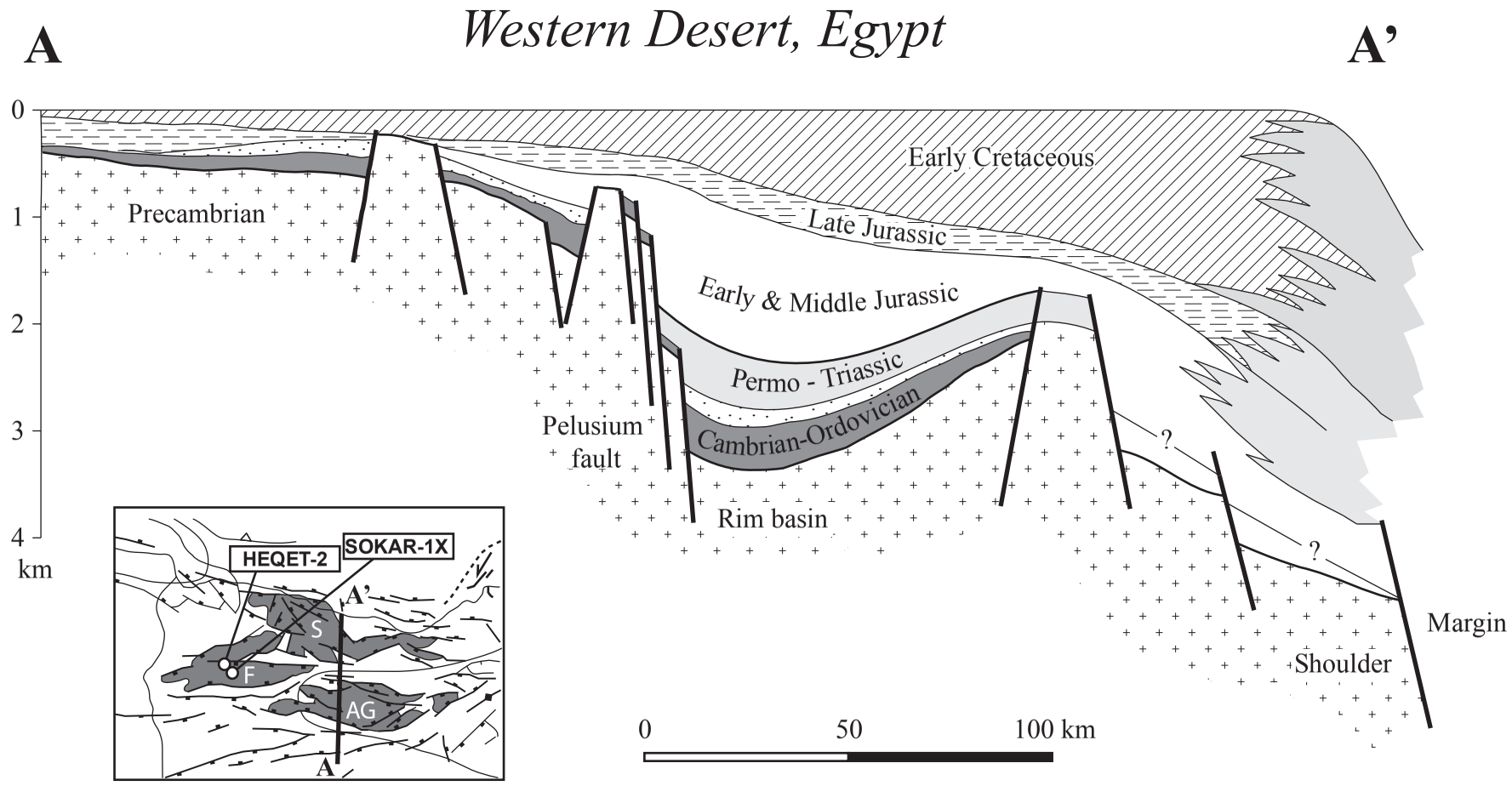
A
Western Desert, Egypt
A'
0
1
2
3
4
km
Precambrian
Early Cretaceous
Late Jurassic
Early & Middle Jurassic
Permo - Triassic
Cambrian-Ordovician
Pelusium
fault
Rim basin
?
?
Margin
Shoulder
0
50
100 km
HEQET-2
SOKAR-1X
A'
S
F
AG
A

Figure 3. Regional stratigraphy of the northern Western Desert (after El-Menshawy, 2004). Simplified stratigraphic column of the Sokar-1X and Hequet-2 boreholes showing formation tops. Sample intervals are highlighted in black.

Regional Stratigraphy Western Desert, Egypt

ERA	System	Unit		Formation	Member
CENOZOIC	Neogene	Miocene	M	Marmarica	
			E	Moghra	
	Paleogene	Oligocene		Dabaa	
		Eocene	L		
			M	Apollonian	
			E		
		Paleocene			
MESOZOIC	Cretaceous	Camp./Maest		Khoman	
		Santonian			
		Coniacian		Abu Roash	
		Turonian			
		Cenomanian	L		
			E	Bahariya	
		Albian	L	Kharita	
			M		
			E		
		Aptian		Dahab Shale	
				Alamein Dolomite	
		Barremian	L	Alam El Bueib (AEB)	Unit - 1
			M		Unit - 2
			E		Unit - 3
		Hauterivian			Unit - 4
		Valangenian			Unit - 5
		Berriasian			Unit - 6
	Jurassic	Kimn./Oxfo			
		Oxfordian		Masajid	
		Callovian/ L. Bathonian		Khatatba	Zahra
		E./M. Bathonian			Safa Upper
		Bajocian			Safa Lower
	Triassic			Ras Qattara	
PALEOZOIC	Carboniferous		L	Faghur Grp.	Safi
			M		Dhiffah
			E		Desouqy
	Devonian				Zeitun
	Silurian			Siwa Grp.	Basur
					Kohla
	Ordovician				Shifah
	Cambrian				
PRECAMBRIAN BASEMENT					

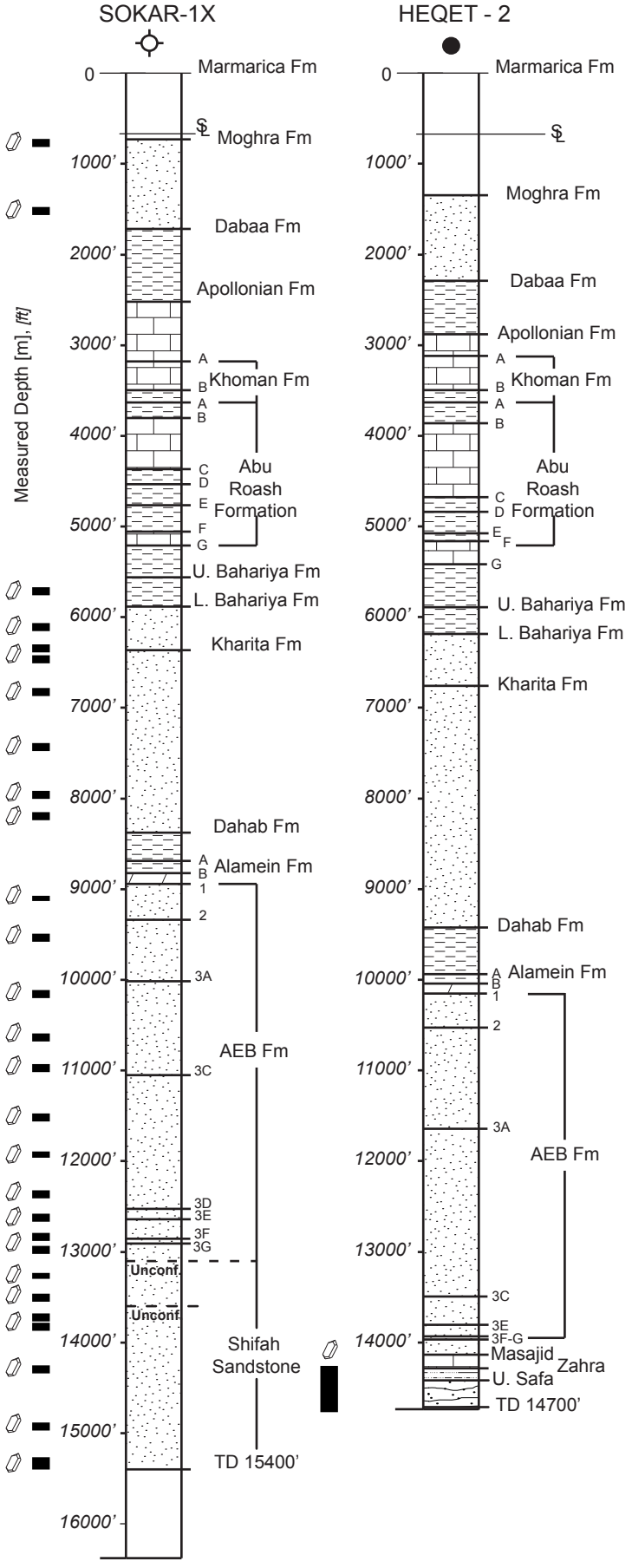

Figure 4. Degrees of abrasion in detrital zircon, shown under transmitted light.

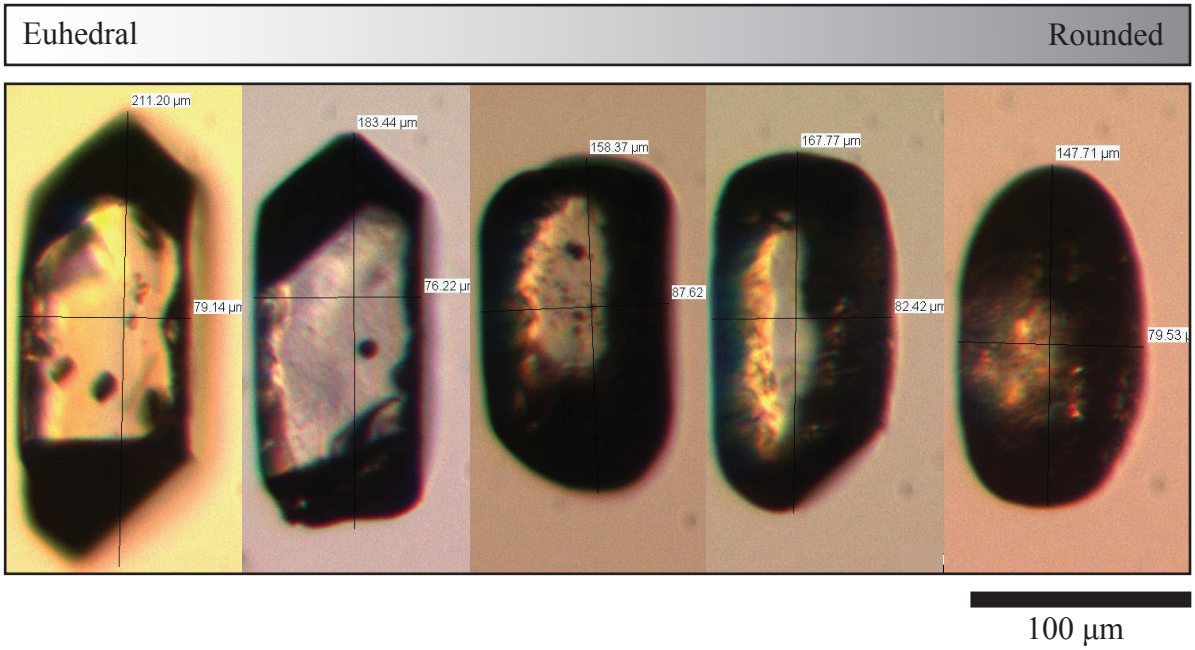
Euhedral
Rounded
211.20 µm
79.14 µm
183.44 µm
76.22 µm
158.37 µm
87.62
167.77 µm
82.42 µm
147.71 µm
79.53 µ
100 µm

Figure 5. ZHe ages for all aliquots from Sokar-1X and Heqet-2 boreholes. Minimum and maximum stratigraphic ages of host rocks are shown. Heqet-2 ZHe ages are from the Upper Safa Member of the Jurassic Khatatba Formation. Aliquots removed by filter 2 are shown in light grey.

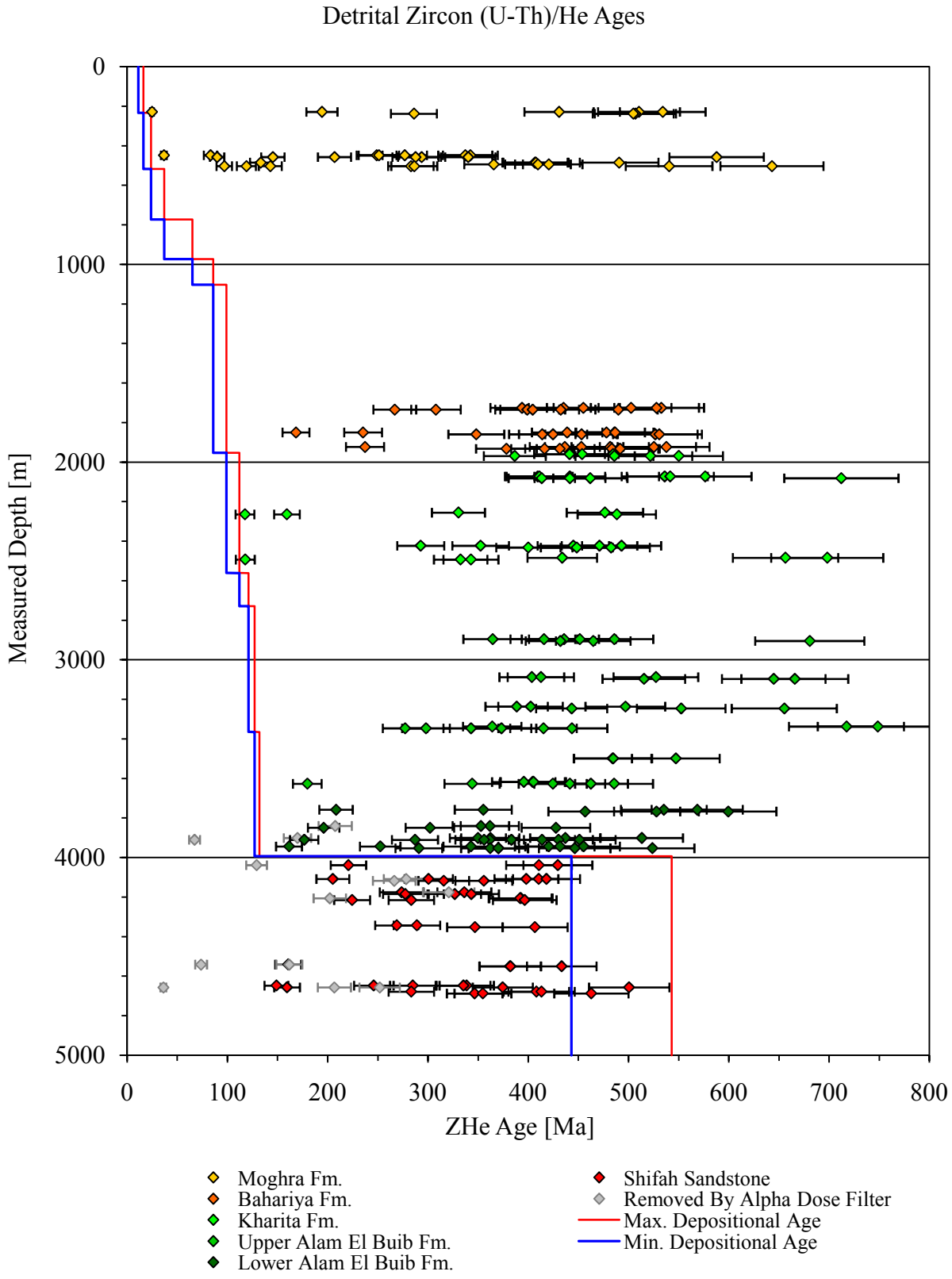
Detrital Zircon (U-Th)/He Ages
Measured Depth [m]
0
1000
2000
3000
4000
5000
0
100
200
300
400
500
600
700
800
ZHe Age [Ma]
Moghra Fm.
Bahariya Fm.
Kharita Fm.
Upper Alam El Buib Fm.
Lower Alam El Buib Fm.
Shifah Sandstone
Removed By Alpha Dose Filter
Max. Depositional Age
Min. Depositional Age

Figure 6. ZHe Age vs. alpha-dosage. Moderate to severe metamict grains contain alpha=dosage above 3.0 E16. *Safa Member Khatatba Fm. Zircons are from the Heqet-2 borehole and all other formations are from the Sokar-1X borehole.

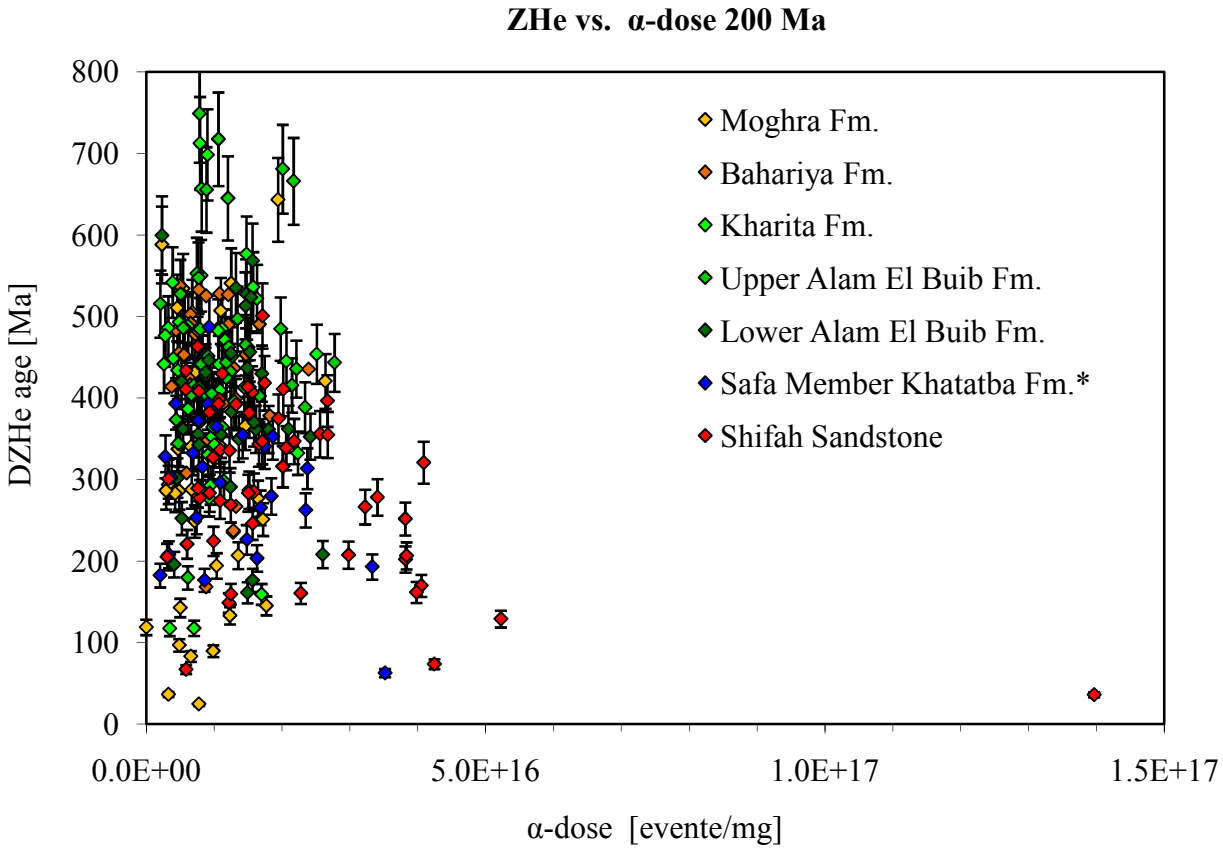
ZHe vs. α-dose 200 Ma
DZHe age [Ma]
800
700
600
500
400
300
200
100
0
0.0E+00
5.0E+16
1.0E+17
1.5E+17
α-dose [evente/mg]
Moghra Fm.
Bahariya Fm.
Kharita Fm.
Upper Alam El Buib Fm.
Lower Alam El Buib Fm.
Safa Member Khatatba Fm.*
Shifah Sandstone

Figure 7. Measured helium concentration [nmol/g] vs. alpha dosage [events/g] based on 200 Myr elapsed time for all Sokar-1X ZHe ages above 13,100 ft unconformity. This plot shows a distinct linear relationship for majority of analyses and two minority regions that exhibit excess He-loss and excess He, which are eliminated during analysis of probability density plots.

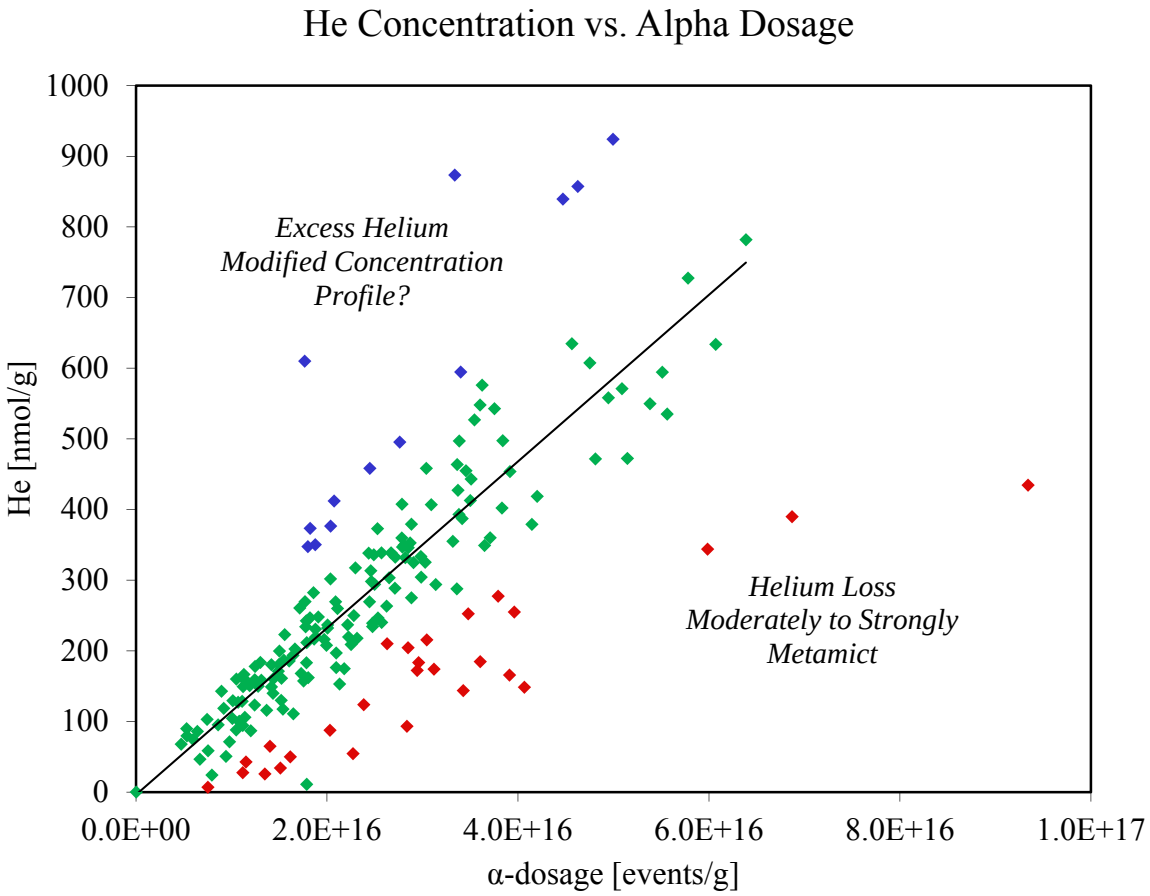
He Concentration vs. Alpha Dosage
He [nmol/g]
1000
900
800
700
600
500
400
300
200
100
0
0.0E+00
2.0E+16
4.0E+16
6.0E+16
8.0E+16
1.0E+17
α-dosage [events/g]
Excess Helium
Modified Concentration
Profile?
Helium Loss
Moderately to Strongly
Metamict

Figure 8. Probability density distribution of ZHe ages from the Shifa Formation below the Paleozoic-Mesozoic unconformity. All ages are younger than Cambro-Ordovician depositional ages. Aliquots were only taken from the 13,430 to 13,800 ft window to constrain the closest possible exhumation age to the unconformity. The average age of the 18 aliquots contributing to this curve is 329 +/- 26 Ma.

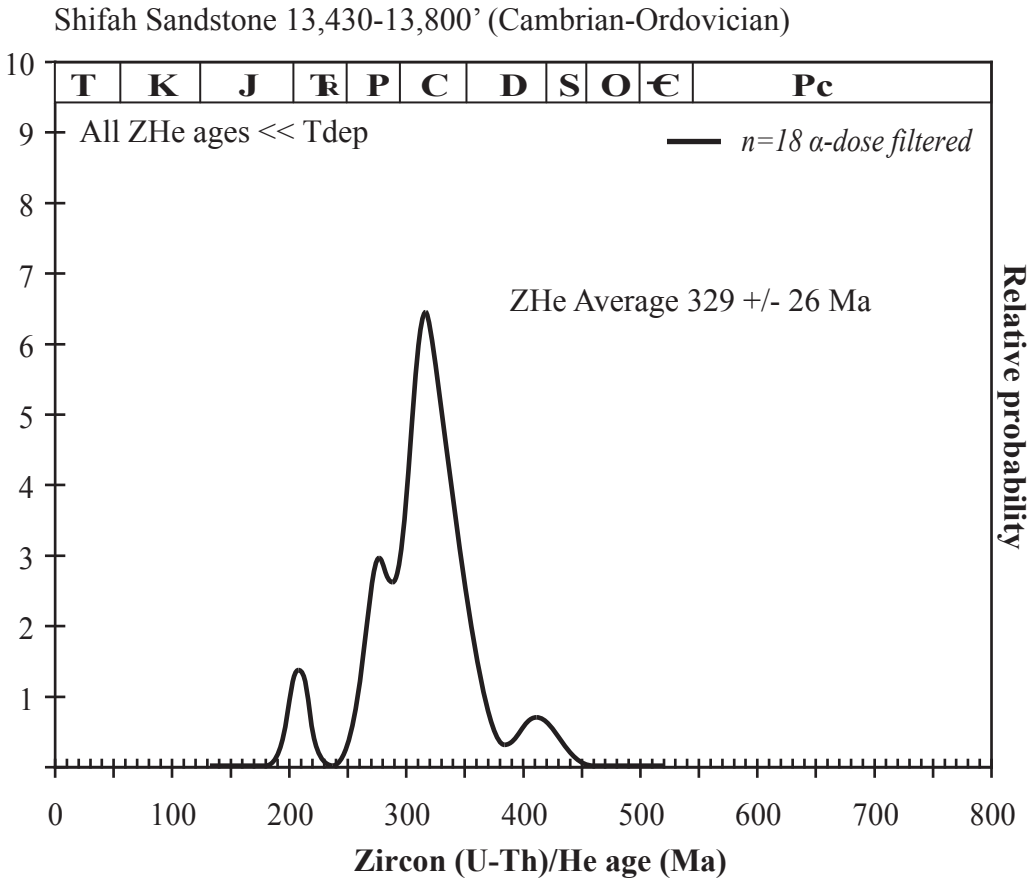
Shifah Sandstone 13,430-13,800' (Cambrian-Ordovician)
T
K
J
Tr
P
C
D
S
O
Pc
All ZHe ages << Tdep
n=18 α-dose filtered
ZHe Average 329 +/- 26 Ma
Relative probability
Zircon (U-Th)/He age (Ma)
0
100
200
300
400
500
600
700
800
1
2
3
4
5
6
7
8
9
10

Figure 9. Probability density distribution of ZHe ages from: (a) Upper Safa Member of the Jurassic Khatatba Formation; (b) lower members of the Early Cretaceous Alam El Buib Formation; (c) upper members of the Early Cretaceous Alam El Buib Formation; (d) Early Cretaceous Kharita Formation; (e) Late Cretaceous Bahariya Formation; and (f) Miocene Moghra Formation.

a) Khatatba Fm. Upper Safa Mbr. (Early-Middle Bathonian)
Hequet-2 14,460-14,700 ft

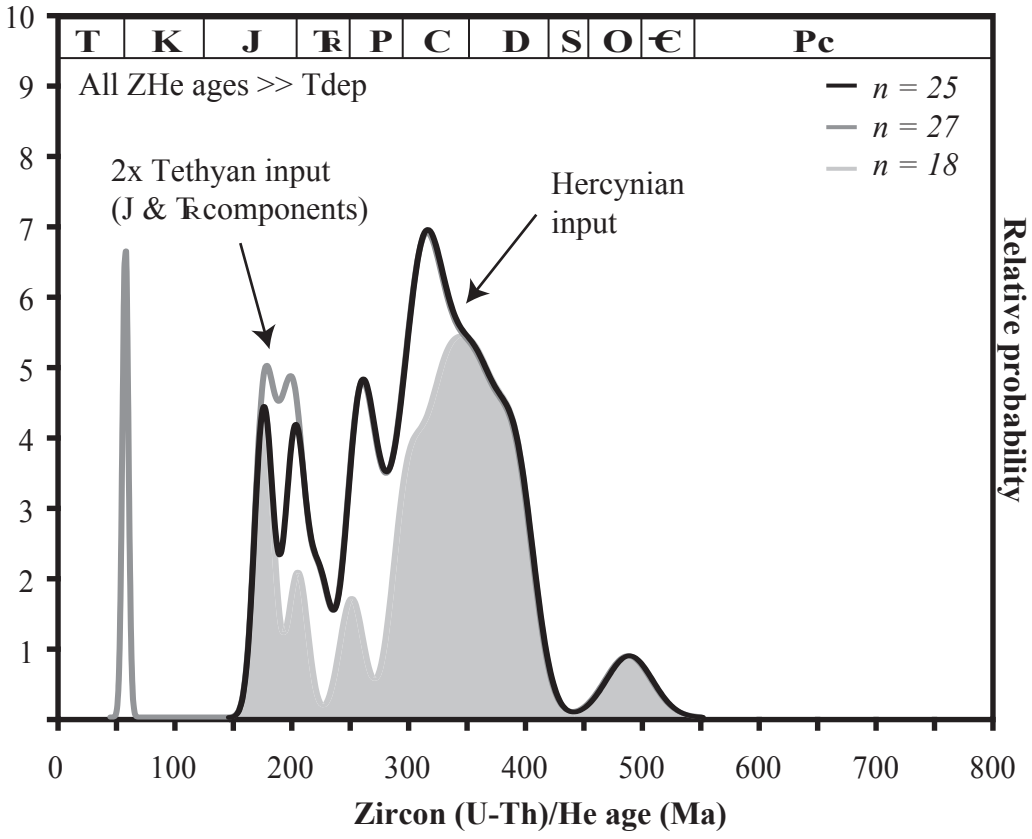

b) Alam El Buib Fm. 3C-3G (Hauterivian-Early Barremian)
Sokar-1X 12,000-13,100 ft

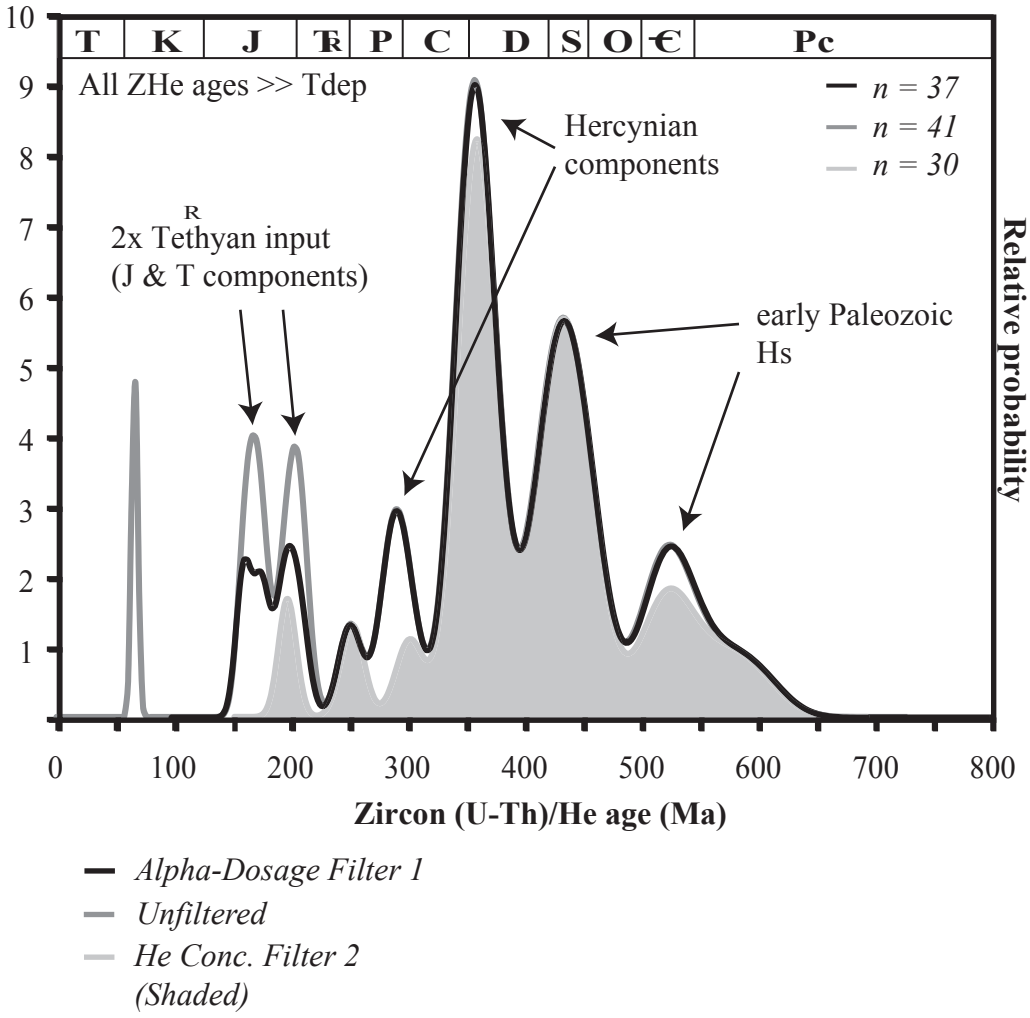

c) Alam El Buib Fm. 1-3C (Hauterivian-Early Barremian)
Sokar-1X 9,080-11,900 ft

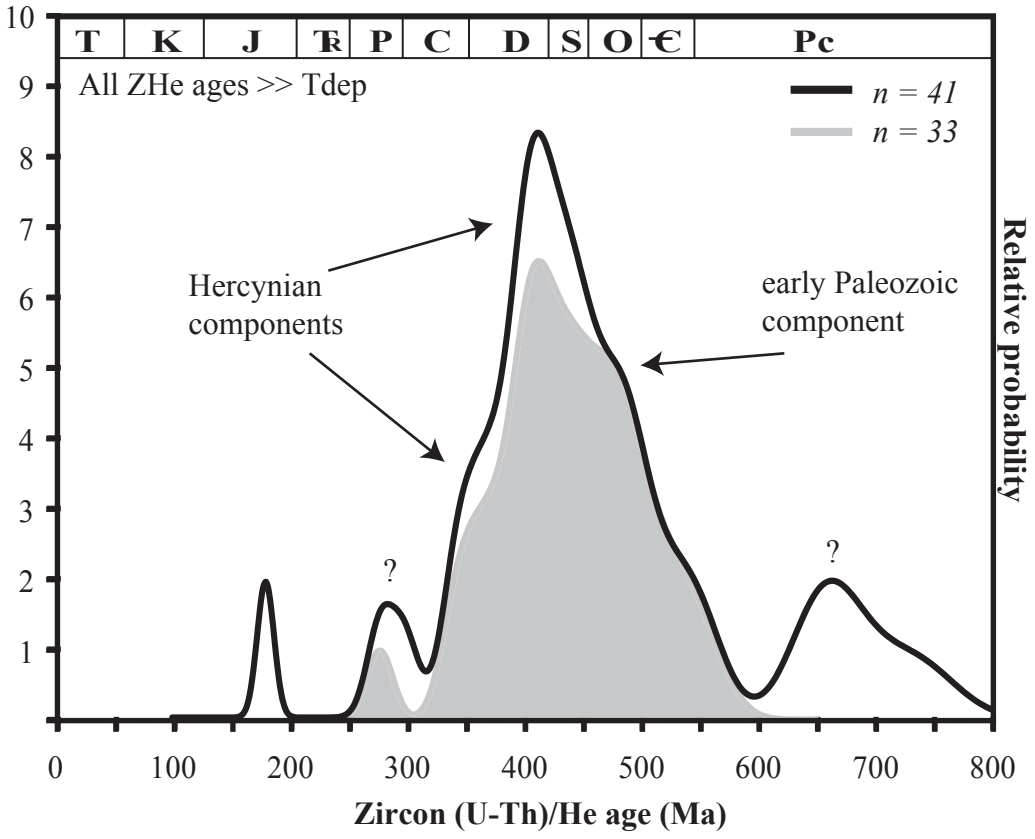

d) Kharita Fm. (Albian)
Sokar-1X 6,430-8,180 ft

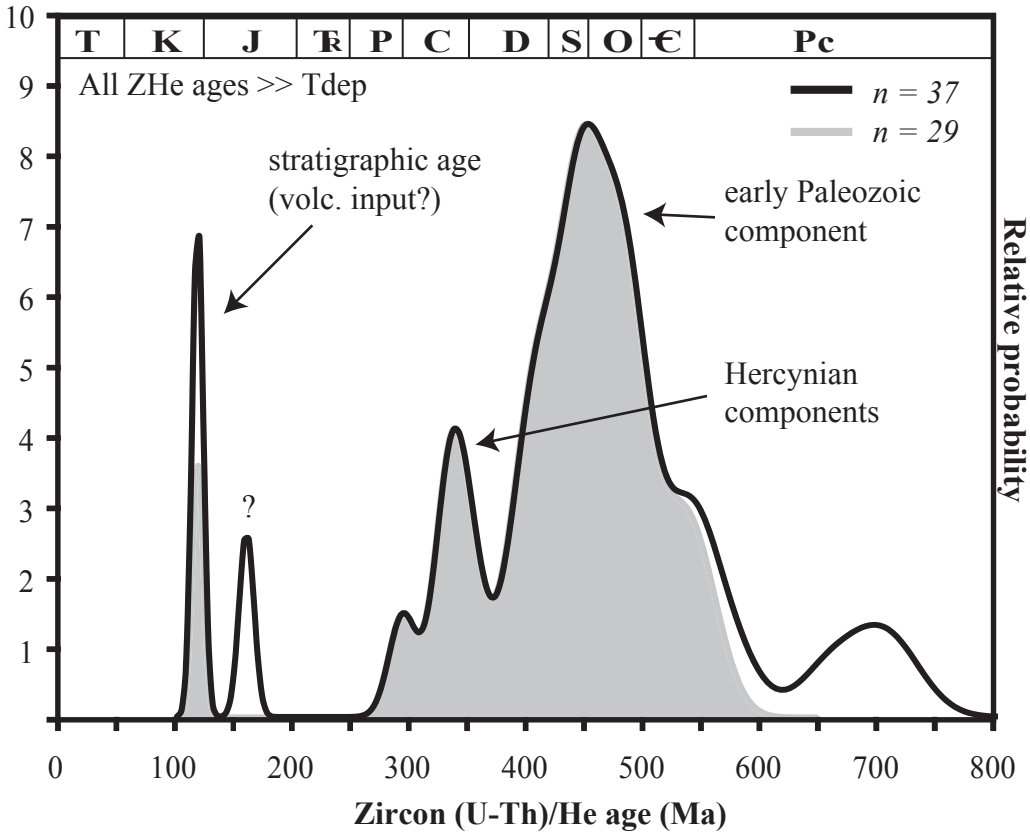

e) Bahariya Fm. (Cenomanian)
Sokar-1X 5,660-6,340 ft

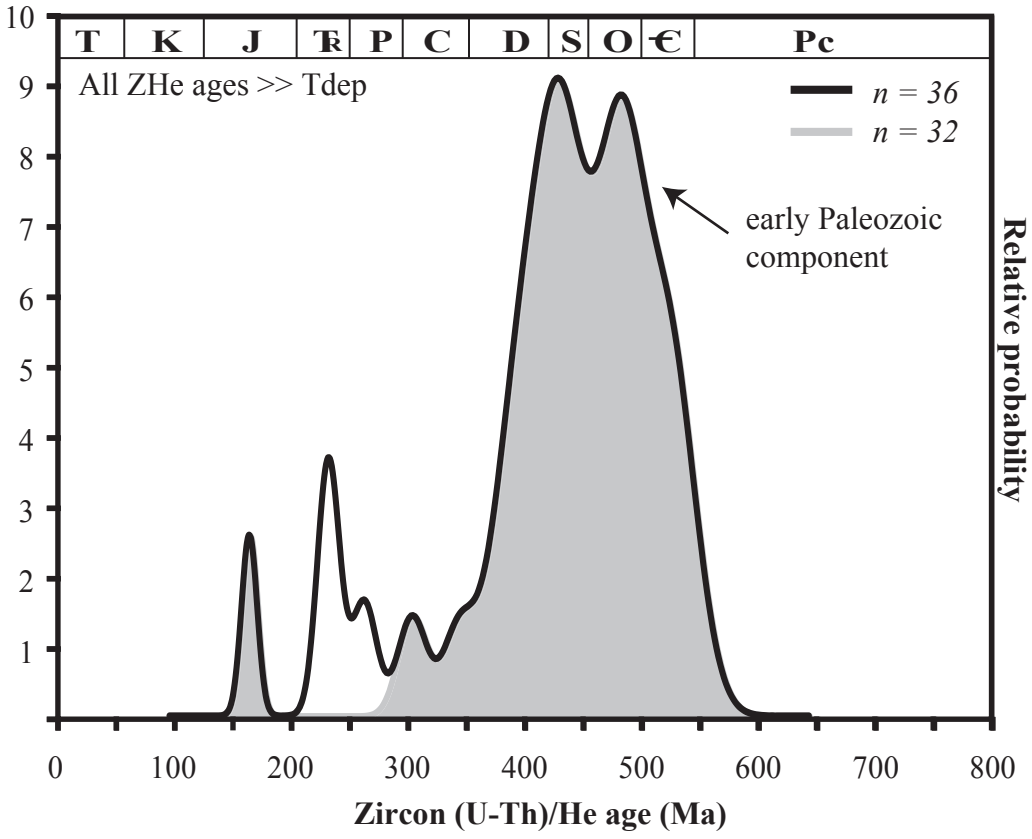

Alpha-Dosage Filter 1

He Conc. Filter 2 (Shaded)

f) Moghra Fm. (Miocene)
Sokar-1X 750-1,650 ft

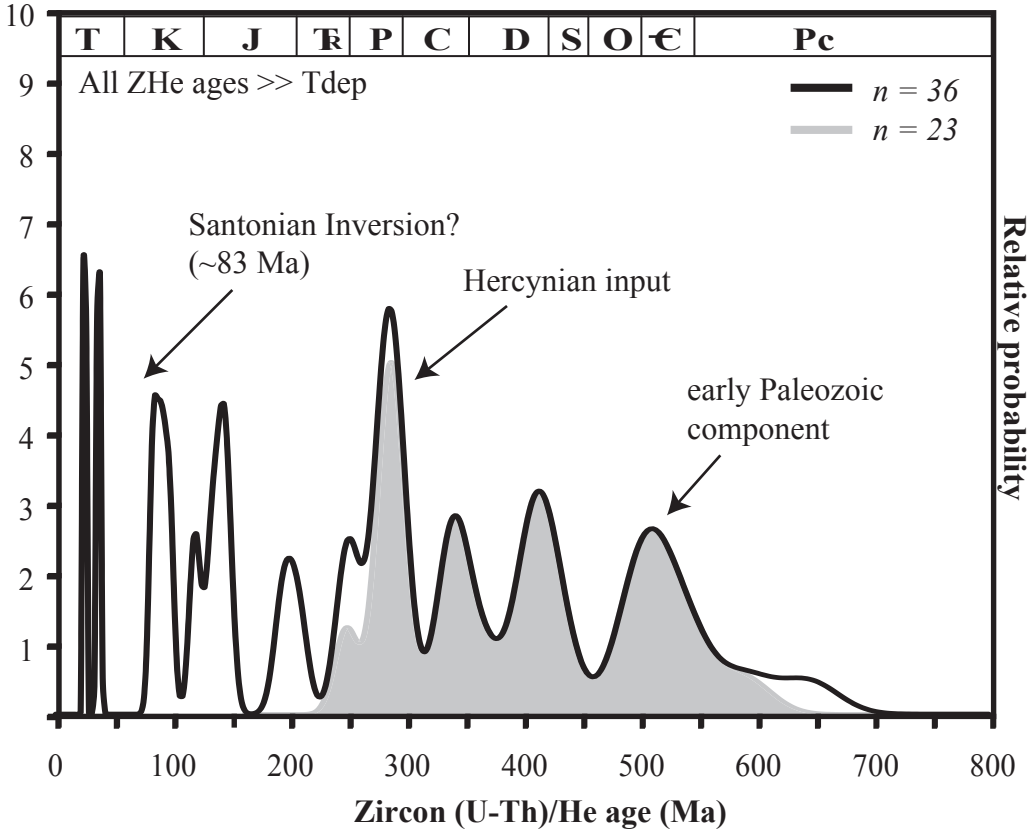

Figure 10. Compiled deconvolution of peak ages of the non-reset ZHe ages from Mesozoic and Cenozoic strata.

Figure 10 - ZHe Age Components

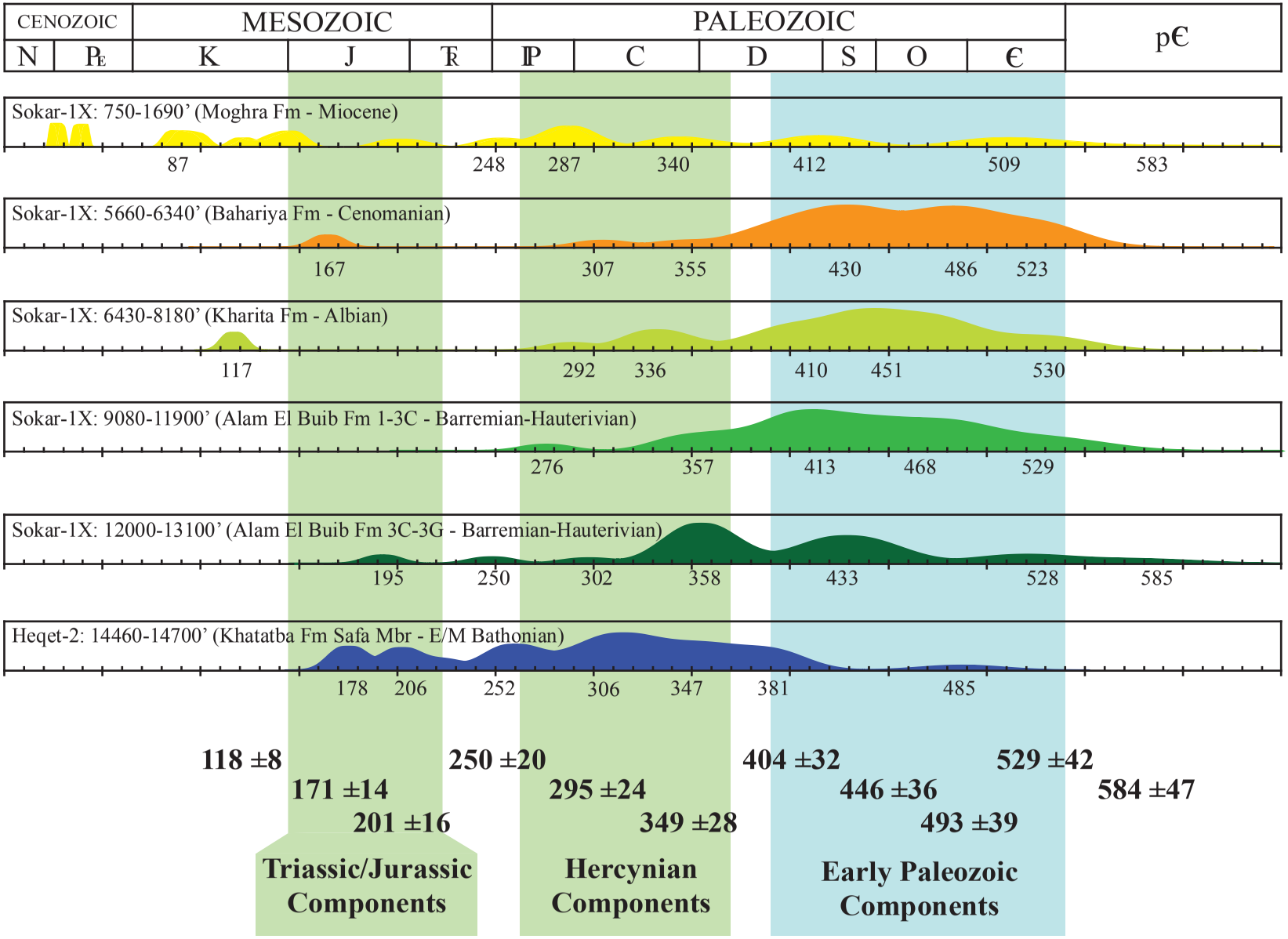

*All ages are picked from the original cumulative density distributions. 8% standard error is assumed for all ZHe ages.

Figure 11. Conceptual cross-section of the Sokar-1X vicinity during deposition of: (a) Jurassic Upper Safa Member of the Khatatba Formation, (b) the lower and (c) upper members of the Alam El Buib Formation and (d) the Kharita Formation during the Early Cretaceous, the (e) Bahariya Formation during the Late Cretaceous, and (f) the Moghra Formation during the Miocene following Late Cretaceous inversion.

Figure 11a - Detrital components of Upper Safa Member of the Khatatba Formation.

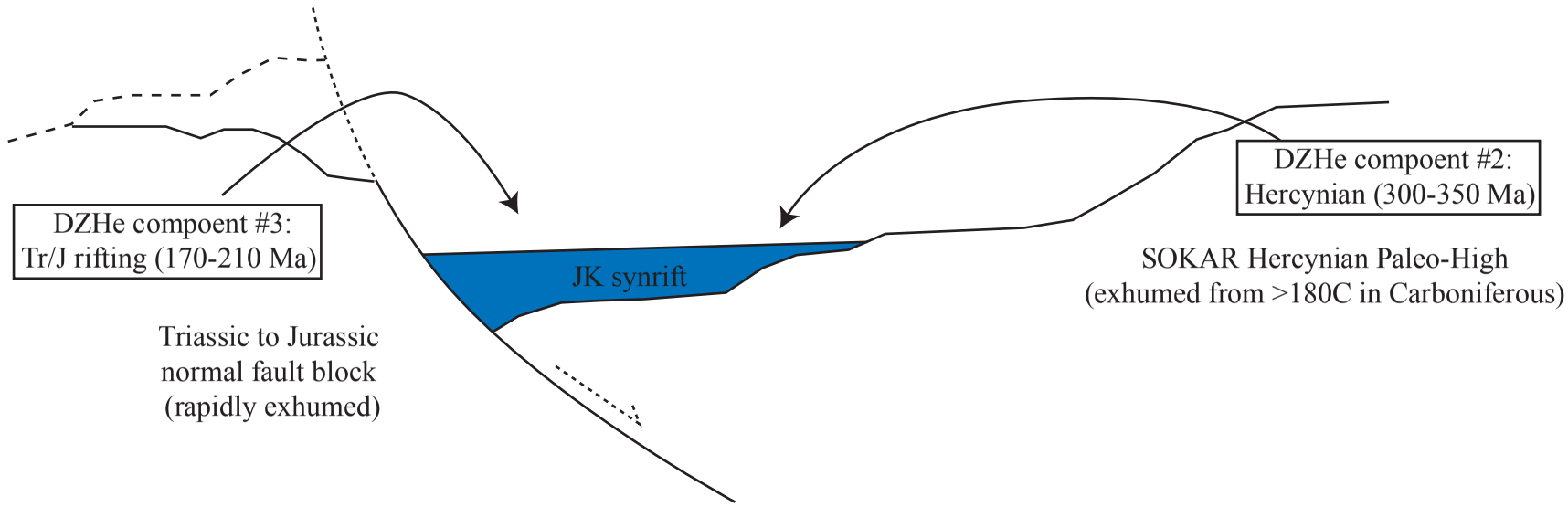

Figure 11b - Detrital components of lower members of the Alam El Buib Formation..

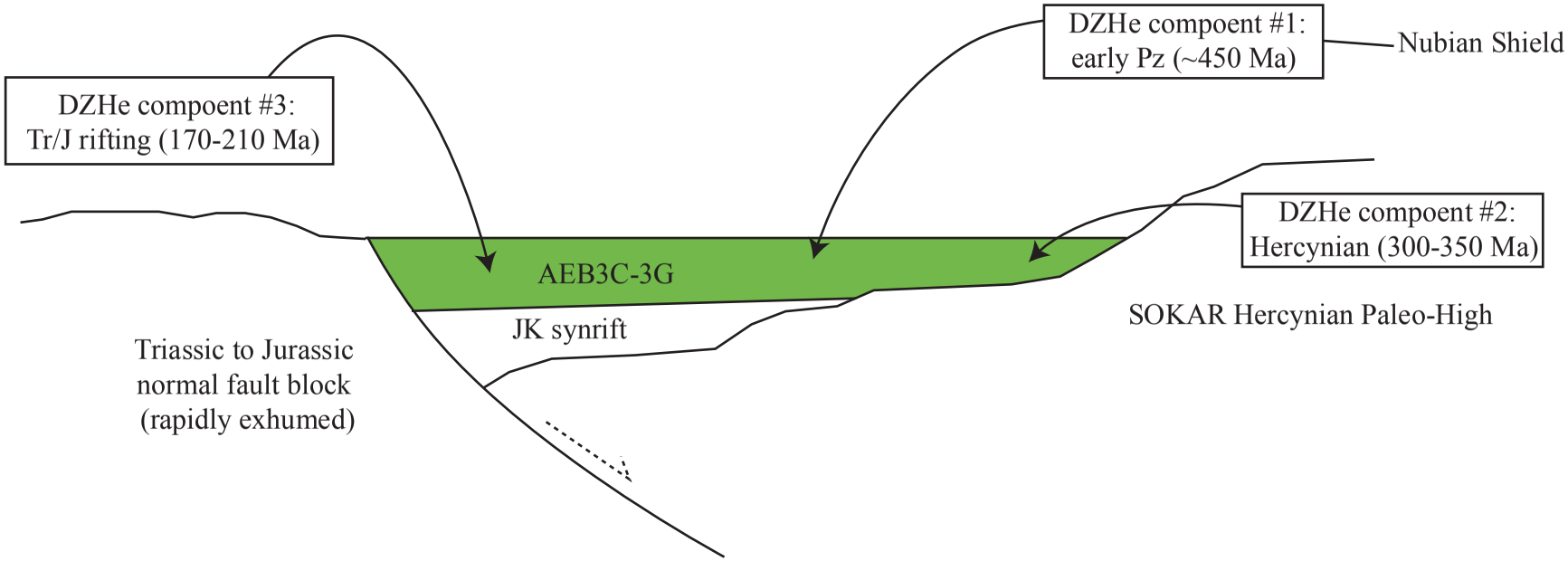

Figure 11c - Detrital components of upper members of the Alam El Buib Formation.

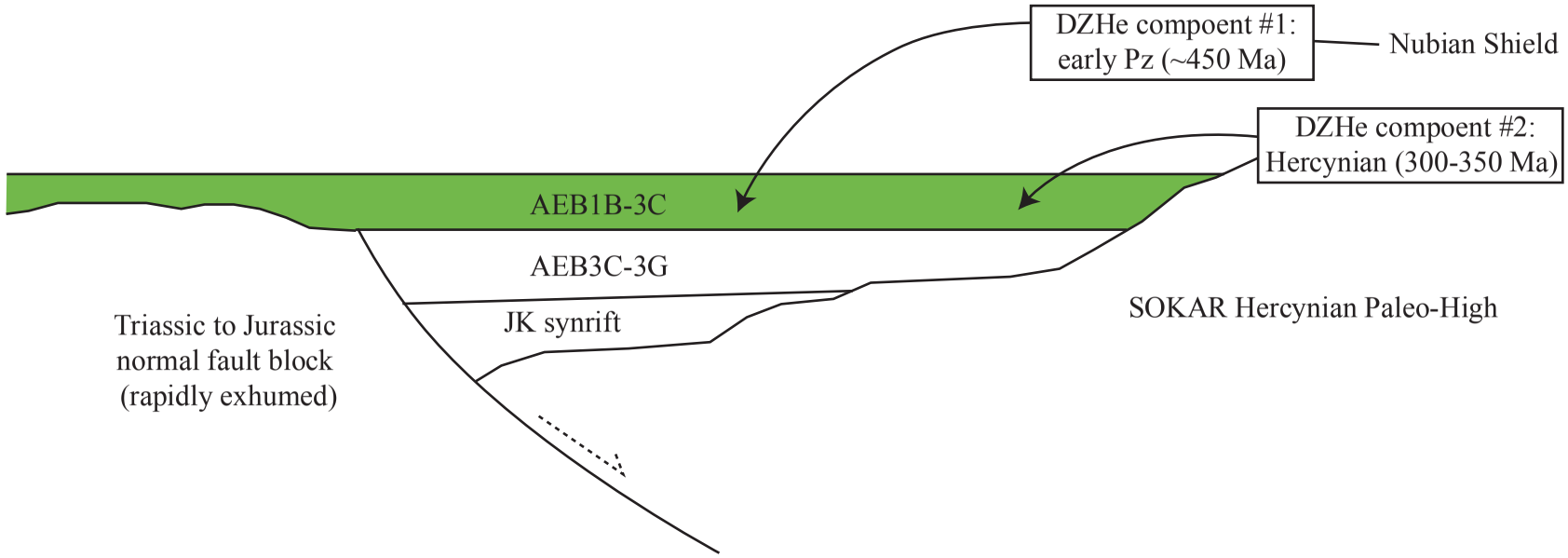

Figure 11d - Detrital components of Kharita Formation.

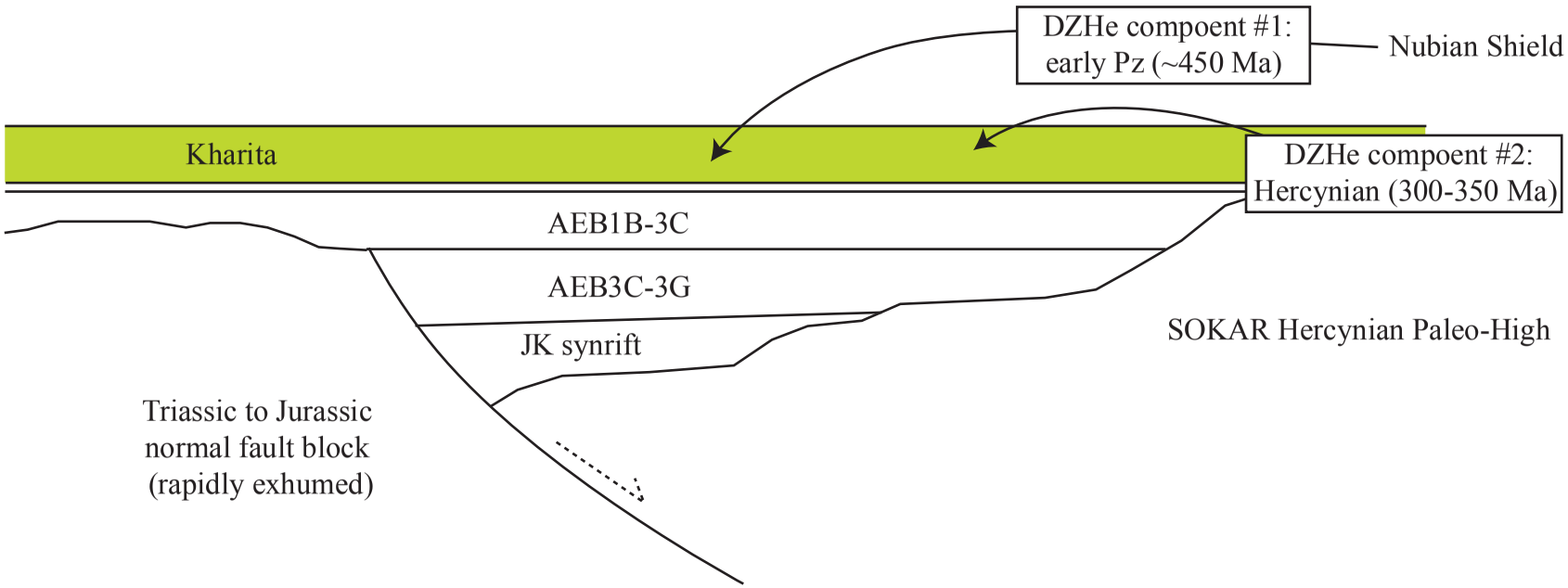

Figure 11e - Detrital components of Bahariya Formation.

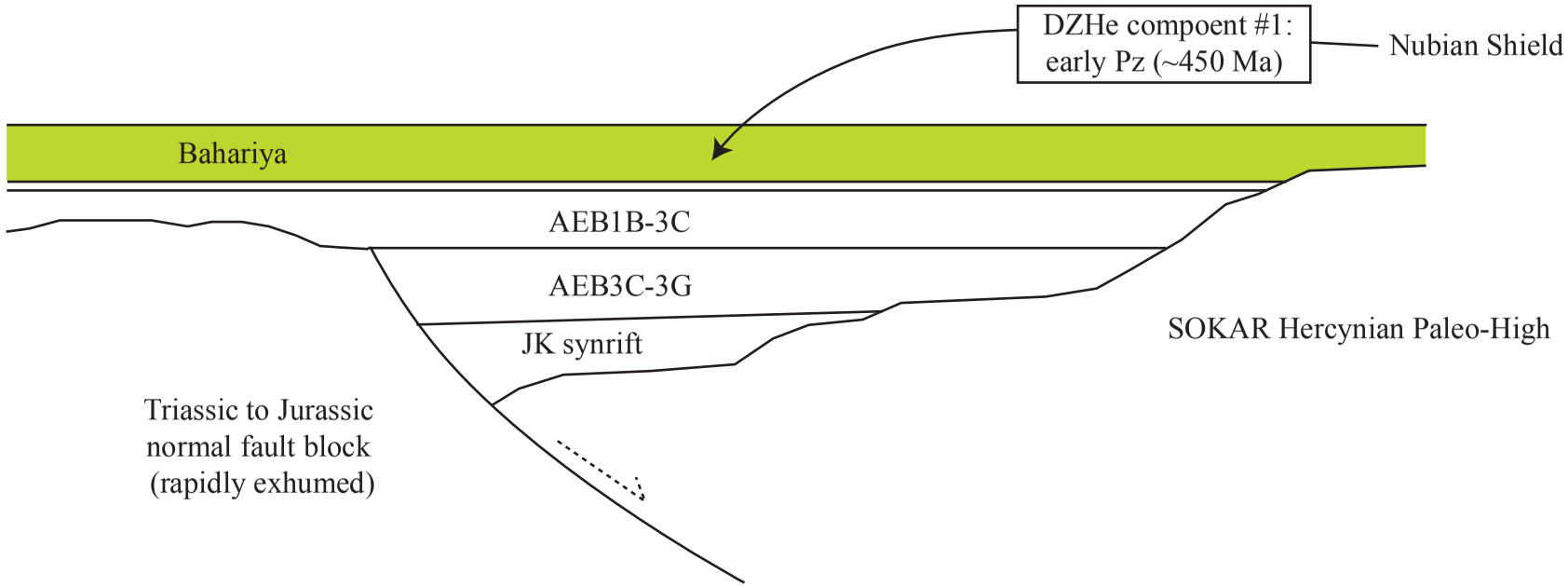

Figure 11f - Detrital components of Moghra Formation.

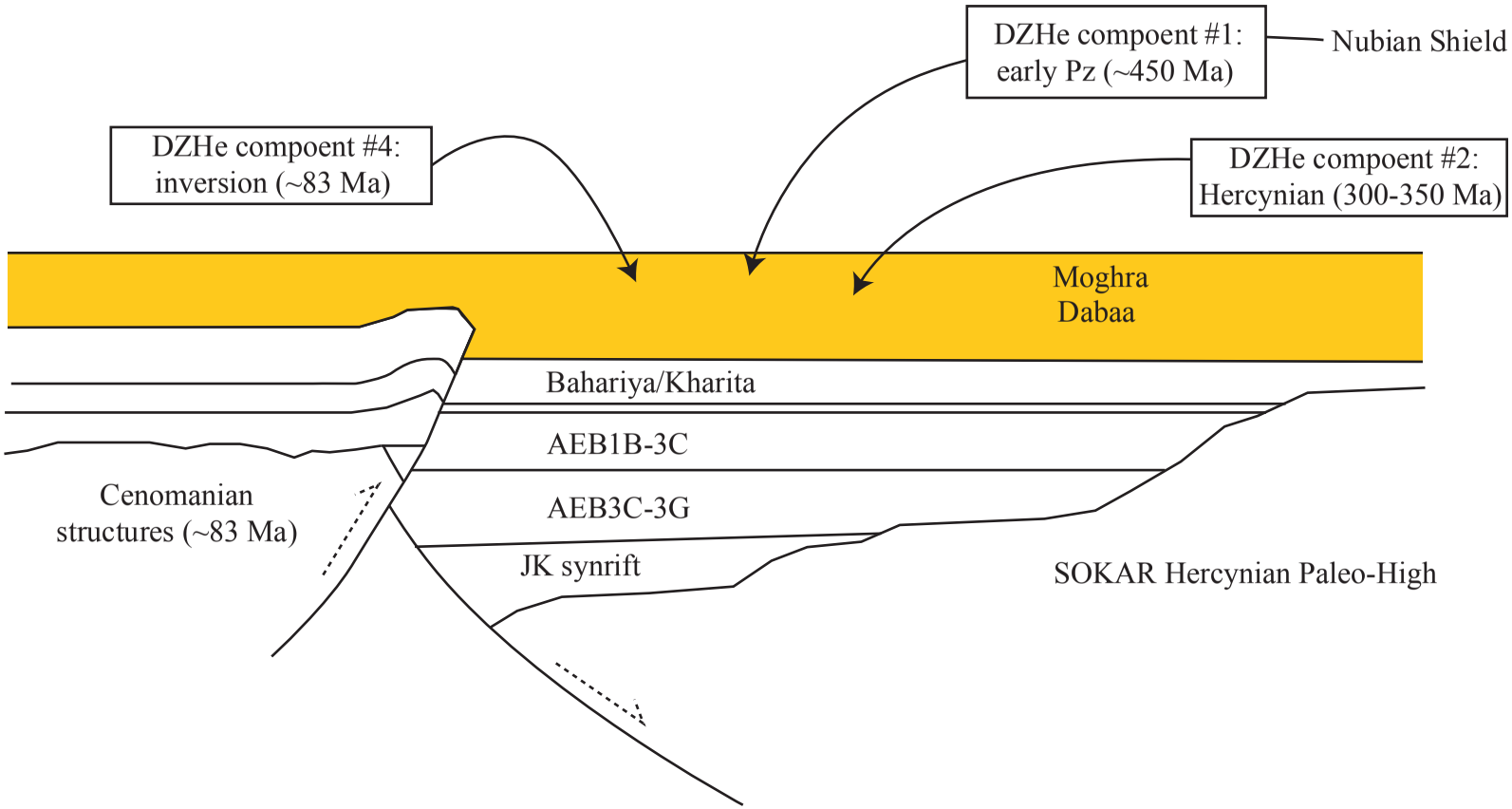

CHAPTER 2: Detrital Apatite (U-Th)/He Thermochronometry of Cuttings from the Sokar-1X Borehole, Western Desert, Egypt

Abstract

Detrital apatite (U-Th)/He (DAHe) age populations from cuttings of a borehole that penetrates the Moghra Formation in the northern Western Desert of Egypt correspond to several Late Cretaceous to Late Eocene compressional events that shaped the Neotethyan margin. Strong evidence of the well-studied and widespread Santonian inversion of most basins in northern Africa at ~83 Ma is recorded within analytical error at 85.1 +/- 6.8 Ma. Late Maastrichtian inversion is recorded at 67.5 +/- 5.4 Ma as well as Late Eocene to Early Oligocene inversion at 38.9 +/- 3.1 Ma. Syndepositional volcanic ages are recorded at 20.4 +/- 1.6 Ma, and represent the onset of Early Miocene rifting.

1. Introduction

The primary investigation of the basal Cretaceous unconformity encountered in the Sokar-1X well does not include support from detrital apatite (U-Th)/He data because the temperature at the unconformity exceeds the AHe closure temperature, which has been accepted to be . However, samples from the upper regions of the borehole are cool enough to provide other useful AHe information and are explained separately in this section. Similar to the zircon study, apatites from the Moghra Formation display a significant spread in AHe ages, which is representative of detrital-source cooling with respect to the apatite (U-Th)/He closure temperature. Several detrital-source cooling populations correspond very well with Late Cretaceous to Miocene collision and rifting events, particularly multiple phases of short-lived but widespread basin inversion in northern Africa. This study is the apatite analog of the higher resolution zircon study from the same suite of samples.

2. Geologic Setting

Late Paleozoic to Neogene stratigraphy of the African plate mainly reflects continental rifting and development of passive continental margins, but several short-lived and widespread compressional events affected much of the continent from the Permian to Recent (Guiraud and Bosworth, 1997). One of the most studied of these events is collision-related basin inversion during the Santonian. A change in rotation of the African plate during the opening of the Atlantic Ocean created dextral transpression across the North African Lineament (Guiraud and Bosworth, 1999), inverting many basins from Morocco to Oman (Bosworth, 2008). Similar compressional events also occurred between the Late Cretaceous and Neogene.

The surface geology of the Western Desert comprises a thin veneer of Miocene fluvio-marine clastics that conceals a thick wedge of Paleozoic to Cenozoic rocks. The Early Miocene Mogrha Formation consists of fluvio-marine clastics deposited in a river system that drained water from northern Africa (Said, 1962).

3. Methodology

3.1 Detrital Apatite (U-Th)/He Thermochronology

Apatite is a well established (U-Th)/He thermochronometer applied to many recent geologic, stratigraphic, tectonic, and geomorphologic studies (Ehlers and Farley, 2003; Reiners et al., 2005; Stockli, 2005). (U-Th)/He dating is based on the decay of ^{235}U, ^{238}U, and ^{232}Th to produce ^{4}He nuclei (alpha emission). The retention of ^{4}He nuclei (He age) within the crystal lattice is dependent on thermally activated diffusive loss and is strongly affected by a mineral-specific partial retention zone (PRZ). At temperatures above the partial retention zone all ^{4}He is lost, resetting the age to zero, and below no ^{4}He is lost through thermal diffusion. The partial retention zone for apatite (AHe PRZ) is 80 to ~40°C (Wolf et al., 1996; Stockli, 2000).

In this study drilling measurements indicate the present AHe PRZ boundaries are between ~6,000 and 2,000 ft measured depth (Fig. 1). From ~5,500-2,000 ft, the dominant lithologies are carbonate and mudstone, which unfortunately, do not yield apatite or zircon, so these rocks were not sampled. DAHe ages below the PRZ are clearly reset. Between 5,500-6,000 ft, only a few samples yield DAHe ages, defining the lower depth limits of the modern partial retention zone (RPZ), and the full PRZ cannot be seen from the intervals sampled.

3.2 Sampling Complexities

Apatite yield from Sokar-1X cuttings was relatively low compared to zircon yield. Most samples of cuttings approximately 500 g dry weight only yields a few grains of apatite after standard mineral separation. As a result of low apatite yield, ideal apatite grains were extremely rare. There was significant variety in size and roundedness of apatite, which was likely due to differing detrital provenance. All apatite were analyzed as single grains in order to preserve detrital ages of differing populations. Some apatite contained minor inclusions and needed to be dissolved in pressure vessel dissolution in order to account for helium produced by non-phosphate U-Th-bearing inclusions.

4. Results

The theoretical boundary of the AHe PRZ defined by the present day geothermal gradient separates two regions of AHe ages (Fig. 2). Below the AHe PRZ, AHe ages are all within analytiacal error of zero with the exception of a few outliers around 10 Ma. Above the PRZ, AHe ages are equal to or older than the Early Miocene Moghra Formation. A cumulative probability density distribution (Fig. 3) for AHe ages within the Moghra Formation shows four major detrital sources from Late Cretaceous to the Neogene. AHe ages contributive to each population were combined resulting in the following average population ages: 85.1 +/- 6.8 Ma, 67.5 +/- 5.4 Ma, 38.9 +/- 3.1 Ma and 20.4 +/- 1.6 Ma.

5. Discussion and Conclusions

Apatite extracted for Early Miocene Moghra Formation contains several DAHe age populations ranging from ~20-80 Ma. This indicates that Miocene rocks were not buried to a depth to exceed the closure temperature of Apatite. DAHe ages around 80 Ma further supports

the record of basin inversion during the Santonian (Guiraud and Bosworth, 1997) seen in detrital zircons from the same unit (this work). Other basin inversion events are also recorded at the KT boundary as well as ~40 Ma. Basin inversions in Northern Africa at these times are less studied than the Santonian, but in a similar way correlate extremely well with global tectonic events. The Central Alps were building at 40 Ma from collision of Eurasia and the African plate, which correlates well with basin inversion seen in Africa and Arabia (Ziegler et al., 1995, Guiraud and Bosworth, 1997).

These basin inversion events are not represented well in the zircon study of the same suite of samples due to the amount burial required to reset zircon prior to exhumation. Apatite requires less burial to be reset, so Late Cretaceous to Oligocene basin inversion structures may have enough structural throw to exhume reset apatite. In case of zircon there is not enough structural offset during the Santonian to exhume reset zircon, yet there is a marked population in the Moghra Formation at ~83 Ma. This suggests that another source of heat is present to reset zircon, such as the presence of hot fluids in fault zones. The secondary heat source would be more than enough to reset apatite as well. Detrital AHe ages from a single formation record several compressional episodes from Late Cretaceous to the Oligoccene. Futhermore, synrift detrital apatite provides additional absolute age constraints on the deposition of the Moghra Formation in the northern Western Desert.

6. Future Work

Additional samples from the Moghra Formation may yield significant apatite to further constrain basin inversion events within the region. The apatite fractions from Sokar-1X cuttings contained a significant number of microfossils, particularly conodont fragments. Perhaps in the

future biogenic apatite as a (U-Th)/He thermochronometer may support crystalline detrital apatite, pending current research (Reiners et al., 2006; Peppe and Reiners, 2007). If the significant carbonate section of Sokar-1X could be re-sampled for biogenic apatite, the PRZ for apatite may be visible in resulting ages. These theoretical analyses would then have to be treated not as detrital ages, but rather as local depositional/exhumation ages since biogenic apatite in these carbonates would have belonged to the organisms living in that environment. Possibly several more *cans of worms* would come from that study.

REFERENCES CITED

Bosworth, W., El-Hawat, A.S., Helgeson, D.E., and Burke, K., 2008, Cyrenaica "shock absorber" and associated inversion strain shadow in the collision zone of northeast Africa: Geology, v. 36, p. 695-698.

Ehlers, T.A., and Farley, K.A., 2003, Apatite (U-Th)/He thermochronometry: Methods and applications to problems in tectonic and surface processes: Earth and Planetary Science Letter, v. 206, p. 1-14.

Guiraud, R. and Bosworth, W., 1997, Senonian basin inversion and rejuvenation of rifting in Africa and Arabia: synthesis and implications to plate-scale tectonics: Tectonophysics, v. 282, p. 39-82.

-, 1999, Phanerozoic geodynamic evolution of northeastern Africa and the northwestern Arabian platform: Techtonophysics, v. 315, p. 73-108.

Peppe, D.J. and Reiners, P.W., 2007, Conodont (U/Th)/He thermochronometry: Initial results, potential, and problems: Earth an Planetary Science Letters, v. 258, p.569-580.

Reiners, P.W., Campbell, I.H., Nicolescu, S., Allen, C.M., Hourigan, J.K., Garver, J.I., Mattinson, J.M., and Cowan, D.S., 2005, (U-Th)/(He-Pb) double dating of detrital zircons: American Journal of Science, v. 305, p. 259-311.

Reiners, P.W., Peppe, D., Bibi, F. and Nicolescu, S., 2006, He diffusion in and (U-Th)/He dating of fossil tooth enamel and conodont: Goldschmidt Conference Abstracts, A525.

Said, R., 1962 Geology of Egypt, New York, p. 209-215.

Stockli, D.F., Farley, K.A., and Dumitru, T.A., 2000, Calibration ot the apatite (U-Th)/He thermochronometer on an exhumed fault block, White Mountains, California: Geology, v. 28, p. 983-986.

Stockli, D.F., 2005, Application of low-temperature thermochronometry to extensional tectonic settings.; Low-temperature thermochronology; techniques, interpretations, and applications: Reviews in Mineralogy and Geochemistry, v. 58, p. 411-448.

Wolf, R.A., Farley, K.A., and Silver, L.T., 1996, Helium diffusion and low-temperature thermochronometry of apatite, Geochimica et Cosmochimica Acta, v. 60, p. 4231-4240.

Ziegler, P.A., Cloetingh, S., and van Wees, J., 1995, Dynamics of intra-plate compressional deformation: The Alpine foreland and other examples: Tectonophysics, v. p. 252, 7-59.

LIST OF FIGURES AND TABLES

Table 1 – Sokar-1X Apatite (U-Th)/He Results (excerpt)

Sample	Aliqouts	MD [m]	Unit	Age [Ma]	± [Ma] 8%	U [ppm]	Th [ppm]	Sm [ppm]	Th/U	eU	He [nmol/g]	mass [µg]	Ft
SKR00750	AS0075-1	229	Moghra	40.7	2.4	10.3	25.4	22.2	2.5	16.3	2.45	2.5	0.67
	AS0075-2	229	Moghra	17.0	1.0	16.8	13.2	33.6	0.8	19.9	1.23	2.0	0.66
	AS0075-3	229	Moghra	67.0	4.0	21.1	59.8	71.8	2.8	35.1	7.25	1.1	0.56
	AS0075-4	229	Moghra	22.8	1.4	156.6	55.0	60.3	0.4	169.5	13.76	1.7	0.66
SKR00780	AS0078-2	238	Moghra	35.2	2.1	51.4	26.5	106.0	0.5	57.6	6.92	1.3	0.62
	AS0078-3	238	Moghra	86.3	5.2	11.5	9.7	68.3	0.8	13.8	4.26	1.5	0.64
	AS0078-4	238	Moghra	64.6	3.9	29.0	21.7	31.5	0.7	34.2	7.42	1.6	0.62
SKR01470	AS0147-1	448	Moghra	84.2	5.1	0.4	5.7	6.1	15.4	1.7	0.50	1.9	0.62
	AS0147-2	448	Moghra	40.9	2.5	11.6	31.5	59.1	2.7	19.0	2.69	1.6	0.62
	AS0147-3	448	Moghra	70.8	4.3	14.0	9.0	83.2	0.6	16.1	3.83	1.2	0.60
SKR01500	AS0150-2	457	Moghra	21.3	1.3	4.2	35.9	199.9	8.5	12.6	1.01	1.5	0.61
SKR06070	AS0607-1	1850	L. Bahariya	84.8	5.1	0.3	2.9	10.5	11.1	0.9	0.27	1.1	0.57
	AS0607-2	1850	L. Bahariya	67.5	4.0	24.9	42.5	29.7	1.7	34.9	7.46	1.0	0.58
SKR06080	AS0680-3	2073	Kharita	2.7	0.2	0.2	4.6	12.9	21.6	1.3	0.01	0.9	0.55
	AS0680-4	2073	Kharita	-0.8	-0.1	0.1	2.2	7.2	19.0	0.6	0.00	1.6	0.62
SKR07430	AS0743-1	2265	Kharita	12.6	0.8	8.2	6.4	56.3	0.8	9.7	0.46	2.1	0.67
	AS0743-2	2265	Kharita	2.8	0.2	42.6	36.7	130.4	0.9	51.2	0.50	1.4	0.63
	AS0743-3	2265	Kharita	1.3	0.1	14.3	23.6	183.8	1.7	19.8	0.09	0.9	0.57
SKR08150	AS0815-1	2484	Kharita	1.3	0.1	0.4	1.8	7.1	5.3	0.8	0.00	2.0	0.64
SKR09050	AS0905-1	2758	Alamein A	0.8	0.0	10.0	7.1	54.2	0.7	11.7	0.03	0.5	0.51
SKR13250	AS1325-2	4039	Shifa	7.6	5.1	0.1	2.5	9.6	21.4	0.7	0.02	1.3	0.60
SKR13280	AS1328-1	4048	Shifa	0.1	0.0	4.2	1.5	155.3	0.4	4.5	0.00	1.1	0.60
	AS1328-2	4048	Shifa	7.9	2.1	3.6	0.5	131.2	0.1	3.8	0.12	1.0	0.61
	AS1328-3	4048	Shifa	0.3	0.0	30.8	1.3	48.9	0.0	31.1	0.04	1.8	0.67
SKR13980	AS1398-1	4261	Shifa	0.2	0.0	3.5	13.1	120.1	3.7	6.6	0.00	5.0	0.66
	AS1398-2	4261	Shifa	0.3	0.0	3.4	15.3	102.5	4.5	7.0	0.01	5.9	0.67
	AS1398-3	4261	Shifa	0.1	0.0	2.7	11.9	91.3	4.4	5.5	0.00	5.7	0.67
SKR14010	AS1401-1	4270	Shifa	1.6	0.2	3.9	16.7	117.1	4.3	7.9	0.05	5.5	0.68
	AS1401-2	4270	Shifa	0.2	0.0	3.6	13.4	98.4	3.7	6.8	0.01	5.4	0.67
	AS1401-3	4270	Shifa	0.0	0.0	4.3	23.3	107.5	5.4	9.8	0.00	3.0	0.67
	AS1401-4	4270	Shifa	1.1	0.1	3.2	11.9	107.4	3.8	6.0	0.03	3.1	0.69
SKR14280	AS1428-1	4353	Shifa	2.2	0.3	3.9	15.1	121.5	3.8	7.5	0.06	3.5	0.63
	AS1428-2	4353	Shifa	1.4	0.2	3.6	13.3	107.3	3.7	6.7	0.04	4.8	0.67

Figure 1. Geothermal gradient in the Sokar-1X borehole and partial retention zone of relevant thermochronometers.

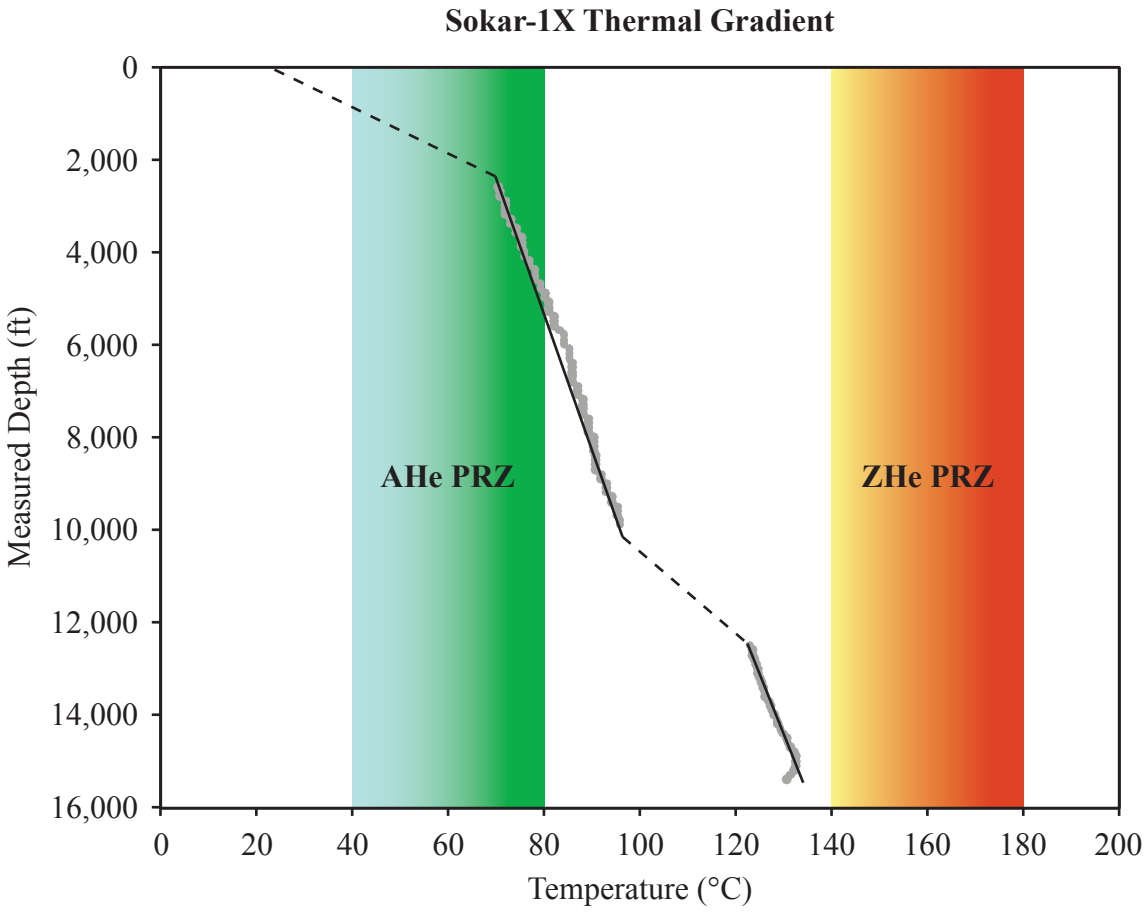
Sokar-1X Thermal Gradient
Measured Depth (ft)
0
2,000
4,000
6,000
8,000
10,000
12,000
14,000
16,000
AHe PRZ
ZHe PRZ
0
20
40
60
80
100
120
140
160
180
200
Temperature (°C)

Figure 2. Detrital Apatite (U-Th)/He ages from the Sokar-1X borehole. Apatite He partial retention zone separates “zero” age aliquots and non-reset AHe ages. Gap in data within the PRZ corresponds to lack of samples in carbonate and mudstone dominant lithologies.

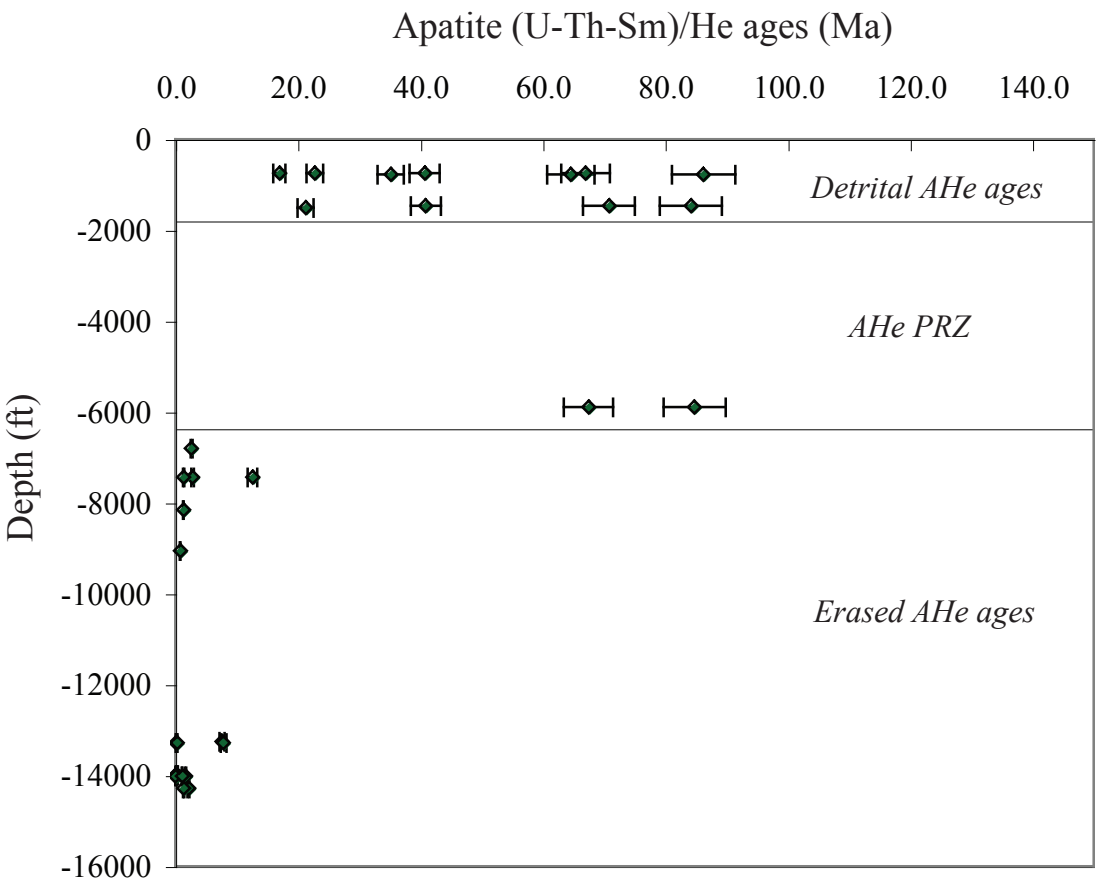
Apatite (U-Th-Sm)/He ages (Ma)
0.0
20.0
40.0
60.0
80.0
100.0
120.0
140.0
0
-2000
-4000
-6000
-8000
-10000
-12000
-14000
-16000
Depth (ft)
Detrital AHe ages
AHe PRZ
Erased AHe ages

Figure 3. Cumulative probability distribution of the single grain apatite (U-Th)/He ages and tectonic events of Africa and Arabia. Peak ages are based on the average of those ages contributing to peak groups, and peak error is based on 8% standard analytical error of the resulting averages. Tectonic events are labeled after Guiraud and Bosworth (1997). Timescale is after GSA (1999).

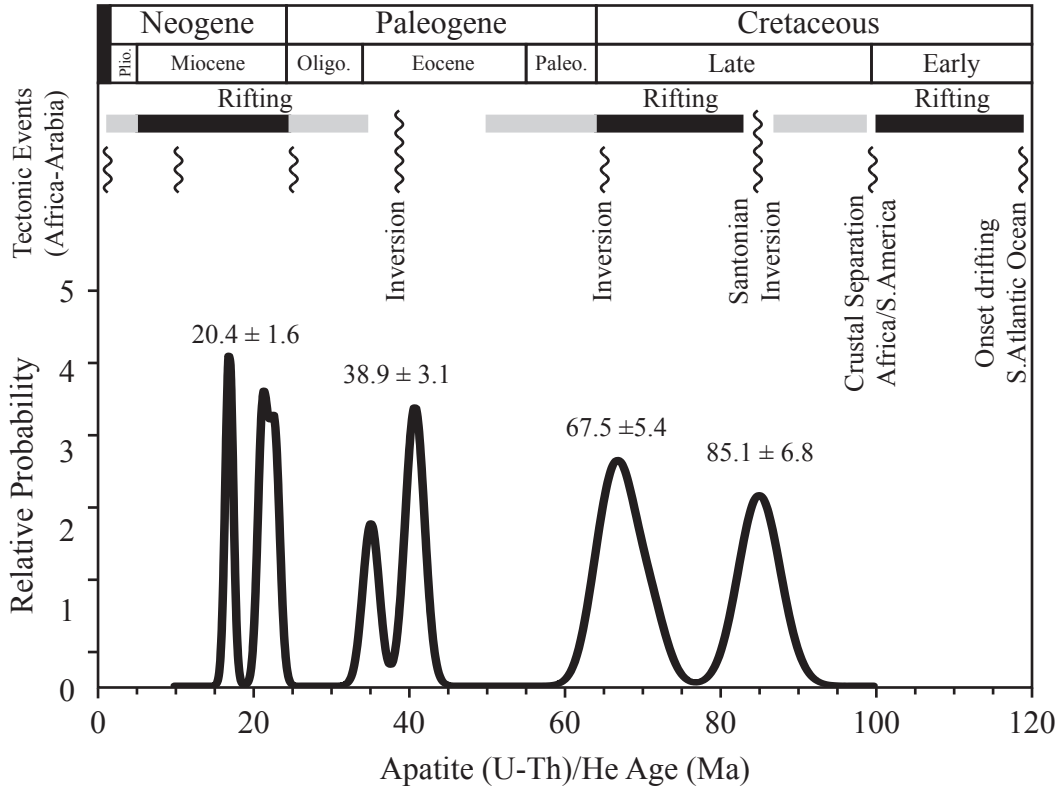
Neogene
Paleogene
Cretaceous
Plio.
Miocene
Oligo.
Eocene
Paleo.
Late
Early
Tectonic Events
(Africa-Arabia)
Rifting
Rifting
Rifting
Inversion
Inversion
Santonian
Inversion
Crustal Separation
Africa/S.America
Onset drifting
S.Atlantic Ocean
20.4 ± 1.6
38.9 ± 3.1
67.5 ±5.4
85.1 ± 6.8
Relative Probability
0
1
2
3
4
5
0
20
40
60
80
100
120
Apatite (U-Th)/He Age (Ma)